ANALYSIS OF FRACTURES IN 3D LINEAR PIEZOELECTRIC MEDIA

Mr. Weeraporn Phongtinnaboot

A Dissertation Submitted in Partial Fulfillment of the Requirements

for the Degree of Doctor of Philosophy Program in Civil Engineering

Department of Civil Engineering

Faculty of Engineering

Chulalongkorn University

Academic Year 2011

การวิเคราะห์รอยแตกร้าวในตัวกลาง 3 มิติที่ทำมาจากวัสดุไพอิโซอิเล็กทริกเชิงเส้น

นายวีรพร พงศ์ติณบุตร

Thesis Title   ANALYSIS OF FRACTURES IN 3D LINEAR PIEZOELECTRIC MEDIA

By   Mr. Weeraporn Phongtinnaboot

Field of Study   Civil Engineering

Thesis Advisor   Assistant Professor Chatpan Chintanapakdee, Ph.D.

Thesis Co-advisor   Assistant Professor Jaroon Rungamornrat, Ph.D.

Accepted by the Faculty of Engineering, Chulalongkorn University in Partial Fulfillment of the Requirements for the Doctoral Degree

………………………………….…… Dean of the Faculty of Engineering

(Associate Professor Boonsom Lerdhirunwong, Dr.Ing.)

THESIS COMMITTEE

………………………………...…….. Chairman

(Professor Teerapong Senjuntichai, Ph.D.)

…………………………………………. Thesis Advisor

(Assistant Professor Chatpan Chintanapakdee, Ph.D.)

…………………………………...…….. Thesis Co-advisor

(Assistant Professor Jaroon Rungamornrat, Ph.D.)

……………………………….…...…….. Examiner

(Assistant Professor Watanachai Smittakorn, Ph.D.)

……………………………….…...…….. Examiner

(Associate Professor Akhrawat Lenwari, Ph.D.)

……………………………….…...…….. External Examiner

(Associate Professor Pruettha Nanakorn, D.Eng)

วีรพร พงศ์ติณบุตร : การวิเคราะห์รอยแตกร้าวในตัวกลาง 3 มิติที่ทำมาจากวัสดุไพอิโซอิเล็กทริกเชิงเส้น. (ANALYSIS OF FRACTURES IN 3D LINEAR PIEZOELECTRIC MEDIA) อ. ที่ปรึกษาวิทยานิพนธ์หลัก : ผศ.ดร.ฉัตรพันธ์ จินตนาภักดี, อ. ที่ปรึกษาวิทยานิพนธ์ร่วม : ผศ.ดร.จรูญ รุ่งอมรรัตน์, 125 หน้า.

วิทยานิพนธ์ฉบับนี้นำเสนอระเบียบวิธีการคำนวณเชิงตัวเลขที่เรียกว่า ระเบียบวิธีบาวดารีเอเลเมนต์แบบสมมาตรกาเลอร์คินที่มีความเป็นเอกฐานอย่างอ่อน มาใช้ในการวิเคราะห์ปัญหารอยแตกร้าว 3 มิติในตัวกลางไพอิโซอิเล็กทริกที่มีพฤติกรรมเป็นแบบเชิงเส้นภายใต้คุณสมบัติแอนไอโซทรอปิก ทั้งในโดเมนต์แบบไร้ขอบเขตและโดเมนต์ที่มีขอบเขต ภายใต้เงื่อนไขขอบเขตเชิงไฟฟ้าแบบต่างๆ จุดเด่นอย่างหนึ่งของระเบียบวิธีที่นำเสนอนี้ คือ สมการควบคุมสำหรับวิเคราะห์ปัญหารอยแตกร้าวมีความสมมาตร ซึ่งได้จากการนำสมการ 2   ชุดมาใช้ร่วมกัน กล่าวคือ สมการชุดแรกถูกนำมาใช้กับบริเวณที่ทราบค่าการกระจัดและศักย์ไฟฟ้า ส่วนสมการชุดที่สองจะถูกนำมาใช้กับบริเวณที่ทราบค่าของแรงฉุดลาก (traction) และประจุไฟฟ้าที่ผิว (surface electric charge) นอกจากนี้เคอร์เนลที่ปรากฎในสมการทั้งสองยังมีความเป็นเอกฐานอย่างอ่อนจึงทำให้สามารถเลือกใช้ฟังก์ชันรูปร่างที่มีความต่อเนื่อง (C^0) ในการประมาณค่าหาคำตอบด้วยวิธีกาเลอร์คินได้อีกด้วย ข้อดีประการต่อมาก็คือการประยุกต์ใช้เอเลเมนต์ชนิดพิเศษที่บริเวณติดกับขอบของรอยแตกร้าว   ซึ่งผลจากการประยุกต์ใช้เอเลเมนต์ชนิดพิเศษนี้ พบว่าค่าตัวประกอบความเข้มของความเค้นและของไฟฟ้าที่คำนวณได้มีความถูกต้อง ถึงแม้ว่าจะใช้จำนวนเอเลเมนต์ชนิดพิเศษนี้ที่บริเวณขอบของรอยแตกร้าวเพียงไม่กี่ชิ้นก็ตาม และจากการทดลองวิเคราะห์ปัญหารอยแตกร้าวในตัวกลางไพอิโซอิเล็กทริกสำหรับทั้งโดเมนต์แบบไร้ขอบเขตและโดเมนต์ที่มีขอบเขต ในกรณีศึกษาต่างๆ ที่มีผลเฉลยแบบแม่นตรงมาเปรียบเทียบ พบว่า ระเบียบวิธีที่นำเสนอนี้สามารถคำนวณค่าตัวประกอบความเข้มของความเค้นและของไฟฟ้าได้อย่างถูกต้อง นอกจากนี้ระเบียบวิธีที่ทำเสนอนี้ยังสามารถวิเคราะห์ปัญหารอยแตกร้าวที่มีความซับซ้อนได้อย่างมีประสิทธิภาพ และในส่วนสุดท้ายของวิทยานิพนธ์ฉบับนี้ยังได้เปิดเผยให้เห็นถึงอิทธิพลของเงื่อนไขขอบเขตทางไฟฟ้าแบบต่าง ๆ ที่มีต่อค่าตัวประกอบความเข้มของความเค้นและของไฟฟ้าในตัวกลางไพอิโซอิเล็กทริก ทั้งในโดเมนต์แบบไร้ขอบเขตและในโดเมนต์ที่มีขอบเขต

ภาควิชา ....วิศวกรรมโยธา................... ลายมือชื่อนิสิต ....

สาขาวิชา ....วิศวกรรมโยธา................... ลายมือชื่อ อ.ที่ปรึกษาวิทยานิพนธ์หลัก ....

ปีการศึกษา ....2554.................... ลายมือชื่อ อ.ที่ปรึกษาวิทยานิพนธ์ร่วม ....

4971889221 : MAJOR CIVIL ENGINEERING

KEYWORDS : PIEZOELECTRIC MATERIALS / CRACKS / FINITE DOMAINS / WEAKLY SINGULAR / SGBEM

WEERAPORN PHONGTINNABOOT : ANALYSIS OF FRACTURES IN 3D LINEAR PIEZOELECTRIC MEDIA. ADVISOR : ASST. PROF. CHATPAN CHINTANAPAKDEE, Ph.D., CO-ADVISOR : ASST. PROF. JAROON RUNGAMORNRAT, Ph.D., 125 pp.

This paper presents a numerical technique called a weakly singular, symmetric Galerkin boundary element method (SGBEM) that can be used to analyze cracks in three-dimensional, generally anisotropic, linear piezoelectric infinite and finite media under various types of electrical boundary conditions including impermeable, permeable, semi-permeable and Landis-type conditions. One of advantage features of the present technique is that the governing equations are in symmetric forms, which are obtained by using two sets of boundary integral equations: the first one is the integral equation for the generalized displacement (i.e. displacement and electric potential) and the other one is the integral equation for the generalized traction (i.e. traction and surface electric charge). Since such pair of integral equations contain only weakly singular kernels of $\mathbb{O}(1/r)$, the standard C^o-interpolation functions can be employed to approximate the solutions by using the Galerkin scheme. Another positive feature is the use of special crack tip elements along the local region of the crack front to accurately model the near tip field. As a result, the stress and electric intensity factors can therefore be obtained accurately by using relatively coarse meshes. The weakly singular SGBEM is validated through various numerical experiments for both infinite and finite boundary value problems under several types of electrical boundary conditions. It was found that obtained results for a penny-shaped crack are in excellent agreement with the exact solutions. Subsequently, more complex problems are treated to demonstrate the versatility of the current technique to model cracks and bodies of various geometries under various loading conditions. Finally, the influence of electrical boundary conditions on the stress intensity factors and the electric intensity factor for piezoelectric infinite and finite media is thoroughly investigated.

Department: ……………………………… Student 's Signature: ……………………..
Civil Engineering

Field of Study: …………………………… Advisor 's Signature: ……………..……...
Civil Engineering

Academic Year: ……………………..... Co-advisor 's Signature: …………………...
2011

ACKNOWLEDGEMENTS

CONTENTS

Page

LIST OF TABLES

Page

LIST OF FIGURES

Page

Page

LIST OF ABBREVIATIONS

D_i	electric induction vectors in the i-direction
E_i	electric fields in the i-direction
E_{iJKm}	generalized moduli
E_{ijkm}	elastic constants
e_{mij}	piezoelectric constants
G_{tK}^J	weakly singular kernels of $\mathcal{O}(1/r)$
n_i	outward unit normal vector in the i-direction
S_{iJ}^P	generalized stress fundamental solution
S_c^+	upper crack surfaces
S_c^-	lower crack surfaces
S_o	ordinary boundary of the body
S_t	surface on which the generalized traction is prescribed
S_u	surface on which the generalized displacement is prescribed
$\mathbf{T}$	vector of nodal quantities of the generalized traction
t_J	generalized surface traction
t_i	mechanical traction in the i-direction
$\mathbf{U}$	vector of nodal quantities of the generalized displacement
U_J^P	generalized displacement fundamental solution
u_i	mechanical displacement vectors in the i-direction
u_K	generalized displacement vectors
$\mathbf{x}$	interior point within the domain
$\mathbf{z}$	unit vector
$\Delta\mathbf{U}$	vector of nodal quantities associated with the jump of the generalized displacement
ε_{ij}	strain components
ϕ	electric potential

κ_c dielectric permittivity of the medium inside the crack gap

κ_{im} dielectric permittivities of piezoelectric material

σ_{ij} stress components

ξ point located on the surface

CHAPTER I

INTRODUCTION

1.1 General

It is well known that piezoelectric materials exhibit coupling effect between mechanical and electric fields. As the results, they produce electric field when deformed under mechanical loadings and undergo deformation when subjected to an electrical field. For this reason, piezoelectric materials have been widely used in various engineering and industrial applications such as sensors (e.g. sonar), actuators (e.g. ultrasonic cleaner, ultraprecision positioner, ink jet print head) and signal transmitters (e.g. cellular phone, remote car opener) (Denda and Mansukh, 2005). However, the main disadvantage is that piezoelectric materials are in general brittle and susceptible to fracture either during manufacturing process or during applications. Presence of fractures in such materials can produce stress concentration, reduce the global strength, induce fatigue and damage, and finally lead to ultimate failure and reduction of lifespan and performance of the components. This therefore necessitates extensive investigations to gain an insight into fracture behavior of piezoelectric materials.

Due to complex electro-mechanical coupling and anisotropic nature of the piezoelectric material, responses of a piezoelectric body under various mechanical and electric loading conditions are consequently very sophisticated and generally inaccessible. Furthermore, the situation becomes more intricate when discontinuities such as dislocations and flaws are additionally present within the body. To construct a physically sound but sufficiently simple mathematical model to mimic such physical problems to the level of complexity involved, various assumptions and simplifications must be integrated. For the past two decades, a simplified mathematical model based upon a linear constitutive law has increasingly gained popularity and extensively been employed by various investigators to model a variety of physical problems involving piezoelectric materials. In addition to its simplicity, the linear piezoelectricity assumption has found well-suited and sufficient for the response prediction of a wide range of practical applications.

Within the context of linear piezoelectricity, analysis of a body containing no crack has been well-established in comparison with that concerning cracked bodies. This is due primarily to complexity of electric and elastic fields induced in the neighborhood of the crack; in particular, the singularity of such fields exists along the crack front. As a result, existing solutions of such boundary value problems are rather limited. While various analytical techniques have been developed to study fractures in linear piezoelectric media, the main objective to construct close-form or analytical solutions is their key drawback and poses restrictions on their capability. Most of existing works are limited only to cracks of simple geometries, under simple loading conditions, and contained in an infinite medium (Park and Sun, 1995; Xu and Rajapakse, 2001; Wang and Jiang, 2002; Wang and Mai, 2003; Chen and Lim, 2005; Chiang and Weng, 2007). According to such limitations, numerical techniques have recently become more attractive alternatives in the modeling due to their vast features and potential capability to solve complex and large scale boundary value problems.

The boundary integral equation methods (BIEMs) have proven to be one of the most efficient numerical techniques for analysis of fractures in linear homogeneous media. One crucial advantage of these methods (over other domain-based techniques) is that the key governing equations involve only integrals over the boundary of a domain and the crack surface; this therefore reduces dimensions of the problem by one. In terms of computational efficiency, the boundary integral equation methods only require discretization of the boundary and the crack surface rather than the entire domain; this significantly reduces preprocessing effort corresponding to the mesh generation. While the framework of BIEMs for modeling of fractures in linear elastic media has been well-established, a significantly less number of investigations has been found within the context of piezoelectric materials and this motivates the present study.

1.2 Literature Review

In this section, a brief overview of the background and existing works relevant to the current study is provided. The key objective is to demonstrate the sequence of historical development in this special area and, more importantly, to indicate the gap of knowledge and originality of the current work. Results from extensive literature

survey are organized in two separate subsections regarding to their main focus. First, works on development of boundary integral equation methods are intensively explored and then various studies on influence of electric boundary conditions on fracture behavior are discussed.

1.2.1   Boundary integral equation methods (BIEMs)

It is well-known that the conventional boundary integral equation for the generalized displacement (i.e. the elastic displacement and the electric potential) is efficient only for treatment of bodies containing no crack. This is due to the fact that the integral equation for the generalized displacement, when applied to cracks, is mathematically degenerate. Complete information of the generalized surface traction (i.e. traction and surface electric charge) is lost as a consequence of geometrically coincident crack surfaces. Nevertheless, such equation was still employed by Sanz *et al*. (2005) along with the domain decomposition technique to model cracks in three-dimensional piezoelectric media. The domain decomposition technique was utilized to partition the domain into several parts along the crack surfaces to circumvent the degenerate problem. Unfortunately, introduction of fictitious interfaces may generates a vast number of extra unknowns and, more importantly, such partition is impractical for multiple and nonplanar cracks (Davi and Milazzo, 2001; Groh and Kuna, 2005; Wippler and Kuna, 2007).

An alternative to handle this mathematical degeneracy is to exploit a boundary integral equation for the generalized traction to model cracks (Pan, 1999; Chen, 2003a; Chen, 2003b; Qin and Noda, 2004; Qin *et al*., 2007). Pan (1999) proposed a single-domain-based boundary element method for analysis of cracks in two-dimensional piezoelectric media. In his development, an extended strongly singular displacement integral equation is applied to the outer boundary of the domain (excluding the crack surface) while an extended hypersingular traction integral equation is applied to the crack surface. Chen (2003a) derived a hypersingular generalized surface traction boundary integral equation for cracks in three-dimensional infinite media and, later, Chen (2003b) used such integral equation to implement a hypersingular boundary element method to investigate cracks of various configurations. Qin and Noda (2004) developed the Green's functions and the

hypersingular generalized surface traction integral equation for cracks in three-dimensional transversely isotropic piezoelectric infinite media. However, no numerical implementation of the integral equation was presented in their work. Later, Qin *et al*. (2007) utilized the integral equation from Qin and Noda (2004) to establish a hypersingular boundary element method and used such technique to compute stress and electric intensity factors for isolated cracks. While BIEMs mentioned above can overcome the degeneracy problem induced by the presence of cracks, the generalized surface traction boundary integral equation employed is still hypersingular. Presence of hypersingular kernels in such integrals poses several difficulties including interpretation of their values, numerical evaluation and the strong continuity requirement on the boundary data (Martin and Rizzo, 1996; Chen, 2003b; Qin *et al*., 2007).

To circumvent such key drawback, various regularization techniques have been proposed to reduce the strength of singularity of kernels appearing in the boundary integral equations before used in the numerical implementation. Many forms of regularized boundary integral equations were derived within the context of cracks in elastic media; for instance, the regularization from hypersingular to strongly singular integral equations was carried out successfully by Bui (1977), Weaver (1977) and Sladek and Sladek (1982), and the completely regularized integral equations containing only weakly singular kernel of $\mathbb{O}(1/r)$ were extensively investigated by several researchers such as Gu and Yew (1988), Xu and Ortiz (1993), Li and Mear (1998), and Rungamornrat and Mear (2008a). It can be emphasized that the latter type of singularity-reduced integral equations are attractive and to be sought in the present study since the presence of weakly singular kernels in all involved integrals renders their values existing in an ordinary sense, requires much simpler numerical quadrature and, in addition, alleviates the continuity requirement of boundary data for the integrals to be valid. The last feature allows continuous interpolations to be employed in the approximation of primary unknowns on the boundary. Such weakly singular integral equations forms the basis for the development of a well known BIEM called a weakly singular symmetric Galerkin boundary element method (SGBEM) for analysis of cracks (Li *et al*., 1998; Frangi *et al*., 2002; Rungamornrat and Mear, 2008b).

While the regularized boundary integral equations and the weakly singular SGBEM have been extensively investigated in the context of linear elastic media, relatively few studies relevant to fracture modeling in piezoelectric media have been found. Recently, Rungamornrat and Mear (2008c) established a weakly singular, weak-form generalized surface traction integral equation for cracks in three-dimensional, generally anisotropic, linear piezoelectric media and used such equation to implement a weakly singular SGBEM to solve cracks of various geometries and under different loading conditions. However, their development is still restricted to isolated cracks in an infinite piezoelectric medium. Most recently, Solis *et al.* (2009) established the generalized displacement and generalized surface traction integral equations for treatment of cracks in linear piezoelectric finite domains. In their formulation, the subtraction technique was employed to regularize both the boundary integral equations and they claimed that the resulting integral equations are completely regularized. However, from the careful mathematical consideration, both integral equations still require the boundary data to be of the type $C^{1,\alpha}$ for the integrals to be valid. This strong continuity requirement must be satisfied either by the use of C^1 elements or by collocating the integral equations at interior points. Use of C^1 elements in two dimensions is computationally inefficient while the significant drawback of collocating in the interior is that the interpolation is discontinuous along the element inter-boundary. In addition, their development was restricted only to a specific class of piezoelectric materials called transversely isotropic piezoelectric materials. On the basis of an extensive literature survey, work towards the development of weakly singular SGBEM capable of modeling cracks in three-dimensional, piezoelectric finite bodies has not been found and thus deserves a rigorous investigation.

1.2.2 Influence of electrical boundary conditions

One of the most challenges in studying fracture mechanics of piezoelectric media, besides to determine the electroelastic fields around the fracture front in materials that exhibit fully mechanical and electrical coupling effect as well as strongly anisotropic behavior, is to appropriately model electrical boundary conditions on the

crack surface. This issue not only increases the complication in analysis of crack in piezoelectric materials but also become more interested to many researchers (Xu and Rajapakse, 2001; Wang and Jiang, 2002; Wang and Jiang, 2004; Li and Lee, 2004; Chiang and Weng, 2007).

According to various earlier studies (Motola and Banks-Sills, 2009; Chen and Lim, 2005; Nam and Watanabe, 2008), several types of electrical boundary conditions (e.g. electrically permeable boundary condition, electrically impermeable boundary condition, electrically semi-permeable boundary condition, Landis-type boundary condition proposed by Landis (2004), etc.) have been employed and discussed. Each type of electrical boundary conditions has their own characteristics and is applicable to and suitable for different situations due to the underlying assumptions and simplifications (Parton, 1976; Deeg, 1980; Hao and Shen, 1994; Ou and Chen, 2003; McMeeking, 2004; Landis, 2004). Consequently, the electro-mechanical behavior and electroelastic field of a cracked piezoelectric material are completely different based on the electrical boundary conditions adopted at the crack surfaces. Therefore, the selection of electrical boundary conditions, which represent more realistic fracture behavior of piezoelectric cracked media, is very important in this research area. However, understanding of the fracture behavior of piezoelectric cracked bodies under each type of electrical boundary conditions is a prerequisite.

The electrically permeable boundary condition was originally proposed by Parton (1976). For this particular boundary condition, both the electric potential and the electric induction normal to the crack surface are continuous across the crack surface. This assumption implies that there is no jump of the electric potential across the crack surfaces, or in the other word, there is no electric potential drop across the crack surfaces. However, as discussed by Suo *et al*. (1992), the permeable assumption cannot be represented a realistic crack. Because the medium inside the crack gap (e.g. air) has the permittivity much lower than the piezoelectric solid and, as a result, the crack occurs in the piezoelectric media may be considered as a low capacitance medium and it should cause the electric potential drop across the crack surfaces. Such discussion is in agreement with the work of Schneider *et al*. (2003), who performed the experimental studies for investigating an indentation crack embedded in a poled PZT ceramic and found that there is an electric potential drop across the upper and lower

crack faces. Nevertheless, in some cases, this boundary condition is an acceptable model. As pointed out by Ou and Chen (2007), the permeable boundary condition was a reasonable assumption when the crack opening is sufficiently small (i.e. sharp crack or slit crack). Many investigators employed such electrical boundary condition to investigate simple cracks in an infinite domain under remote mechanical and electric loadings (Kogan *et al.*, 1996; Chen and Lim, 2005). Similar results were also reported; in particular, for a penny-shaped crack under applied remote uniform tensile stresses and electric induction, the mode-I stress intensity factor depends only on the mechanical loading whereas the electric intensity factor is independent of the electric loading but depends primarily on both the mechanical loading and material properties.

Another simple type of electrical boundary conditions called "electrically impermeable boundary condition" was utilized by Deeg (1980). For this case, the electric induction normal to the crack surface was assumed to identically vanish on both sides of the crack surface, whereas the electric potential was unknown a priori. However, Gao and Fan (1999) and Ou and Chen (2003) indicated that the impermeable boundary conditions are not well-suited for modeling real cracks since such conditions are physically unreasonable and can leads to a false prediction of the singularity. In addition, several investigators pointed out that the modeling based on the impermeable boundary conditions may lead to erroneous results and conclusions (Dunn, 1994; Sosa and Khutoryansky, 1996; McMeeking, 1999; McMeeking, 2001). Nevertheless, the impermeable boundary condition is still valid when the crack opening is sufficiently large as indicated by Pak (1992) and McMeeking (2004). Due to its simplicity, this assumption has widely been used in the modeling either by analytical approaches or numerical techniques (Park and Sun, 1995; Chen *et al.*, 2000; Jiang and Sun, 2001; Sanz *et al.*, 2005; Qin *et al.*, 2007; Rungamornrat and Mear, 2008c; Solis *et al.*, 2009). Extensive results obtained for a straight crack and a penny-shape crack in two-dimensional and three-dimensional infinite media revealed the same conclusion that under the remote uniform tensile stress and electric induction, the mode-I stress intensity factor depends only on the magnitude of the applied mechanical load (identical to the permeable case). However, the electric intensity factor, for this particular type of electrical boundary condition, is independent of both

the material properties and the mechanical load but depends strongly on the magnitude of the electric load (opposite to the permeable case).

Since the medium inside the opened crack has non-zero permittivity and the above two conditions ignore the contribution of such medium, Hao and Shen (1994) proposed a new type of electrical boundary conditions by incorporating the permittivity of the medium within the crack opening. In this case, the normal component of the electric induction at the crack surface depends on the jump of mechanical displacement, the jump of electric potential, and the permittivity of the medium inside the crack. This assumption is known as either Hao&Shen-type boundary condition or electrically semi-permeable boundary condition. It is well known that the impermeable and permeable conditions are two extreme cases of the semi-permeable assumption. By assuming the dielectric constant within the crack vanishes, the semi-permeable condition can be reduced directly to the impermeable condition. While the permeable assumption is equivalent to assuming that the jump of mechanical displacement disappears, this implies that the upper and lower crack surfaces are always in contact or, equivalently, the crack is always closed. Consequently, Ou and Chen (2003) pointed out that the permeable boundary condition can only be used along with nonzero mechanical traction boundary conditions on the crack surfaces. In addition, Ou and Chen (2003) also concluded that the electrical boundary condition proposed by Hao and Shen (1994) is physically sound since the interaction between the media present within the crack gap and the crack surface is treated. Such electrical boundary condition has later gained significant attentions and extensively been employed by several investigators to study cracks in piezoelectric media (Xu and Rajapakse, 2001; Wang and Jiang, 2002; Wang and Jiang, 2004; Li and Lee, 2004; Chiang and Weng, 2007). It was also reported that under remote uniform tensile stress and electric induction, the mode-I stress intensity factor of a penny-shaped crack depends only on the magnitude of the applied mechanical load and such results are identical to those of both permeable and impermeable boundary conditions. However, the electric intensity factor under the semi-permeable boundary condition is different from that for permeable and impermeable boundary conditions. The electric intensity factor of semi-permeable

cracks depends on four parameters such as mechanical loading, electric loading, material properties and the dielectric constant of the medium inside the crack gap.

Since the permittivity of the medium inside the crack gap is considered, the semi-permeable cracks seem to represent the more realistic crack and there is no need another type of electrical boundary conditions. However, McMeeking (2004) examined the energy release rate for a Griffith crack using the Hao&Shen-type boundary condition along with the mechanical traction free boundary conditions. He reported that the total energy release rate is not equivalent to the crack tip energy release rate. To resolve such conflict, Landis (2004) proposed a modified Hao&Shen-type boundary condition by adding extra traction on the crack surface. Such nonzero mechanical traction resulted from the consideration of energetic consistency condition and was directly related to the electric field in the crack gap. Besides the nonlinearity posed by such boundary condition, Landis (2004) was able to prove that the total energy release rate is equivalent to the crack tip energy release rate for a Griffith crack model. Recently, Li *et al*. (2011) pointed out that the mode-I stress intensity factor of a penny-shaped crack under Landis-type cracks depends on both the electric loading and the mechanical loading. Such results were different from those associated with the former three boundary conditions (i.e. permeable, impermeable and semi-permeable boundary conditions) where the mode-I stress intensity factor depends only on the mechanical loading but is independent of the electric loading. Moreover, Li and Chen (2008) and Li *et al*. (2011) also indicated that the non-zero mechanical traction, which is unknown a priori, tend to pull the upper and lower crack surfaces together. This finding is in agreement with the work of Motola and Banks-Sills (2009).

Moreover, many useful results from various investigations of the influence of different types of electrical boundary conditions can also be summarized as follows. For two-dimensional boundary value problems, Xu and Rajapakse (2001) studied an elliptical void of arbitrary orientations in infinite media and were able to retrieve a straight crack as its special limiting case. Results from their study revealed that when a crack is not parallel to the poling direction of a piezoelectric material and subjected to a given remote uniaxial stress and varying remote electric field, the electric intensity factors for permeable and semi-permeable cases are nearly identical. Wang

and Jiang (2002) found that for a given positive electric field, the electric intensity factor for the semi-permeable case varies from that for the permeable condition to that for the impermeable condition as the applied positive mechanical load increases. Moreover, Wang and Jiang (2004) pointed out that under high tensile mechanical loads and the poling direction is perpendicular to the crack surface, the electric intensity factor for the semi-permeable and permeable cases are not identical. In addition, for the applied positive electric field and the poling direction is perpendicular to the crack surface, the impermeable and permeable conditions constitute the upper and lower bound of the semi-permeable condition, respectively. Conversely, if the sign of the applied electric field is reversed, the impermeable and permeable conditions become lower and upper bounds of the semi-permeable condition, respectively.

For three-dimensional boundary value problems, Li and Lee (2004) investigated a penny-shaped crack in transversely isotropic piezoelectric infinite media for various types of electrical boundary conditions. Results from their study agreed with those by Wang and Jiang (2002) and Wang and Jiang (2004). Later, the same problem was reexamined by Chiang and Weng (2007). They proposed a critical state for (applied remote) both positive and negative electric inductions. The critical state consists of the critical stress and the applied remote electric inductions. Under positive remote electric induction, the critical state depends on material properties (the material properties for the four type of PZT were also given by Chiang and Weng, 2007). In addition, the critical stress is computed from applied remote positive electric induction divided by material properties. Moreover, they reported that when remote tensile stress is less than the critical stress, the electric intensity factor of the impermeable and permeable are upper bound and lower bound of semi-permeable boundary condition, respectively. On the other hand, when the remote tensile stress is greater than the critical stress, the electric intensity factor of impermeable and permeable cases are lower bound and upper bound of the semi-permeable case, respectively. Under negative remote electric induction, the critical state is at the origin and independent of the material properties.

As discussed above, most of previous studies have focused primarily on planar cracks (i.e. a penny-shaped crack and a straight crack) embedded in piezoelectric

media. A question arises as what is the fracture behavior of non-planar cracks or curvilinear cracks in such materials. Recently, Rungamornrat and Mear (2008c) successfully developed a weakly singular, symmetric Galerkin boundary element method (SGBEM) for analyzing an arbitrary shaped crack, in a three-dimensional, generally anisotropic, linear piezoelectric infinite media. They found that, in the case of spherical cap crack, the mechanical loading can cause the mode-I and mode-II stress intensity factors, including, the electric intensity factor and vice versa. These results are in contrast with those found in the case of a planar crack embedded in an infinite domain under impermeable boundary condition where the mechanical and electrical loadings are uncoupled. However, the work of Rungamornrat and Mear (2008c) was still restricted to cracks subjected to an electrically impermeable boundary condition.

Moreover, the investigation of three-dimensional, piezoelectric finite cracked body conducted by Sanz *et al.* (2005) and Solis *et al.* (2009) revealed that the uniform mechanical traction loading can cause the mode-I stress intensity factor and the electric intensity factor and vice versa. Again, these results are different from that found in the case of a planar crack embedded in an unbounded domain under the impermeable boundary condition. Again, the work of Sanz *et al.* (2005) and Solis *et al.* (2009) are still limited only to impermeable cracks.

The limitation of the work of Rungamornrat and Mear (2008c), Sanz *et al.* (2005) and Solis *et al.* (2009) motivates the current study to explore the fracture behavior of piezoelectric infinite and finite cracked media under several types of electrical boundary conditions (i.e. electrically permeable boundary condition, electrically impermeable boundary condition, electrically semi-permeable boundary condition and Landis-type boundary condition).

1.3 Research Objectives

1)   Develop mathematical models and efficient computational techniques for analysis of cracks in piezoelectric media

2)   Investigate the influence of various electrical boundary conditions on the intensity factors along the crack front

1.4 Scope

1)   The development is carried out within a context of three-dimensional boundary value problems including both infinite and finite media.

2)   Piezoelectric materials to be treated are homogeneous, linear and generally anisotropic.

3)   Four types of electrical boundary conditions, (i) electrically permeable, (ii) electrically impermeable, (iii) electrically semi-permeable and (iv) Landis-type boundary conditions, are investigated.

1.5 Research Significance

1)   Accurate computational strategies such as the one developed in the current study could be beneficial through their use in supporting careful experimental studies and as a tool for analysis and simulation of fracture phenomena of piezoelectric media.

2)   Gain an insight into the behavior of cracks including fracture information along the crack front under various electrical boundary conditions.

1.6 Research Methodology

1)   A pair of completely regularized integral equations for the generalized displacement and the generalized surface traction is established by using a systematic regularization technique (i.e., an integration by parts via Stokes' theorem along with two special decompositions of involved kernels), which was proposed by Rungamornrat and Mear (2008c). Subsequently, this set of boundary integral equations is utilized to formulate a set of governing equations to treat cracks in three-dimensional, generally anisotropic, piezoelectric finite and infinite media.

2)   A set of symmetric weak-form boundary integral equations, which is developed in the previous step, along with certain numerical treatments (e.g., discretization, numerical integration of double surface integrals and evaluation of weakly singular kernels) leads to a system of linear algebraic equations.

3) The resulting system of linear algebraic equations is sufficient for solving the unknown degrees of freedom (i.e. the generalized traction and generalized displacement on the ordinary boundary of body, and the jump of generalized displacement along the crack front) for the impermeable and permeable cracks. However, such system of linear equations is not sufficient to determine all unknowns for semi-permeable and Landis-type cracks. As a result, additional equations associated with the electrical boundary conditions on the crack surface are enforced by using the weight residual technique. Finally, the system of linear equations and the resulting non-linear additional conditions form a complete set of equations to solve for all unknowns. Newton-Raphson method is utilized to obtain the numerical solution of such non-linear equations.

4) Once the unknown data on the boundary are obtained for any types of electrical boundary conditions, the stress intensity factors and the electric intensity factor are computed from the nodal data along the crack front using the special formula proposed by Rungamornrat and Mear (2008c).

CHAPTER II

THEORETICAL CONSIDERATIONS

This chapter first presents a set of basic field equations governing a body constituting a linear piezoelectric material. Standard boundary integral relations for the generalized displacement and generalized stress are then obtained for cracks in a piezoelectric medium. Such integral relations are employed along with a systematic regularization procedure to derive a pair of completely regularized boundary integral equations for the generalized displacement and generalized surface traction. Subsequently, the symmetric formulation is established as a basis for the development of a symmetric Galerkin boundary element method (SGBEM) and other involved numerical techniques. Finally, the treatment of remote conditions using the principle of superposition is discussed.

2.1 Basic Equations

In the absence of body forces and body electric charges, a set of field equations governing a linear piezoelectric body, i.e. (i) conservation of forces and electric charges, (ii) strain-displacement and electric field-electric potential relations and (iii) constitutive model for linear piezoelectricity, can be expressed as

$$\frac{\partial \sigma_{ij}}{\partial x_i} = 0; \qquad \frac{\partial D_i}{\partial x_i} = 0 \tag{2.1}$$

$$\varepsilon_{ij} = \frac{1}{2}(u_{i,j} + u_{j,i}) \qquad E_i = -\phi_{,i} \tag{2.2}$$

$$\sigma_{ij} = E_{ijkm}\varepsilon_{km} + e_{mij}\phi_{,m}; \qquad D_i = e_{ikm}\varepsilon_{km} - \kappa_{im}\phi_{,m} \tag{2.3}$$

where σ_{ij}, ε_{ij}, u_i, D_i, and E_i are components of the stress tensor, strain tensor, displacement vector, electric induction vector and electric field, respectively; ϕ is the electric potential; E_{ijkm} are elastic constants; e_{mij} are piezoelectric constants; and κ_{im}

are dielectric permittivities. For brevity and convenience in the presentation of results derived further, the field equations (2.1)-(2.3) can be compressed in a concise form as

$$\frac{\partial \sigma_{iJ}}{\partial x_i} = 0 \tag{2.4}$$

$$\sigma_{iJ} = E_{iJKm} \frac{\partial u_K}{\partial x_m} \tag{2.5}$$

where σ_{iJ} ($i \in \{1,2,3\}$ and $J \in \{1,2,3,4\}$) is termed as the "generalized stress" defined such that σ_{ij} are components of the stress tensor and $\sigma_{i4} = D_i$ are components of the electric induction vector; u_K ($K \in \{1,2,3,4\}$) is termed as the "generalized displacement" defined such that u_k are components of the displacement vector and $u_4 = \phi$ is the electric potential; and E_{iJKm} ($J,K \in \{1,2,3,4\}$) which is termed as the "generalized moduli" is defined such that E_{ijkm} represents the elastic constants, $E_{ij4m} = E_{m4ji}$ represents the piezoelectric constant and $-E_{i44m} = -E_{m44i}$ represents the dielectric permittivities. Note that from now to what follows, lower case indices range from 1 to 3 whereas upper case indices range from 1 to 4, and repeated indices are taken to imply summation over the range of those indices. Further, the "generalized surface traction" t_J at any point on a sufficiently smooth surface is defined by $t_J = \sigma_{iJ} n_i$ where n_i denotes an outward unit normal to the surface. Consistent with above notations, $t_j = \sigma_{ij} n_i$ represents components of the traction whereas $t_4 = \sigma_{i4} n_i$ represents the surface electric charge.

Besides the basic field equations presented above, the boundary conditions (BCs) on the outer boundary and the crack surfaces, i.e. the mechanical and the electrical conditions, are essential information that must properly be defined in the analysis of cracks in piezoelectric media. Since such information, especially the boundary conditions on the crack surfaces, has significant influence on both the behavior and essential information present along the crack front. For this study, the uncoupled mechanical-electrical BCs are considered at the outer boundary, while the boundary conditions at the crack surfaces can be classified into two groups, one

associated with uncoupled mechanical-electrical BCs (i.e. permeable and impermeable assumptions) and the other corresponding to fully coupled mechanical-electrical BCs (e.g. semi-permeable and Landis assumptions). Four types of cracks focused in this study are summarized below.

(1) <u>Impermeable cracks</u>: t_I^+, t_I^- are prescribed whereas Δu_J are unknowns.

(2) <u>Permeable cracks</u>: t_i^+, t_i^- are prescribed, $\Delta u_4 = 0$ whereas Δu_i, t_4^+ are unknowns.

(3) <u>Semi-permeable cracks</u>: t_i^+, t_i^- are prescribed, whereas Δu_I, t_4^+ are unknowns and satisfy $t_4^+ \Delta u_i n_i = \kappa_c \Delta u_4$.

(4) <u>Landis-type cracks</u>: t_{tangent}^+, t_{tangent}^- are prescribed, whereas Δu_I, t_{normal}^+, t_4^+ are unknowns and satisfy $t_4^+ \Delta u_i n_i = \kappa_c \Delta u_4$, $\sigma_{\text{normal}} = (1/2)\kappa_c (\Delta u_4)^2 / (\Delta u_i n_i)^2$.

where t_I^+ and t_I^- denote the generalized tractions on the upper and lower crack surfaces, respectively, Δu_J denote the jump of the generalized displacement across the crack surface, κ_c is the dielectric permittivity of the medium inside the crack; and t_{normal}^+ and t_{tangent}^+ denote the traction normal and tangent to the upper crack surface.

2.2 Standard Integral relations

Consider a linear, homogeneous, generally anisotropic piezoelectric finite body, denoted by Ω, containing a crack as shown schematically in Fig. 2.1. The ordinary boundary of the body, denoted by S_o, can be decomposed into two surfaces: a surface S_u on which the generalized displacement is prescribed and a (compliment) surface S_t on which the generalized traction is prescribed. The crack surface consists of the upper and the lower crack surfaces, denoted by S_c^+ and S_c^-; it is sufficient and standard to characterize the crack geometry only by a single surface S_c^+. For convenience in the following development, a surface $S = S_o \cup S_c^+$ is defined as the total boundary of the domain. In addition to the absence of body forces and body electric charges, all involved boundaries including the crack surface are assumed to be piecewise smooth; i.e. the outward unit normal is piecewise well-defined. In the present study, the prescribed generalized traction is self equilibrated, i.e.,

$\mathbf{t}^+ = -\mathbf{t}^- = \mathbf{t}_c$ where $\mathbf{t}^+$ and $\mathbf{t}^-$ are generalized tractions on the upper and lower crack surfaces respectively, and $\mathbf{t}_c$ is a given function.
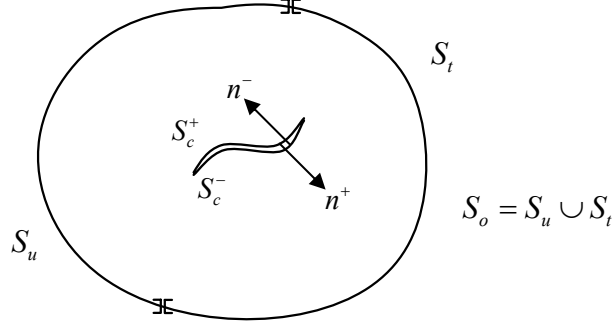
Fig. 2.1. Schematic of a linear piezoelectric body containing a crack.

By generalizing a conventional Somigliana's identity for linear elasticity to a linear piezoelectric body containing a crack, it leads to

$$u_P(\mathbf{x}) = \int_{S_o} U_J^P(\xi - \mathbf{x}) t_J(\xi) dS(\xi) - \int_S S_{iJ}^P(\xi - \mathbf{x}) n_i(\xi) \upsilon_J(\xi) dS(\xi) \tag{2.6}$$

where $\mathbf{x}$ is any interior point, $U_J^P(\xi - \mathbf{x})$ is the generalized displacement fundamental solution, $S_{iJ}^P(\xi - \mathbf{x})$ is the corresponding generalized stress (sometimes called the generalized stress fundamental solution), and

$$\upsilon_J(\xi) = \begin{cases} u_J(\xi); & \xi \in S_o \\ u_J^+(\xi) - u_J^-(\xi); & \xi \in S_c^+ \end{cases}. \tag{2.7}$$

The relation is in fact the boundary integral relation of the generalized displacement at any interior point $\mathbf{x}$ in terms of data on the entire boundary including the crack surface. It is worth noting that the integral relation (2.6) merely involves a single crack surface S_c^+ due to the continuity of the fundamental solutions and geometric coincidence of both crack surfaces S_c^+ and S_c^-, and that the fundamental solutions $U_J^P(\xi - \mathbf{x})$ and $S_{iJ}^P(\xi - \mathbf{x})$ are singular only at $\xi = \mathbf{x}$ of order $\mathcal{O}(1/r)$ and $\mathcal{O}(1/r^2)$ where $r = |\xi - \mathbf{x}|$, respectively. The explicit expression of the fundamental solution $U_J^P(\xi - \mathbf{x})$, obtained by solving a system of partial differential equations via the

Radon transform method (Bacon *et al.*, 1978; Deans, 1983; Gel'fand *et al.*, 1966; Helganson, 1999), is given by

$$U_J^P(\boldsymbol{\xi} - \mathbf{x}) = \frac{1}{8\pi^2 r} \oint_{\mathbf{z} \cdot \mathbf{r} = 0} (\mathbf{z}, \mathbf{z})_{JP}^{-1} \, ds(\mathbf{z}) \qquad (2.8)$$

where $\mathbf{z}$ is a unit vector, $(\mathbf{z}, \mathbf{z})_{IJ} = z_m E_{mIJn} z_n$, $(\mathbf{z}, \mathbf{z})^{-1}$ is the inverse of $(\mathbf{z}, \mathbf{z})$ and the line integral is to be evaluated over a unit circle on the plane defined by $\mathbf{z} \cdot \mathbf{r} = 0$. The explicit expression of the fundamental solution $S_{iJ}^P(\boldsymbol{\xi} - \mathbf{x})$ is somewhat lengthy and while not presented here, it can be obtained by a direct substitution of (2.8) into (2.5). Note, in addition, that the boundary integral relation (2.6) involves both the prescribed and unknown data on the boundary and it can only be employed to determine the generalized displacement at any interior point once all unknown quantities on the boundary are solved.

Another boundary integral relation of equal importance to (2.6) is the boundary integral relation for the generalized stress. This relation can readily be obtained by directly substituting (2.6) into the constitutive relation (2.5). The final result is given by

$$\sigma_{lK}(\mathbf{x}) = -\int_{S_o} S_{lJ}^K(\boldsymbol{\xi} - \mathbf{x}) t_J(\boldsymbol{\xi}) dS(\boldsymbol{\xi}) + \int_S \Sigma_{iJ}^{lK}(\boldsymbol{\xi} - \mathbf{x}) n_i(\boldsymbol{\xi}) \upsilon_J(\boldsymbol{\xi}) dS(\boldsymbol{\xi}) \qquad (2.9)$$

where the kernel $\Sigma_{iJ}^{lK}(\boldsymbol{\xi} - \mathbf{x})$ is defined, in terms of the generalized stress fundamental solution and the generalized moduli, by

$$\Sigma_{iJ}^{lK}(\boldsymbol{\xi} - \mathbf{x}) = E_{lKPq} \frac{\partial S_{iJ}^P(\boldsymbol{\xi} - \mathbf{x})}{\partial \xi_q} \qquad . \qquad (2.10)$$

Note that the function $\Sigma_{iJ}^{lK}(\boldsymbol{\xi} - \mathbf{x})$ is singular only at $\boldsymbol{\xi} = \mathbf{x}$ of order $\mathcal{O}(1/r^3)$. Similar to the integral relation for the generalized displacement, (2.9) can be used to determine the generalized stress at any interior point if all data on the entire boundary are known.

Within the context of boundary integral equation methods, the boundary integral relations (2.6) and (2.9) constitute a basis for the development of boundary integral equations governing the primary unknowns on the boundary. It is important to note that the boundary integral equations for the generalized displacement and the generalized surface traction resulting directly from (2.6) and (2.9) via a limit process are strongly singular and hypersingular, respectively. As discussed in many previous investigations (Martin and Rizzo, 1996; Chen, 2003b; Qin *et al.*, 2007), treatment of such integrals cannot be achieved through a standard procedure but it requires special treatment not only on the numerical quadrature but also on the continuity requirement of the boundary data. As one key objective of the current study, a set of singularity-reduced, boundary integral equations well-suited for the numerical treatment are sought.

2.3 Completely Regularized Integral Equations

To establish a pair of singularity-reduced boundary integral equations for the generalized displacement and the generalized surface traction, a systematic regularization technique analogous to that by Rungamornrat and Mear (2008a) is employed. Since the previous work is restricted only to linear elasticity boundary value problems, a proper generalization must be incorporated in order to treat linear piezoelectricity. The crucial ingredients that aid such successful regularization are the following two special decompositions proposed by Rungamornrat and Mear (2008c):

$$S_{iJ}^{P}(\boldsymbol{\xi}-\mathbf{x}) = H_{iJ}^{P}(\boldsymbol{\xi}-\mathbf{x}) + \varepsilon_{ism}\frac{\partial G_{mJ}^{P}(\boldsymbol{\xi}-\mathbf{x})}{\partial \xi_{s}} \quad , \tag{2.11}$$

$$\Sigma_{iJ}^{lK}(\boldsymbol{\xi}-\mathbf{x}) = -E_{iJKl}\delta(\boldsymbol{\xi}-\mathbf{x}) + \varepsilon_{ism}\frac{\partial}{\partial \xi_{s}}\varepsilon_{lrt}\frac{\partial}{\partial \xi_{r}}C_{mJ}^{tK}(\boldsymbol{\xi}-\mathbf{x}) \tag{2.12}$$

where ε_{ism} is a standard alternating symbol, $\delta(\boldsymbol{\xi}-\mathbf{x})$ is a Dirac-delta distribution centered at $\mathbf{x}$, G_{mJ}^{P} and C_{mJ}^{tK} are unknown singular functions to be determined, and $H_{iJ}^{P}(\boldsymbol{\xi}-\mathbf{x})$ is given, independent of the generalized elastic moduli, by

$$H_{iJ}^P(\boldsymbol{\xi} - \mathbf{x}) = -\frac{\delta_{JP}\left(\xi_i - x_i\right)}{4\pi r^3} \tag{2.13}$$

with δ_{JP} denoting a generalized Kronecker delta symbol.

Existence of the decompositions (2.11) and (2.12) results from the fact that $S_{iJ}^P(\boldsymbol{\xi} - \mathbf{x}) - H_{iJ}^P(\boldsymbol{\xi} - \mathbf{x})$ is divergence free with respect to the index "i" and contains no source and that $\Sigma_{iJ}^{lK}(\boldsymbol{\xi} - \mathbf{x}) + E_{iJKl}\delta(\boldsymbol{\xi} - \mathbf{x})$ is divergence free with respect to both indices "i" and "l" and contains no source (also see extensive discussion in the work of Rungamornrat and Mear, 2008a). Another important feature of the decompositions (2.11) and (2.12) is that both systems of differential equations admit an infinite number of solutions for the functions G_{mJ}^P and C_{mJ}^{tK} due to the curl operators $\varepsilon_{ism}\partial(\cdot)/\partial\xi_s$ and $\varepsilon_{lrt}\partial(\cdot)/\partial\xi_l$. In particular, if G_{mJ}^P and C_{mJ}^{tK} are given solutions, it can readily be verified that $G_{mJ}^P + \partial N_J^P/\partial\xi_m$ and $C_{mJ}^{tK} + \partial M_J^K/\partial\xi_m + \partial P_J^K/\partial\xi_t$ for arbitrary, sufficiently smooth functions $\{N_J^P, M_J^K, P_J^K\}$ are also valid solutions.

A particular solution of G_{mJ}^P and C_{mJ}^{tK} can be constructed by solving a system of partial differential equations (2.11) and (2.12). A method of Radon transform similar to that employed by Rungamornrat and Mear (2008a, 2008c) is applied and the final solution are given explicitly in terms of a line integral by

$$G_{mJ}^P(\boldsymbol{\xi} - \mathbf{x}) = \frac{1}{8\pi^2 r}\left(\varepsilon_{abm}E_{aJDc}\right)\oint_{\mathbf{z}\cdot\mathbf{r}=0} z_b z_c\left(\mathbf{z},\mathbf{z}\right)_{DP}^{-1} ds(\mathbf{z}) \ , \tag{2.14}$$

$$C_{mJ}^{tK}(\boldsymbol{\xi} - \mathbf{x}) = \frac{1}{8\pi^2 r}\left(A_{mJdN}^{tKsM}\right)\oint_{\mathbf{z}\cdot\mathbf{r}=0} z_s z_d\left(\mathbf{z},\mathbf{z}\right)_{MN}^{-1} ds(\mathbf{z}) \tag{2.15}$$

with material-dependent constants A_{mJdN}^{tKsM} given by

$$A_{mJdN}^{tKsM} = \varepsilon_{pam}\varepsilon_{pbt}\left(E_{bKNd}E_{aJMs} - \frac{1}{4}E_{aJKb}E_{dNMs}\right) \ , \tag{2.16}$$

And, again, the line integral is to be evaluated over a unit circle on the plane defined by $\mathbf{z}\cdot\mathbf{r} = 0$. It is evident that both the functions G_{mJ}^P and C_{mJ}^{tK} are singular only at $\boldsymbol{\xi} = \mathbf{x}$ of order $\mathcal{O}(1/r)$.

2.3.1 Weakly singular integral equation for generalized displacement

To obtain a weakly singular, weak-form generalized displacement integral equation, it can be proceeded as follows. First, the special decomposition (2.11) is substituted into the boundary integral relation (2.6) and then the result is integrated by part via Stokes' theorem. It leads to an alternative, singularity-reduced boundary integral relation for the generalized displacement:

$$u_P(\mathbf{x}) = \int_{S_o} U_J^P(\boldsymbol{\xi} - \mathbf{x}) t_J(\boldsymbol{\xi}) dS(\boldsymbol{\xi}) + \int_S G_{mJ}^P(\boldsymbol{\xi} - \mathbf{x}) D_m \upsilon_J(\boldsymbol{\xi}) dS(\boldsymbol{\xi})$$
$$- \int_S H_{iJ}^P(\boldsymbol{\xi} - \mathbf{x}) n_i(\boldsymbol{\xi}) \upsilon_J(\boldsymbol{\xi}) dS(\boldsymbol{\xi}) \tag{2.17}$$

where D_m is a surface differential operator defined by

$$D_m = n_i \varepsilon_{ism} \frac{\partial}{\partial \xi_s} \ . \tag{2.18}$$

By taking limit $\mathbf{x} \to \mathbf{y} \in S_o$ of (2.17), we obtain a boundary integral equation for the generalized displacement as

$$c(\mathbf{y}) u_P(\mathbf{y}) = \int_{S_o} U_J^P(\boldsymbol{\xi} - \mathbf{y}) t_J(\boldsymbol{\xi}) dS(\boldsymbol{\xi}) + \int_S G_{mJ}^P(\boldsymbol{\xi} - \mathbf{y}) D_m \upsilon_J(\boldsymbol{\xi}) dS(\boldsymbol{\xi})$$
$$- \int_S H_{iJ}^P(\boldsymbol{\xi} - \mathbf{y}) n_i(\boldsymbol{\xi}) \upsilon_J(\boldsymbol{\xi}) dS(\boldsymbol{\xi}) \tag{2.19}$$

where $c(\mathbf{y}) = 1/2$ if the surface is sufficiently smooth at $\mathbf{y}$ (i.e. the unit normal $\mathbf{n}$ is well-defined at $\mathbf{y}$) otherwise $c(\mathbf{y}) \in (0,1)$ and $u_P(\mathbf{y})$ is the generalized displacement boundary data. Upon multiplying (2.19) by a test function $\tilde{t}_P$ and then integrating the result over the ordinary boundary S_o, we obtain a weakly-singular, weak-form boundary integral equation for the generalized displacement as

$$\frac{1}{2}\int_{S_o}\tilde{t}_P(\mathbf{y})u_P(\mathbf{y})dS(\mathbf{y}) = \int_{S_o}\tilde{t}_P(\mathbf{y})\int_{S_o} U_J^P(\boldsymbol{\xi}-\mathbf{y})t_J(\boldsymbol{\xi})dS(\boldsymbol{\xi})dS(\mathbf{y})$$

$$+\int_{S_o}\tilde{t}_P(\mathbf{y})\int_S G_{mJ}^P(\boldsymbol{\xi}-\mathbf{y})D_m\upsilon_J(\boldsymbol{\xi})dS(\boldsymbol{\xi})dS(\mathbf{y}) \qquad . \qquad (2.20)$$

$$-\int_{S_o}\tilde{t}_P(\mathbf{y})\int_S H_{iJ}^P(\boldsymbol{\xi}-\mathbf{y})n_i(\boldsymbol{\xi})\upsilon_J(\boldsymbol{\xi})dS(\boldsymbol{\xi})dS(\mathbf{y})$$

where the constant $c(\mathbf{y})$ simply reduces to 1/2 due to that the ordinary boundary of the body is piecewise smooth; a set of points $\mathbf{y}$ where the unit normal $\mathbf{n}$ is not well-defined is of measure zero. It is worth noting that the integral equation (2.20) contain only weakly singular kernels $\{U_J^P,\ G_{mJ}^P,\ H_{iJ}^P n_i\}$ of $\mathcal{O}(1/r)$. Verification of the weakly singular nature of the product $H_{iJ}^P n_i$ can be found in the work of Xiao (1998).

2.3.2 Weakly singular integral equation for generalized surface traction

To obtain a weakly singular, weak-form boundary integral equation for the generalized surface traction, it can be proceeded as follows. First, the special decomposition (2.11) and (2.12) are substituted into the boundary integral relation (2.9) and the result is then integrated by part via Stokes' theorem. The final singularity-reduced boundary integral relation for the generalized stress takes the form

$$\sigma_{iK}(\mathbf{x}) = \varepsilon_{irt}\frac{\partial}{\partial x_r}\left[\int_S C_{mJ}^{tK}(\boldsymbol{\xi}-\mathbf{x})D_m\upsilon_J(\boldsymbol{\xi})dS(\boldsymbol{\xi}) + \int_{S_o} G_{tK}^J(\boldsymbol{\xi}-\mathbf{x})t_J(\boldsymbol{\xi})dS(\boldsymbol{\xi})\right]$$
$$-\int_{S_o} H_{iK}^J(\boldsymbol{\xi}-\mathbf{x})t_J(\boldsymbol{\xi})dS(\boldsymbol{\xi}) \qquad (2.21)$$

where the translational property of the kernels G_{mJ}^P and C_{mJ}^{tK}, i.e. $\partial G_{tK}^J(\boldsymbol{\xi}-\mathbf{x})/\partial\xi_r = -\partial G_{tK}^J(\boldsymbol{\xi}-\mathbf{x})/\partial x_r$ and $\partial C_{mJ}^{tK}(\boldsymbol{\xi}-\mathbf{x})/\partial\xi_r = -\partial C_{mJ}^{tK}(\boldsymbol{\xi}-\mathbf{x})/\partial x_r$, has been employed. Next, by forming the product $n_l(\mathbf{y})\sigma_{lK}(\mathbf{x})$ where $\mathbf{y}\in S$ and then taking a limit $\mathbf{x}\to\mathbf{y}$, a boundary integral equation for the generalized surface traction is obtained as

$$\rho(\mathbf{y})t_K^*(\mathbf{y}) = D_t \int_S C_{mJ}^{tK}(\boldsymbol{\xi}-\mathbf{y})D_m\upsilon_J(\boldsymbol{\xi})dS(\boldsymbol{\xi}) + D_t \int_{S_o} G_{tK}^{J}(\boldsymbol{\xi}-\mathbf{y})t_J(\boldsymbol{\xi})dS(\boldsymbol{\xi})$$

$$- \int_{S_o} n_l(\mathbf{y})H_{lK}^{J}(\boldsymbol{\xi}-\mathbf{y})t_J(\boldsymbol{\xi})dS(\boldsymbol{\xi}) \tag{2.22}$$

where $\rho(\mathbf{y})=1/2$ if the surface is sufficiently smooth at $\mathbf{y}$ otherwise $\rho(\mathbf{y}) \in (0,1)$ and $t_K^*(\mathbf{y})$ is given by

$$t_K^*(\mathbf{y}) = \begin{cases} t_K(\mathbf{y}); & \mathbf{y} \in S_o \\ 2t_K^+; & \mathbf{y} \in S_c^+ \end{cases}. \tag{2.23}$$

Upon multiplying (2.22) by a test function

$$\tilde{\upsilon}_K(\mathbf{y}) = \begin{cases} \tilde{u}_K(\mathbf{y}), & \mathbf{y} \in S_o \\ \Delta\tilde{u}_K(\mathbf{y}), & \mathbf{y} \in S_c^+ \end{cases}, \tag{2.24}$$

integrating the result over the total boundary S, and then performing an integration by parts via Stoke's theorem, a weakly singular, weak-form integral equation for the generalized surface traction is obtained as

$$-\frac{1}{2}\int_S \tilde{\upsilon}_K(\mathbf{y})t_K^*(\mathbf{y})dS(\mathbf{y}) = \int_S D_t\tilde{\upsilon}_K(\mathbf{y})\int_S C_{mJ}^{tK}(\boldsymbol{\xi}-\mathbf{y})D_m\upsilon_J(\boldsymbol{\xi})dS(\boldsymbol{\xi})dS(\mathbf{y})$$

$$+ \int_S D_t\tilde{\upsilon}_K(\mathbf{y})\int_{S_o} G_{tK}^{J}(\boldsymbol{\xi}-\mathbf{y})t_J(\boldsymbol{\xi})dS(\boldsymbol{\xi})dS(\mathbf{y}) \tag{2.25}$$

$$+ \int_S \tilde{\upsilon}_K(\mathbf{y})\int_{S_o} H_{iK}^{J}(\boldsymbol{\xi}-\mathbf{y})n_i(\mathbf{y})t_J(\boldsymbol{\xi})dS(\boldsymbol{\xi})dS(\mathbf{y})$$

Again, the fact that the total boundary of the domain is piecewise smooth has been utilized to reduce the constant $\rho(\mathbf{y})$ to 1/2. It can also be noted that the integral equation (2.25) contains only weakly singular kernels $\{ C_{mJ}^{tK}, G_{tK}^{J}, H_{iK}^{J}n_i \}$ of $\mathcal{O}(1/r)$.

2.4 Symmetric Formulation

A system of governing integral equations for the piezoelectric finite body containing crack is obtained as follows: (i) applying the weakly singular, weak-form integral equations for the generalized displacement (2.20) to the surface S_u with $\widetilde{t}_P = 0$ on S_t; (ii) applying the weakly singular, weak-form integral equation for the generalized surface traction (2.25) to the surface S_t with $\widetilde{\upsilon}_P = 0$ on $S_u \cup S_c^+$ and, finally applying the weakly singular, weak-form integral equation for the generalized surface traction (2.25) to the crack surface S_c^+ with $\widetilde{\upsilon}_P = 0$ on $S_u \cup S_t$. The resulting set of governing integral equations is given by

$$\mathcal{A}_{uu}\left(\tilde{\mathbf{t}}, \mathbf{t}\right) + \mathcal{B}_{ut}\left(\tilde{\mathbf{t}}, \mathbf{u}\right) + \mathcal{B}_{uc}\left(\tilde{\mathbf{t}}, \Delta\mathbf{u}\right) = \mathcal{R}_1\left(\tilde{\mathbf{t}}\right)$$

$$\mathcal{B}_{ut}\left(\mathbf{t}, \tilde{\mathbf{u}}\right) + \mathcal{C}_{tt}\left(\tilde{\mathbf{u}}, \mathbf{u}\right) + \mathcal{C}_{tc}\left(\tilde{\mathbf{u}}, \Delta\mathbf{u}\right) = \mathcal{R}_2\left(\tilde{\mathbf{u}}\right) \qquad (2.26)$$

$$\mathcal{B}_{uc}\left(\mathbf{t}, \Delta\tilde{\mathbf{u}}\right) + \mathcal{C}_{ct}\left(\Delta\tilde{\mathbf{u}}, \mathbf{u}\right) + \mathcal{C}_{cc}\left(\Delta\tilde{\mathbf{u}}, \Delta\mathbf{u}\right) = \mathcal{R}_3\left(\Delta\tilde{\mathbf{u}}\right)$$

where the bi-linear integral operators $\mathcal{A}_{PQ}$, $\mathcal{B}_{PQ}$ and $\mathcal{C}_{PQ}$ (with $P, Q \in \{u, t, c\}$) are defined by

$$\mathcal{A}_{PQ}\left(\mathbf{X}, \mathbf{Y}\right) = \int_{S_P} X_K(\mathbf{y}) \int_{S_Q} U_J^K(\xi - \mathbf{y}) Y_J(\xi) dS(\xi) dS(\mathbf{y}) \qquad (2.27)$$

$$\mathcal{B}_{PQ}\left(\mathbf{X}, \mathbf{Y}\right) = \int_{S_P} X_K(\mathbf{y}) \int_{S_Q} G_{mJ}^K(\xi - \mathbf{y}) D_m Y_J(\xi) dS(\xi) dS(\mathbf{y})$$
$$\qquad\qquad - \int_{S_P} X_K(\mathbf{y}) \int_{S_Q} H_{iJ}^K(\xi - \mathbf{y}) n_i(\xi) Y_J(\xi) dS(\xi) dS(\mathbf{y}) \qquad (2.28)$$

$$\mathcal{C}_{PQ}\left(\mathbf{X}, \mathbf{Y}\right) = \int_{S_P} D_t X_K(\mathbf{y}) \int_{S_Q} C_{mJ}^{tK}(\xi - \mathbf{y}) D_m Y_J(\xi) dS(\xi) dS(\mathbf{y}) \qquad (2.29)$$

and the linear integral operators $\mathcal{R}_1$, $\mathcal{R}_2$ and $\mathcal{R}_3$ are defined, in terms of the prescribed data on the boundary, by

$$\mathcal{R}_1\left(\tilde{\mathbf{t}}\right) = \mathcal{F}_u\left(\tilde{\mathbf{t}}, \mathbf{u}_o\right) - \mathcal{A}_{ut}\left(\tilde{\mathbf{t}}, \mathbf{t}_o\right) - \mathcal{B}_{uu}\left(\tilde{\mathbf{t}}, \mathbf{u}_o\right) \qquad (2.30)$$

$$\mathcal{R}_2\left(\tilde{\mathbf{u}}\right) = -\mathcal{F}_t\left(\tilde{\mathbf{u}}, \mathbf{t}_o\right) - \mathcal{B}_{tt}\left(\mathbf{t}_o, \tilde{\mathbf{u}}\right) - \mathcal{C}_{tu}\left(\tilde{\mathbf{u}}, \mathbf{u}_o\right) \qquad (2.31)$$

$$\mathcal{R}_3\left(\Delta\tilde{\mathbf{u}}\right) = -2\mathcal{F}_c\left(\Delta\tilde{\mathbf{u}}, \mathbf{t}_c\right) - \mathcal{B}_{tc}\left(\mathbf{t}_o, \Delta\tilde{\mathbf{u}}\right) - \mathcal{C}_{cu}\left(\Delta\tilde{\mathbf{u}}, \mathbf{u}_o\right) \qquad (2.32)$$

with

$$\mathcal{F}_p\left(\mathbf{X}, \mathbf{Y}\right) = \frac{1}{2}\int_{S_p} X_I(\mathbf{y})Y_I(\mathbf{y})dS(\mathbf{y}) \qquad (2.33)$$

It is evident that the governing integral equations (2.26) are in a symmetric form, i.e. $\mathcal{A}_{uu}\left(\mathbf{X}, \mathbf{Y}\right) = \mathcal{A}_{uu}\left(\mathbf{Y}, \mathbf{X}\right)$ and $\mathcal{C}_{tt}\left(\mathbf{X}, \mathbf{Y}\right) = \mathcal{C}_{tt}\left(\mathbf{Y}, \mathbf{X}\right)$.

Even though the above formulation is originally developed for the piezoelectric finite domain, such formulation can be employed to solve the isolated crack embedded in a piezoelectric infinite domain by setting $S_o = \emptyset$ and the final form is given by

$$\mathcal{C}_{cc}\left(\Delta\tilde{\mathbf{u}}, \Delta\mathbf{u}\right) = -2\mathcal{F}_c\left(\Delta\tilde{\mathbf{u}}, \mathbf{t}_c\right) \qquad (2.34)$$

It should be emphasized that the equation (2.34) is applicable to an isolated crack embedded in a piezoelectric infinite domain which is free of the electro-elastic loading at infinity and such situation can be obtained by using the principle of superposition, which will be discussed in the following section.

2.5 Treatment of Remote Conditions

Consider a crack of arbitrary shape embedded in a piezoelectric infinite medium that is subjected to the remote mechanical and electrical loading as shown in Fig. 2.2(a). This original problem can be decomposed into two sub-problems by using the superposition method: (a) a homogenous piezoelectric infinite body containing no crack and subjected to the prescribed remote electromechanical loading and (b) a piezoelectric infinite body containing crack and subjected to an appropriate loading at the crack surface as shown in Figs 2.2(b) and 2.2(c), respectively.

Fig. 2.2. Decomposition of a crack in an infinite domain subjected to the loading at infinity: (a) original problem, (b) a piezoelectric infinite body containing no crack and subjected to the remote loading, and (c) a piezoelectric infinite body containing crack and subjected to the appropriate loading at the crack surface.

From the method of superposition, it leads to

$$t_J = t_J^\infty + t_J^*$$
(2.35)

$$\Delta u_J = \Delta u_J^\infty + \Delta u_J^*$$
(2.36)

where t_J and Δu_J are the generalized traction and the jump of the generalized displacement associated with the original problem (a); t_J^∞ and Δu_J^∞ are the generalized traction and the jump of the generalized displacement due to the remote loading associated with the problem (b); and t_J^* and Δu_J^* are the appropriate generalized traction and the jump of the generalized displacement due to the appropriate loading associated with the problem (c).

For the impermeable assumption, the mechanical traction t_j and surface electric charge t_4 are prescribed. By substituting $t_J = t_J^o$ and $t_J^\infty = \sigma_{iJ}^\infty n_i$ into the equation (2.35), the generalized traction t_J^* for the impermeable crack is obtained as

$$t_J^* = t_J^o - \sigma_{iJ}^\infty n_i$$
(2.37)

For the permeable assumption, the mechanical tractions t_j are prescribed whereas the jump of the electric potential Δu_4 are equal to zero. By substituting $t_j = t_j^o$ and $t_j^\infty = \sigma_{ij}^\infty n_i$ into the equation (2.35) and substituting $\Delta u_4 = 0$ and $\Delta u_4^\infty = 0$ into the equation (2.36), the mechanical traction t_j^* and the jump of the electric potential Δu_4^* for the permeable crack are obtained as

$$t_j^* = t_j^o - \sigma_{ij}^\infty n_i \tag{2.38}$$

$$\Delta u_4^* = 0 \tag{2.39}$$

For the semi-permeable assumption, the mechanical traction t_j are prescribed whereas the jump of the generalized displacement Δu_J and the surface electric charge t_4 are unknown a priori and satisfy the condition $t_4 \Delta u_j n_j = \kappa_c \Delta u_4$. By substituting $t_j = t_j^o$, $t_j^\infty = \sigma_{ij}^\infty n_i$, $t_4^\infty = D_i^\infty n_i$ and $t_4 = \kappa_c \Delta u_4 / \Delta u_j n_j$ into the equation (2.35), the mechanical traction t_j^* and the jump of the electric potential Δu_4 for this particular case are given by

$$t_j^* = t_j^o - \sigma_{ij}^\infty n_i \tag{2.40}$$

$$\Delta u_4 = \frac{\left(t_4^* + D_i^\infty n_i\right)\Delta u_j n_j}{\kappa_c} \tag{2.41a}$$

For convenience in the further development, the alternative expression of equation (2.41a) is given by

$$\Delta u_4 = \frac{(T_4^{\text{crack}} + T_4^\infty)\Delta u_j n_j}{\kappa_c} \tag{2.41b}$$

where $T_4^{\text{crack}} = t_4^*$ represents the surface electric charge and $T_4^\infty = D_i^\infty n_i$ represent the applied remote surface electric charge.

For the Landis-type assumption, the condition $t_4 \Delta u_j n_j = \kappa_c \Delta u_4$ is still the same as that for the semi-permeable crack, whereas the normal component of the stress σ_{nn} satisfies the condition $\sigma_{nn} = (1/2)\kappa_c (\Delta u_4 / \Delta u_m n_m)^2$ and the tangential components of the stress $\sigma^{shear,o}$ are prescribed. By substituting the conditions $t_4 \Delta u_j n_j = \kappa_c \Delta u_4$ and $t_4^\infty = D_i^\infty n_i$ into the equation (2.35), the jump of the electric potential (Δu_4) for the Landis-type cracks are given by

$$\Delta u_4 = \frac{\left(t_4^* + D_i^\infty n_i \right) \Delta u_j n_j}{\kappa_c} \tag{2.42}$$

And by substituting $t_j = \sigma_{nn} n_j + \sigma^{shear,o} s_j$ and $t_j^\infty = \sigma_{ij}^\infty n_i$ into the equation (2.35), it leads to

$$\sigma_{nn} n_j + \sigma^{shear,o} s_j = \sigma_{ij}^\infty n_i + t_j^* \tag{2.43}$$

And by substituting the condition $\sigma_{nn} = (1/2)\kappa_c (\Delta u_4 / \Delta u_m n_m)^2$ into equation (2.43), it yields

$$\frac{1}{2}\kappa_c \left(\frac{\Delta u_4}{\Delta u_m n_m} \right)^2 n_j + \sigma^{shear,o} s_j = \sigma_{ij}^\infty n_i + t_j^* \tag{2.44}$$

By using the equation (2.42) along with (2.44), the relation between the mechanical tractions $\sigma_{ij}^\infty n_i + t_j^*$, the surface electric charge $t_4^* + D_i^\infty n_i$ and the shear components of the mechanical tractions $\sigma^{shear,o} s_j$ are given by

$$t_j^* + \sigma_{ij}^\infty n_i = \frac{\left(t_4^* + D_i^\infty n_i \right)^2}{2\kappa_c} n_j + \sigma^{shear,o} s_j \tag{2.45a}$$

Again, for convenience in the further development, the alternative expression of equation (2.45a) is given by

$$T_j^{crack} + T_j^\infty = \frac{\left(T_4^{crack} + T_4^\infty\right)^2}{2\kappa_c} n_j + T_j^{shear} \qquad (2.45b)$$

where $T_j^{crack} = t_j^*$ represents the mechanical tractions, $T_j^\infty = \sigma_{ij}^\infty n_i$ represents the applied remote mechanical tractions, $T_4^{crack} = t_4^*$ represents the surface electric charge, $T_4^\infty = D_i^\infty n_i$ represents the applied remote surface electric charge and $T_j^{shear} = \sigma^{shear,o} s_j$ represents the shear components of the mechanical tractions.

CHAPTER III

NUMERICAL IMPLEMENTATIONS

A set of symmetric weak-form boundary integral equations (2.26), established in the previous chapter, constitutes a basis for the development of a weakly singular symmetric Galerkin boundary element method (SGBEM). This chapter briefly summarizes components essential for implementing such well-known numerical technique, e.g. discretization, numerical integration of double surface integrals, evaluation of weakly singular kernels, solver for boundary conditions, and determination of stress and electric intensity factors.

3.1 Discretization

A standard Galerkin approximation scheme is used to discretize the governing integral equations (2.26). Because such integral equations contain only weakly singular kernels of order $\mathcal{O}(1/r)$, standard C^o-interpolations are employed to approximate the solution and test functions on both the ordinary boundary ($S_o = S_u \cup S_t$) and the majority of the crack surface S_c^+. The special C^o-interpolations are employed to approximate the jump of the generalized displacement on the local region near the crack front. Those special crack tip elements, which were proposed by Rungamornrat and Mear (2008c), have two attractive features: (i) the shaped function of these elements can capture the higher order approximation of asymptotic field (capture the first three terms) and (ii) the degrees of freedoms of nodes along the fracture front are directly related to the stress and electric intensity factors. It should be emphasized that the first feature allows relatively large crack-tip elements to be used along the crack front and the second feature provides a direct means to determine the mixed-mode stress intensity factors and the electric intensity factor without carrying extrapolations.

Another task that requires a special care is associated with the treatment of surface-breaking cracks; for this particular case, the crack surface is not embedded entirely within the domain but intersects its ordinary boundary as shown schematically in Fig.3.1(a). In the discretization, shape functions defined on certain elements on the ordinary boundary that contain the vertex (a point where the crack front intersects the ordinary boundary) and are adjacent to the crack-tip element (e.g. elements A and B shown in Fig.3.1(b)) must be modified to ensure the continuity across the element inter-boundary and the ability to represent constant and linear functions. Such modification can be achieved by employing special shape functions analogous to those proposed by Li *et al.* (1998).
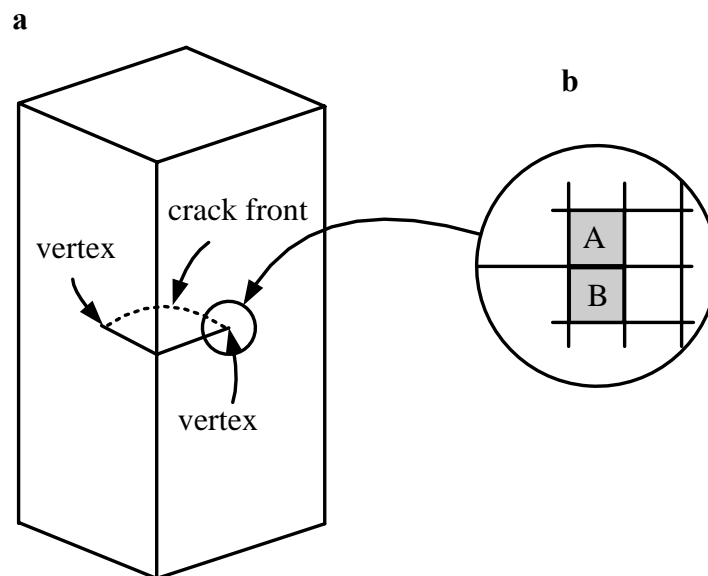
Fig. 3.1. (a) Schematic of a body containing a surface-breaking crack and (b) schematic of mesh in a local region surrounding the vertex. Element A and B are adjacent to the crack-tip elements.

By using the symmetric system of governing integral equations (2.26), along with the discretization via Galerkin approximation, leads to a system of linear algebraic equations for a piezoelectric finite domain containing crack is given by

$$\begin{bmatrix} \mathbf{A}_{uu} & \mathbf{B}_{ut} & \mathbf{B}_{uc} \\ \mathbf{B}_{ut}^T & \mathbf{C}_{tt} & \mathbf{C}_{tc} \\ \mathbf{B}_{uc}^T & \mathbf{C}_{tc}^T & \mathbf{C}_{cc} \end{bmatrix} \begin{bmatrix} \mathbf{T}_B \\ \mathbf{U}_B \\ \mathbf{\Delta U} \end{bmatrix} = \begin{bmatrix} \mathbf{R}_1 \\ \mathbf{R}_2 \\ \mathbf{R}_3 \end{bmatrix} \tag{3.1}$$

where $\mathbf{A}_{PQ}$, $\mathbf{B}_{PQ}$ and $\mathbf{C}_{PQ}$ (with $P, Q \in \{u,t,c\}$) correspond to the integral operators $\mathcal{A}_{PQ}$, $\mathcal{B}_{PQ}$ and $\mathcal{C}_{PQ}$, and where the column vectors $\mathbf{R}_1$, $\mathbf{R}_2$ and $\mathbf{R}_3$ correspond to the integral operators $\mathcal{R}_1$, $\mathcal{R}_2$ and $\mathcal{R}_3$.

And by using the formulation (2.25) along with the discretization via Galerkin approximation, a system of linear algebraic equations for an isolated crack embedded in an infinite domain is given by

$$\mathbf{C\Delta U} + \mathbf{LT} = \mathbf{0} \tag{3.2}$$

where matrices $\mathbf{C}$ corresponds to double surface integrals, which involves the kernel C_{mJ}^{tK} that is weakly singular of order 1/r; matrix $\mathbf{L}$ corresponds to a single surface integral; $\mathbf{\Delta U}$ is a vector of nodal quantities associated with the jump of the generalized displacement (i.e. the jump of mechanical displacement $\begin{bmatrix} \Delta \mathbf{U}_1 & \Delta \mathbf{U}_2 & \Delta \mathbf{U}_3 \end{bmatrix}^T$ and the jump of the electric potential $\Delta \mathbf{U}_4$), and $\mathbf{T}$ is a vector of nodal quantities of the generalized traction, respectively.

The system of linear algebraic equation (3.1), which is developed for analyzing a cracked piezoelectric finite body, and the equation (3.2), which is established to solve an isolated crack embedded in an unbounded domain, are sufficient to solve all unknowns for the impermeable and permeable cracks. However, the semi-permeable and Landis-type cracks require additional equations due to extra unknowns present on the crack surface. For semi-permeable cracks, by applying the weight residual technique along with the equation (2.41b), $\Delta u_4 = (T_4^{\text{crack}} + T_4^{\infty}) \Delta u_m n_m / \kappa_c$, on the entire crack surface. The resulting weak-from is given by

$$\int_{S_c^+} \psi^{(i)} \varphi^{(k)} dS_c^+ \Delta u_4^{(k)} = \frac{\int_{S_c^+} \psi^{(i)} \phi^{(j)} \Delta u_m^{(k)} n_m \varphi^{(k)} dS_c^+ \left[T_4^{\text{crack}(j)} + T_4^{\infty(j)} \right]}{\kappa_c} \qquad (3.3)$$

where $\Delta u_4^{(k)}$ and $\Delta u_m^{(k)}$ are, respectively, the jump of the electric potential and the jump of the mechanical displacement associated with the node k, n_m is the outward unit normal vector on the crack surface, ψ_i is the basis function associated with the node i, $T_4^{\text{crack}(j)}$ and $T_4^{\infty(j)}$ are, respectively, the surface electric charge on the crack surface and the applied remote surface electric charge associated with the node j, $\phi^{(j)}$ is the basis function of these quantities $\left\{ T_4^{\text{crack}(j)} \quad T_4^{\infty(j)} \right\}$ associated with the node j, and $\varphi^{(k)}$ is the basis function of these quantities $\left\{ \Delta u_4^{(k)} \quad \Delta u_m^{(k)} \right\}$ associated with the node k. It should be noted that the shape functions of $\left\{ \Delta u_4^{(k)} \quad \Delta u_m^{(k)} \right\}$ are the special C^o-interpolation functions for the elements located near the crack front and are the standard C^o-interpolation functions for the regular elements located the rest of the crack surface. The alternative expression of the equation (3.3) can be written into matrix form as follows

$$\mathbf{A} \Delta \mathbf{U}_4 = \mathbf{N}(\Delta \mathbf{U}_1, \Delta \mathbf{U}_2, \Delta \mathbf{U}_3) \mathbf{T}_4 \qquad (3.4)$$

where $\left[\mathbf{N} \right]_{ij} = (1/\kappa_c) \int_{S_c^+} \psi^{(i)} \phi^{(j)} \Delta u_m^{(k)} n_m \varphi^{(k)} dS_c^+$, $\left[\mathbf{A} \right]_{ik} = \int_{S_c^+} \psi^{(i)} \varphi^{(k)} dS_c^+$, $\left[\Delta \mathbf{U}_4 \right]_k = \Delta u_4^{(k)}$ and $\left[\mathbf{T}_4 \right]_j = \left[T_4^{\text{crack}(j)} + T_4^{\infty(j)} \right]$. It is seen that the unknown vectors $\Delta \mathbf{U}_4$, $\left[\Delta \mathbf{U}_1 \quad \Delta \mathbf{U}_2 \quad \Delta \mathbf{U}_3 \right]^T$ and $\mathbf{T}_4$ are coupled together. More specially, the jump of the electric potential $\Delta \mathbf{U}_4$ is related to the jump of mechanical displacement $\left[\Delta \mathbf{U}_1 \quad \Delta \mathbf{U}_2 \quad \Delta \mathbf{U}_3 \right]^T$ and the surface electric charge $\mathbf{T}_4$ via the equation (3.4). Finally, the system of linear algebraic equation (3.1), which is developed for piezoelectric finite domain, and equation (3.2), which is established for an unbounded domain, along with the equation (3.4) is sufficiently to solve the unknown vectors by using the Newton-Raphson iterative scheme.

For Landis-type cracks, two additional equations are required; the first one is the same as that one for the semi-permeable cracks and the final form is given as shown in equation (3.4). And another one is obtained by applying the weight residual technique along with the equation (2.45b), the final weak-form is given by

$$\int_{S_c^+} \psi^{(i)} \phi^{(j)} dS_c^+ \left[T_m^{crack(j)} + T_m^{\infty(j)} - T_m^{shear(j)} \right] = \frac{\int_{S_c^+} \psi^{(i)} \left[T_4^{\infty(j)} \phi^{(j)} + T_4^{crack(j)} \phi^{(j)} \right]^2 n_m dS_c^+}{2\kappa_c} \quad (3.5)$$

where $T_m^{crack(j)}$ and $T_m^{\infty(j)}$ are, respectively, the mechanical tractions on the crack surface and the applied remote mechanical tractions associated with the node j, $\psi^{(i)}$ is the basis function associated with the node i, n_m is the outward unit normal vector on the crack surface and $\phi^{(j)}$ is the basis function of these quantities $\left\{ T_m^{crack(j)} \quad T_m^{\infty(j)} \quad T_4^{crack(j)} \quad T_4^{\infty(j)} \quad T_m^{shear(j)} \right\}$ associated with node j. The equation (3.5) can be also written in matrix form as

$$\begin{bmatrix} \mathbf{A} & \mathbf{0} & \mathbf{0} \\ \mathbf{0} & \mathbf{A} & \mathbf{0} \\ \mathbf{0} & \mathbf{0} & \mathbf{A} \end{bmatrix} \begin{bmatrix} \mathbf{T}_1 \\ \mathbf{T}_2 \\ \mathbf{T}_3 \end{bmatrix} = \begin{bmatrix} \mathbf{M}_1(\mathbf{T}_4) \\ \mathbf{M}_2(\mathbf{T}_4) \\ \mathbf{M}_3(\mathbf{T}_4) \end{bmatrix} - \begin{bmatrix} \mathbf{T}_1^{known} \\ \mathbf{T}_2^{known} \\ \mathbf{T}_3^{known} \end{bmatrix} \quad (3.6)$$

where $\left[\mathbf{M}_m \right]_i = \dfrac{1}{2\kappa_c} \displaystyle\int_{S_c^+} \psi^{(i)} \left[T_4^{\infty(j)} \phi^{(j)} + T_4^{crack(j)} \phi^{(j)} \right]^2 n_m dS_c^+$, $\left[\mathbf{A} \right]_{ij} = \displaystyle\int_{S_c^+} \psi^{(i)} \phi^{(j)} dS_c^+$,

$\left[\mathbf{T}_m \right]_j = \left[T_m^{crack(j)} \right]$ and $\left[\mathbf{T}_m^{known} \right]_i = \displaystyle\int_{S_c^+} \psi^{(i)} \phi^{(j)} dS_c^+ \left[T_m^{\infty(j)} - T_m^{shear(j)} \right]$. It is seen that the

unknown vectors $\begin{bmatrix} \mathbf{T}_1 & \mathbf{T}_2 & \mathbf{T}_3 \end{bmatrix}^T$ and $\mathbf{T}_4$ are coupled together. More specially, the mechanical tractions $\begin{bmatrix} \mathbf{T}_1 & \mathbf{T}_2 & \mathbf{T}_3 \end{bmatrix}^T$ are related to the surface electric charge $\mathbf{T}_4$ via the equation (3.6). Finally, the system of linear algebraic equation (3.1) (or (3.2)), along with the equation (3.4) and (3.6), is sufficiently to solve the unknown vectors by using the Newton-Raphson iterative scheme. And this will be discussed in the section 3.4.

3.2 Numerical Integration

As be evident from (2.26), the governing equations involve two groups of integrals: single surface integrals and double surface integrals. The integrand of integrals in the first group involves the test functions and prescribed data and is, therefore, non-singular. Numerical evaluation of such integrals can efficiently and accurately be performed by standard Gaussian quadrature. In contrast, integrals in the second group consume more computational cost due to that they involves double surface integration and their integrand contains kernels that may generate singularity or rapid variation behavior within the surface of integration. In general, integrals in this group can further be classified into three different types: regular integrals, weakly-singular integrals and nearly singular integrals.

The regular double surface integral is associated with an integral over a pair of elements (resulting from the discretization) that are relatively remote (in comparison with their characteristic dimension such as the size of elements). For this particular case, the integrand is non-singular and exhibits only mild variation across the surface of integration. Hence, such regular integrals can accurately and efficiently be integrated by standard Gaussian quadrature.

The weakly singular double surface integral arises when it involves a pair of coincident elements. The integrand of this particular integral is therefore singular of $\mathcal{O}(1/r)$. While in principle this weakly singular integral exists in an ordinary sense, its numerical evaluation still requires special care. It has been pointed out by Xiao (1998) that this type of integrals can no longer be integrated efficiently by standard Gaussian quadrature; a substantially large number of integration points is required to achieve a reasonable level of accuracy. To circumvent such situation, a triangular polar transformation is first employed to remove $1/r$ singularity and then a special family of logarithmic transformations is applied to further alleviate the rapid variation of the integrand that may be generated by the former transformation. The resulting integrand is well-behaved and can accurately be integrated by standard Gaussian quadrature with a reasonable number of integration points (also see details form Hayami and Brebbia, 1988; Li and Han, 1985; Xiao, 1998).

The nearly singular double surface integral arises when elements in the pair are not coincident but adjacent or relatively close in comparison with their characteristic dimensions. The integrand of this integral is generally non-singular (except along the adjacent edge of the two elements) but can exhibit rapid variation in the zone that the source and field points are nearly coincident. It has also been found by Xiao (1998) that the nearly singular integral of this type cannot efficiently be integrated by standard Gaussian quadrature without modification. To overcome this difficulty, the triangular polar transformation is first applied and the result is further regularized by a series of logarithmic transformations in both radial and angular directions (resulting from the triangular polar transformation). The resulting new integrand possesses only mild variation and the corresponding integral can accurately and efficiently be integrated by standard Gaussian quadrature (also see details from Hayami, 1992; Hayami and Matsumoto, 1994; Xiao, 1998).

3.3 Evaluation of Kernels

Another essential component that must be incorporated in order to reduce the computational cost of numerical evaluation of double surface integrals is the efficient evaluation of the five weakly singular kernels $\{ U_J^P(\mathbf{y} - \mathbf{x}), \ G_{mJ}^P(\mathbf{y} - \mathbf{x}), \ C_{mJ}^{tK}(\mathbf{y} - \mathbf{x}),$ $H_{iK}^J(\mathbf{y} - \mathbf{x})n_i(\mathbf{x}), \ H_{iK}^J(\mathbf{y} - \mathbf{x})n_i(\mathbf{y}) \}$ at every pair of points $\{\mathbf{x}, \ \mathbf{y}\}$ arising from the numerical integration. From the explicit expression (2.13) along with the standard procedure for computing a unit normal vector, the last two kernels can directly and efficiently be computed. In contrast, the first three kernels are given in terms of closed-loop integrals by (2.8) and (2.14)-(2.15); as a result, a direct evaluation of such integrals is obviously computationally expensive. To avoid such massive computation, we adopt an interpolation technique to approximate values of those kernels. In this technique, it requires evaluation of the closed-loop integrals only at nodal points of the interpolation grid and values of kernels at arbitrary pair of points $\{\mathbf{x}, \ \mathbf{y}\}$ can readily be approximated by interpolants of the kernels constructed based on piecewise polynomial basis functions on the interpolation grid. Accuracy of this approximation can readily be enhanced by either increasing the number of nodal points or increasing the highest degree of the polynomial basis functions. Extensive

discussion of this interpolation technique can be found in the work of Rungamornrat and Mear (2008b, 2008c).

3.4 Solver for Different Electrical Boundary Conditions

For impermeable cracks, the system of linear equations (3.1) and (3.2) developed to treat the piezoelectric finite and infinite bodies, respectively, have the same number of equations as the number of unknowns. As a result, the unknown vector $\begin{bmatrix} \mathbf{T}_B & \mathbf{U}_B & \mathbf{\Delta U} \end{bmatrix}^T$, which is sought for the finite domain problem, and $\mathbf{\Delta U}$, for an unbounded domain case, can be obtained immediately by solving the system of equations (3.1) and (3.2), respectively.

For permeable cracks, again the system of linear equations (3.1) and (3.2) contain the same number of unknowns as the number of equations. Consequently, the unknown vectors $\begin{bmatrix} \mathbf{T}_B & \mathbf{U}_B & \mathbf{\Delta U}_1 & \mathbf{\Delta U}_2 & \mathbf{\Delta U}_3 \end{bmatrix}^T$ and $\mathbf{T}_4$, which are sought for the finite domain problem, and $\begin{bmatrix} \mathbf{\Delta U}_1 & \mathbf{\Delta U}_2 & \mathbf{\Delta U}_3 \end{bmatrix}^T$ and $\mathbf{T}_4$, which are sought for the infinite domain problem, can be obtained immediately by solving the system of equations (3.1) and (3.2), respectively.

For semi-permeable cracks, the systems of linear equations (3.1) or (3.2) contain more unknowns than the number of equations. As a result, additional equations are required and given by the equation (3.4). Once the system of equations is sufficiently formulated, i.e. equation (3.1) or (3.2) along with the additional equation (3.4), an iterative method called the Newton-Raphson scheme is employed to solve for all unknowns. However, before presenting the procedure to solve the resulting system of nonlinear equations, some variables need to be introduced into the equation (3.1) and also some additional equations need to be defined to provide a better understanding of the algorithm.

Consider first the system of linear equations (3.1) for cracks in piezoelectric finite media.

$$\begin{bmatrix} \mathbf{A}_{uu} & \mathbf{B}_{ut} & \mathbf{B}_{uc} \\ \mathbf{B}_{ut}^T & \mathbf{C}_{tt} & \mathbf{C}_{tc} \\ \mathbf{B}_{uc}^T & \mathbf{C}_{tc}^T & \mathbf{C}_{cc} \end{bmatrix} \begin{bmatrix} \mathbf{T}_B \\ \mathbf{U}_B \\ \mathbf{\Delta U} \end{bmatrix} = \begin{bmatrix} \mathbf{R}_1 \\ \mathbf{R}_2 \\ \mathbf{R}_3 \end{bmatrix}$$

The right hand side vector $\mathbf{R}_3$ is decomposed into $\begin{bmatrix} \mathbf{R}_3^{Known} & \mathbf{ST} \end{bmatrix}$ where $\mathbf{R}_3^{Known}$ is a vector of nodal quantities of the prescribed data (e.g. generalized traction and generalized displacement) on the boundary whereas $\mathbf{ST}$ is a vector of nodal quantities of the data on the crack surface in which $\mathbf{S}$ is a matrix associated with a single surface integral and $\mathbf{T}$ is a vector of nodal quantities of the generalized traction at the crack surface. By substituting $\mathbf{R}_3 = \mathbf{R}_3^{Known} + \mathbf{ST}$ into the equation (3.1), it leads to

$$\begin{bmatrix} \mathbf{A}_{uu} & \mathbf{B}_{ut} & \mathbf{B}_{uc} \\ \mathbf{B}_{ut}^T & \mathbf{C}_{tt} & \mathbf{C}_{tc} \\ \mathbf{B}_{uc}^T & \mathbf{C}_{tc}^T & \mathbf{C}_{cc} \end{bmatrix} \begin{bmatrix} \mathbf{T}_B \\ \mathbf{U}_B \\ \boldsymbol{\Delta U} \end{bmatrix} = \begin{bmatrix} \mathbf{R}_1 \\ \mathbf{R}_2 \\ \mathbf{R}_3^{Known} \end{bmatrix} + \begin{bmatrix} \mathbf{0} \\ \mathbf{0} \\ \mathbf{ST} \end{bmatrix} \tag{3.7}$$

Or by using the index notation, equation (3.7) can be written as

$$\mathbf{K}_{ij} \mathbf{T}_j^* = \mathbf{R}_i^* \tag{3.8}$$

where $\mathbf{T}_j^* \in \{\mathbf{T}_B \quad \mathbf{U}_B \quad \boldsymbol{\Delta U}\}$ and $\mathbf{R}_i^* \in \{\mathbf{R}_1 \quad \mathbf{R}_2 \quad \mathbf{R}_3^{Known} + \mathbf{ST}\}$. To rearrange the equation (3.8) and then differentiate with respect to the unknown vectors ($\mathbf{X}_p$), this leads to

$$\mathbf{A}_{ip}^* = \mathbf{K}_{ij} \frac{\partial \mathbf{T}_j^*}{\partial \mathbf{X}_p} - \frac{\partial \mathbf{R}_i^*}{\partial \mathbf{X}_p} \tag{3.9}$$

where $\mathbf{A}_{ip}^*$ is the left-hand side coefficient matrix of the Newton-Raphson method and $\mathbf{X}_p \in \{\mathbf{T}_B \quad \mathbf{U}_B \quad \boldsymbol{\Delta U}_1 \quad \boldsymbol{\Delta U}_2 \quad \boldsymbol{\Delta U}_3 \quad \mathbf{T}_4\}$. The residual vector is given by

$$\mathbf{B}_i^* = (-1)\left(\mathbf{K}_{ij}\mathbf{T}_j^* - \mathbf{R}_i^*\right) \tag{3.10}$$

Once the gradient matrix $\mathbf{A}_{ip}^*$ and the residual vector $\mathbf{B}_i^*$ are obtained, the unknown vector $\mathbf{X}_p$ at the ($k+1$) iteration can be updated by solving a system of linear equations

$$\mathbf{A}_{ip}^{*(k)}(\mathbf{X}_p^{(k+1)} - \mathbf{X}_p^{(k)}) = \mathbf{B}_i^{*(k)} \tag{3.11}$$

where k is the iteration number. As a final remark, the terms $\partial \mathbf{T}_j^* / \partial \mathbf{X}_p$ and $\partial \mathbf{R}_i^* / \partial \mathbf{X}_p$, which are presented in equation (3.9), can be written in the matrix form as

$$\frac{\partial \mathbf{T}_j^*}{\partial \mathbf{X}_p} = \begin{bmatrix} \mathbf{1} & \mathbf{0} & \mathbf{0} \\ \mathbf{0} & \mathbf{1} & \mathbf{0} \\ \mathbf{0} & \mathbf{0} & \dfrac{\partial \Delta \mathbf{U}_j}{\partial \Delta \mathbf{U}_p^*} \end{bmatrix} \tag{3.12}$$

$$\frac{\partial \mathbf{R}_i^*}{\partial \mathbf{X}_p} = \begin{bmatrix} \mathbf{0} & \mathbf{0} & \mathbf{0} \\ \mathbf{0} & \mathbf{0} & \mathbf{0} \\ \mathbf{0} & \mathbf{0} & \mathbf{S}_{im}\dfrac{\partial \mathbf{T}_m}{\partial \Delta \mathbf{U}_p^*} \end{bmatrix} \tag{3.13}$$

where $\Delta \mathbf{U}_p^* = \{ \Delta \mathbf{U}_1 \quad \Delta \mathbf{U}_2 \quad \Delta \mathbf{U}_3 \quad \mathbf{T}_4 \}$. Similarly, the terms $\partial \Delta \mathbf{U}_j / \partial \Delta \mathbf{U}_p^*$ and $\partial \mathbf{T}_m / \partial \Delta \mathbf{U}_p^*$ can be written in the matrix form as

$$\frac{\partial \Delta \mathbf{U}_j}{\partial \Delta \mathbf{U}_p^*} = \begin{bmatrix} \mathbf{1} & \mathbf{0} & \mathbf{0} & \mathbf{0} \\ \mathbf{0} & \mathbf{1} & \mathbf{0} & \mathbf{0} \\ \mathbf{0} & \mathbf{0} & \mathbf{1} & \mathbf{0} \\ \dfrac{\partial \Delta \mathbf{U}_4}{\partial \Delta \mathbf{U}_1} & \dfrac{\partial \Delta \mathbf{U}_4}{\partial \Delta \mathbf{U}_2} & \dfrac{\partial \Delta \mathbf{U}_4}{\partial \Delta \mathbf{U}_3} & \dfrac{\partial \Delta \mathbf{U}_4}{\partial \mathbf{T}_4} \end{bmatrix} \tag{3.14}$$

$$\frac{\partial \mathbf{T}_m}{\partial \Delta \mathbf{U}_p^*} = \begin{bmatrix} \mathbf{0} & \mathbf{0} & \mathbf{0} & \mathbf{0} \\ \mathbf{0} & \mathbf{0} & \mathbf{0} & \mathbf{0} \\ \mathbf{0} & \mathbf{0} & \mathbf{0} & \mathbf{0} \\ \mathbf{0} & \mathbf{0} & \mathbf{0} & \mathbf{1} \end{bmatrix} \tag{3.15}$$

The procedure of Newton-Raphson iteration to obtain the unknown vectors can be summarized below (also see the flowchart in Fig.3.2).

(1) Initial guess $\mathbf{X}_p^{(k)} = \begin{bmatrix} \mathbf{T}_B^{(k)} & \mathbf{U}_B^{(k)} & \Delta \mathbf{U}_1^{(k)} & \Delta \mathbf{U}_2^{(k)} & \Delta \mathbf{U}_3^{(k)} & \mathbf{T}_4^{(k)} \end{bmatrix}^T$ with $k = 0$ by using the results obtained from the impermeable cracks

(2) Obtain $\Delta\mathbf{U}_4^{(k)}$ from equation (3.4)

(3) Compute $\dfrac{\partial \Delta U_j^{(k)}}{\partial \Delta U_P^*}$ and $S_{im}\dfrac{\partial T_m^{(k)}}{\partial \Delta U_p^*}$ where $\Delta\mathbf{U}_p^* = \left\{ \Delta\mathbf{U}_1 \quad \Delta\mathbf{U}_2 \quad \Delta\mathbf{U}_3 \quad \mathbf{T}_4 \right\}$

(4) Obtain $\dfrac{\partial T_j^{*(k)}}{\partial X_p}$ and $\dfrac{\partial R_i^{*(k)}}{\partial X_p}$ (Note that $\dfrac{\partial T_j^{*(k)}}{\partial X_p} = \dfrac{\partial \Delta U_j^{(k)}}{\partial \Delta U_P^*}$ and

$\dfrac{\partial R_i^{*(k)}}{\partial X_p} = S_{im}\dfrac{\partial T_m^{(k)}}{\partial \Delta U_p^*}$ for an unbounded domain problem)

(5) Compute $A_{ip}^{*(k)} = K_{ij}\dfrac{\partial T_j^{*(k)}}{\partial X_p} - \dfrac{\partial R_i^{*(k)}}{\partial X_p}$

(6) Compute $B_i^{*(k)} = (-1)(K_{ij}T_j^{*(k)} - R_i^{*(k)})$

(7) Obtain $X_p^{(k+1)}$ by solving the equation $A_{ip}^{*(k)}(X_p^{(k+1)} - X_p^{(k)}) = B_i^{*(k)}$

(8) Obtain $\Delta\mathbf{U}_4^{(k+1)}$ from equation (3.4)

(9) Obtain $T_j^{*(k+1)}$ and $R_i^{*(k+1)}$

(10) Three criteria are employed to check the convergence of the numerical solutions. The first one is the relative errors of $\left\| \Delta U_1^{(k+1)} - \Delta U_1^{(k)} \quad \Delta U_2^{(k+1)} - \Delta U_2^{(k)} \quad \Delta U_3^{(k+1)} - \Delta U_3^{(k)} \right\|_e / \left\| \Delta U_1^{(0)} \quad \Delta U_2^{(0)} \quad \Delta U_3^{(0)} \right\|_e$. The second one is the relative of $\left\| \mathbf{T}_4^{(k+1)} - \mathbf{T}_4^{(k)} \right\|_e / \left\| \mathbf{T}_4^{(0)} \right\|_e$ and the last one is the relative of $\left\| r^* \right\|_e / \left\| R^{*(0)} \right\|_e$, where $r_i^* = K_{ij}T_j^{*(k+1)} - R_i^{*(k+1)}$. The convergent solution ($T_j^{*(k+1)}$) is obtained when the all three criteria, which are defined above, are less than the specified tolerance (Tol). Otherwise, go to the next iteration by updating $k = k + 1$ and repeat step (2) to (10).
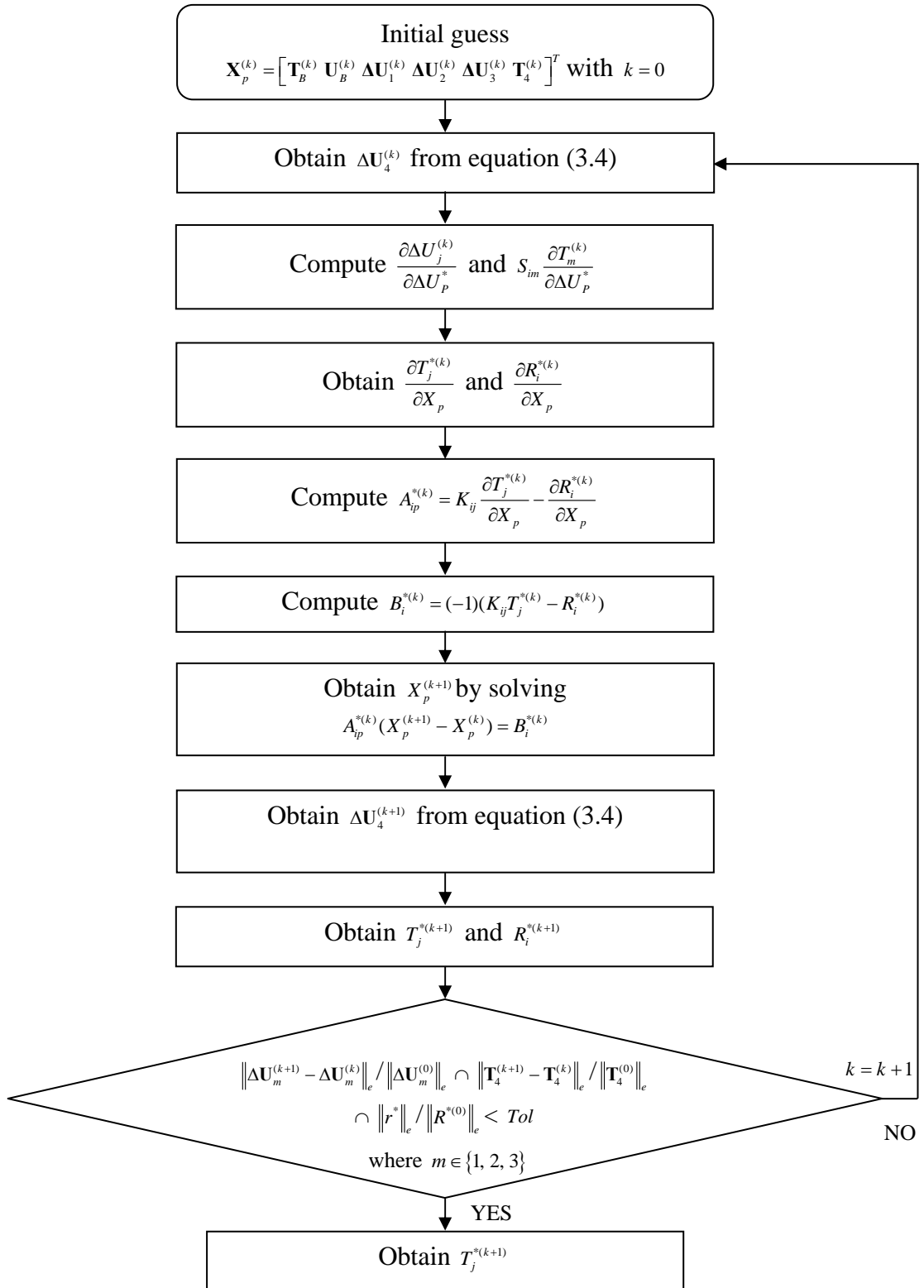
Fig. 3.2. Flowchart of solution procedures by Newton-Raphson method for the semi-permeable cracks.

For Landis-type cracks, the systems of linear equations (3.1) or (3.2) have the number of equations less than the number of unknowns. Consequently, two additional equations are required. The first one is given by equation (3.4), which is exactly the same as that for semi-permeable cracks, and another one is given by equation (3.6). The main difference between the Landis-type cracks and the semi-permeable cracks, besides the equation (3.6) is added to the system of equations of the Landis-type cracks, the term $\partial \mathbf{T}_m / \partial \Delta \mathbf{U}_p^*$ is different from the case of the semi-permeable cracks and is given in the matrix form as

$$\frac{\partial \mathbf{T}_m}{\partial \Delta \mathbf{U}_p^*} = \begin{bmatrix} 0 & 0 & 0 & \dfrac{\partial \mathbf{T}_1}{\partial \mathbf{T}_4} \\[2ex] 0 & 0 & 0 & \dfrac{\partial \mathbf{T}_2}{\partial \mathbf{T}_4} \\[2ex] 0 & 0 & 0 & \dfrac{\partial \mathbf{T}_3}{\partial \mathbf{T}_4} \\[2ex] 0 & 0 & 0 & 1 \end{bmatrix} \tag{3.16}$$

Once a set of all equations is formulated, the Newton-Raphson method is employed to solve all unknown vectors and the procedure is presented below (also see Fig 3.3.for the corresponding flowchart).

(1) Initial guess $\mathbf{X}_p^{(k)} = \begin{bmatrix} \mathbf{T}_B^{(k)} & \mathbf{U}_B^{(k)} & \Delta \mathbf{U}_1^{(k)} & \Delta \mathbf{U}_2^{(k)} & \Delta \mathbf{U}_3^{(k)} & \mathbf{T}_4^{(k)} \end{bmatrix}^T$ with $k = 0$ by using the results obtained from the impermeable cracks

(2) Obtain $\Delta \mathbf{U}_4^{(k)}$ from equation (3.4) and obtain $\begin{bmatrix} \mathbf{T}_1^{(k)} & \mathbf{T}_2^{(k)} & \mathbf{T}_3^{(k)} \end{bmatrix}^T$ from equation (3.6)

(3) Compute $\dfrac{\partial \Delta U_j^{(k)}}{\partial \Delta U_P^*}$ and $S_{im} \dfrac{\partial T_m^{(k)}}{\partial \Delta U_p^*}$ where $\Delta \mathbf{U}_p^* = \{ \Delta \mathbf{U}_1 \quad \Delta \mathbf{U}_2 \quad \Delta \mathbf{U}_3 \quad \mathbf{T}_4 \}$

(4) Obtain $\dfrac{\partial T_j^{*(k)}}{\partial X_p}$ and $\dfrac{\partial R_i^{*(k)}}{\partial X_p}$ (Note that $\dfrac{\partial T_j^{*(k)}}{\partial X_p} = \dfrac{\partial \Delta U_j^{(k)}}{\partial \Delta U_P^*}$ and

$\dfrac{\partial R_i^{*(k)}}{\partial X_p} = S_{im} \dfrac{\partial T_m^{(k)}}{\partial \Delta U_p^*}$ for an unbounded domain problem)

(5) Compute $A_{ip}^{*(k)} = K_{ij} \dfrac{\partial T_j^{*(k)}}{\partial X_p} - \dfrac{\partial R_i^{*(k)}}{\partial X_p}$

(6) Compute $B_i^{*(k)} = (-1)(K_{ij}T_j^{*(k)} - R_i^{*(k)})$

(7) Obtain $X_p^{(k+1)}$ by solving the equation $A_{ip}^{*(k)}(X_p^{(k+1)} - X_p^{(k)}) = B_i^{*(k)}$

(8) Obtain $\Delta \mathbf{U}_4^{(k+1)}$ and $\begin{bmatrix} \mathbf{T}_1^{(k+1)} & \mathbf{T}_2^{(k+1)} & \mathbf{T}_3^{(k+1)} \end{bmatrix}^T$ from equation (3.4) and equation (3.6), respectively

(9) Obtain $T_j^{*(k+1)}$ and $R_i^{*(k+1)}$

(10) Four criteria are employed to check the convergence of the numerical solutions. The first one is the relative error of $\left\| \Delta \mathbf{U}_1^{(k+1)} - \Delta \mathbf{U}_1^{(k)} \quad \Delta \mathbf{U}_2^{(k+1)} - \Delta \mathbf{U}_2^{(k)} \quad \Delta \mathbf{U}_3^{(k+1)} - \Delta \mathbf{U}_3^{(k)} \right\|_e / \left\| \Delta \mathbf{U}_1^{(0)} \quad \Delta \mathbf{U}_2^{(0)} \quad \Delta \mathbf{U}_3^{(0)} \right\|_e$. The second one is $\left\| \mathbf{T}_3^{(k+1)} - \mathbf{T}_3^{(k)} \right\|_e / \left\| \mathbf{T}_3^{(0)} \right\|_e$. The third one is $\left\| \mathbf{T}_4^{(k+1)} - \mathbf{T}_4^{(k)} \right\|_e / \left\| \mathbf{T}_4^{(0)} \right\|_e$ and the last one is the relative of $\left\| r^* \right\|_e / \left\| R^{*(0)} \right\|_e$, where $r_i^* = K_{ij}T_j^{*(k+1)} - R_i^{*(k+1)}$. The convergent solution ($T_j^{*(k+1)}$) is obtained when the all four criteria are less than the specified tolerance (Tol). Otherwise, go to the next iteration by updating $k = k + 1$ and repeat step (2) to (10).

## 3.5 Calculation of Intensity Factors

Once the jump of the generalized displacement $\Delta \mathbf{U}$ is obtained for any type of crack assumptions, the stress intensity factors $\{K_I \quad K_{II} \quad K_{III}\}$ and the electric intensity factor K_{IV} can be computed by using the formulation proposed by Rungamornrat and Mear (2008c). This fracture parameter is useful for measuring the amplitude of singularity of the stress and electric induction fields near the crack front.

Fig. 3.3. Flowchart of solution procedures by Newton-Raphson method for the Landis-type cracks.

CHAPTER IV

NUMERICAL RESULTS AND DISCUSSION

To demonstrate the accuracy and capabilities of the weakly-singular SGBEM, extensive numerical experiments are performed on various boundary value problems concerning both cracks in piezoelectric infinite and finite bodies under four types of electrical boundary conditions on the crack surface (e.g. permeable, impermeable, semi-permeable and Landis-type boundary conditions). First, a problem associated with a penny-shaped crack in an infinite medium under various loading conditions is treated. Since the analytical solution exists for this particular case, it provides a means to verify both the formulation and numerical implementation and, in addition, to demonstrate that the current technique can treat a special case of cracks in an infinite body. Next, a problem concerning a penny-shaped crack embedded in a finite cube is investigated. This problem is properly constructed such that it mimics exactly the problem of a penny-shaped crack in an infinite domain and, as a result, possesses the exact solution for comparison. This additional verification is crucial and confirms the correctness of the implementation in the context of finite bodies. Once the technique is validated through the extensive numerical experiments for both the infinite and finite boundary value problems, more complex problems are chosen to demonstrate the versatility of the current technique to model cracks and bodies of various geometries and under different loading conditions. Finally, the influence of electrical boundary conditions on the behavior of stress and electrical intensity factors is thoroughly explored.

In the analysis, a series of meshes is adopted to explore the rate of convergence of the numerical solutions and their dependency on the level of mesh refinement. In particular, 9-node crack-tip elements are employed to discretize the region near the crack front while the remaining of the boundary (i.e. the ordinary boundary and the majority of the crack surface) is discretized by standard 6-node and 8-node elements. Two types of piezoelectric materials considered in the investigations are assumed to be transversely isotropic with the generalized moduli to be the same as that for PZT-4 and PZT-5H (see Table 4.1).

Table 4.1 Properties of two transversely isotropic piezoelectric materials, PZT-4 obtained from Li et al. (2011) and PZT-5H obtained from Rungamornrat and Mear (2008c). The axis of material symmetry is directed along the x_3-axis direction.

		PZT-4	PZT-5H
Elastic constants $(\times 10^9 \text{Pa})$	E_{1111}	139	126
	E_{1122}	77.8	55.0
	E_{1133}	74.3	53.0
	E_{3333}	113	117.0
	E_{1313}	25.6	35.3
Piezoelectric constants (C/m^2)	E_{1143}	-6.98	-6.5
	E_{3343}	13.8	23.3
	E_{1341}	13.4	17.0
Dielectric permittivities $(\times 10^{-9} \text{ C/(Vm)})$	$-E_{1441}$	6.0	15.1
	$-E_{3443}$	5.47	13.0

4.1 Numerical Verification

To ensure that the weakly singular SGBEM can be employed to solve the piezoelectric fracture problem both infinite and finite bodies under several types of electrical boundary conditions, two problems with existing analytical solutions are considered first in order to examine the accuracy of the current technique. The first one is associated with a penny-shaped crack embedded in a piezoelectric infinite medium and the other corresponds to a penny-shaped crack embedded in a piezoelectric finite body that mimics exactly the problem of an isolated crack in an unbounded domain.

4.1.1 Penny-shaped crack in infinite medium under tensile loading

Consider a penny-shaped crack of radius a embedded in a transversely isotropic piezoelectric infinite medium with the poling axis directing in the x_3 direction as shown schematically in Fig. 4.1(a). The axis of material symmetry is assumed to be perpendicular to the crack surface and parallel to the poling direction. The medium is subjected to the uniform tensile stress $\sigma_o = 5\,\text{MPa}$ and the constant electric field $E_0 = 0.5\,\text{MV/m}$ at infinity along the poling direction as indicated in Fig. 4.1(b). The material properties of PZT-4 are chosen in the analysis and three meshes of the crack surface are adopted as depicted in Fig. 4.2; in particular, the coarsest mesh contains only 8 elements with 4 crack-tip elements and the finest mesh contains 64 elements with only 16 crack-tip elements.

The analytical solution for the mode-I stress intensity factor (K_I^{ex}) and the electric intensity factor (K_{IV}^{ex}) were reported by Chen et al. (2000) for impermeable cracks, Li and Lee (2004) for permeable and semi-permeable cracks, and Li et al. (2011) for Landis-type cracks. The numerical results of $\{K_I, K_{IV}\}$ normalized by the analytical solutions for four different types of crack assumptions are reported in Table 4.2 and 4.3. It is evident from this set of results that numerical solutions are in excellent agreement with the analytical solutions and exhibit only weak dependence on the level of mesh refinement. Especially, the error is less than 0.6% for results obtained from the coarse mesh and 0.1% for those obtained form the intermediate and fine meshes.
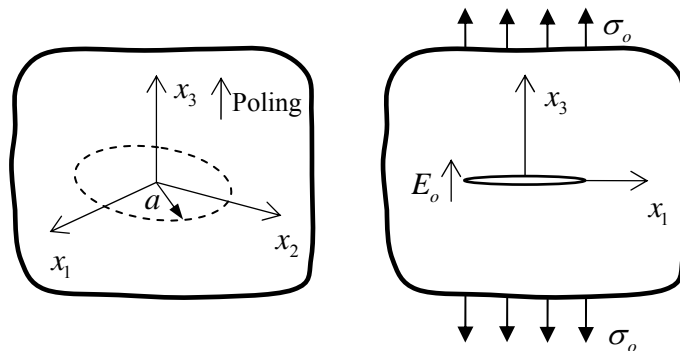
Fig. 4.1. (a) Schematic of a penny-shaped crack in a piezoelectric infinite medium and (b) piezoelectric infinite medium subjected to uniform tensile stress σ_0 and constant electric field E_0.

Mesh-1   Mesh-2   Mesh-3
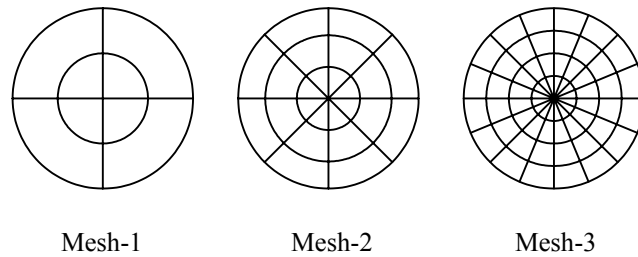
Fig. 4.2. Three meshes adopted in analysis

Table 4.2 Normalized intensity factors $\{K_I, K_{IV}\}$ for a penny-shaped crack subjected to remote uniform tensile stress $\sigma_o = 5$ MPa and uniform electric field $E_o = 0.5$ MV/m for impermeable and permeable cracks.

Mesh	Impermeable crack		Permeable crack	
	K_I / K_I^{ex}	K_{IV} / K_{IV}^{ex}	K_I / K_I^{ex}	K_{IV} / K_{IV}^{ex}
1	0.9944	0.9946	0.9945	0.9945
2	1.0002	1.0004	1.0003	1.0003
3	1.0005	1.0006	1.0006	1.0006

Table 4.3 Normalized intensity factors $\{K_I, K_{IV}\}$ for a penny-shaped crack subjected to remote uniform tensile stress $\sigma_o = 5$ MPa and uniform electric field $E_o = 0.5$ MV/m for semi-permeable and Landis-type cracks.

Mesh	Semi-permeable crack $\kappa_c = 8.85 x 10^{-12} \ C/(Vm)$		Landis-type crack $\kappa_c = 8.85 x 10^{-12} \ C/(Vm)$	
	K_I / K_I^{ex}	K_{IV} / K_{IV}^{ex}	K_I / K_I^{ex}	K_{IV} / K_{IV}^{ex}
1	0.9945	0.9945	0.9944	0.9945
2	1.0003	1.0003	1.0003	1.0003
3	1.0006	1.0006	1.0005	1.0006

4.1.2 Penny-shaped crack in infinite medium under shear loading

Consider a penny-shaped crack with radius a embedded in a transversely isotropic piezoelectric infinite medium as shown in Fig. 4.3(a). The penny-shaped crack is assumed to lie within the $x_1 - x_2$ plane and its normal directs along the axis of material symmetry and the poling direction. The crack is subjected to uniform shear traction $t_1^+ = -t_1^- = \tau_o$ as indicated in Fig. 4.3(b). The material properties of PZT-4 are used in the analysis and three meshes for the crack surface (coarse, intermediate and fine meshes) are adopted as shown in Fig. 4.4.

(a)   (b)
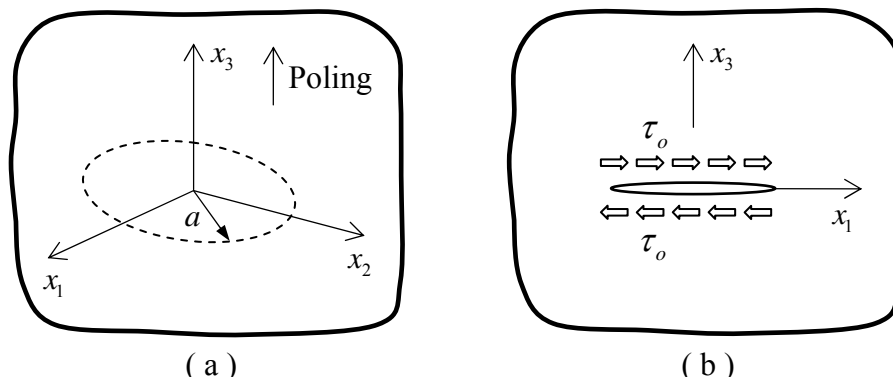
Fig. 4.3. (a) Schematic of a penny-shaped crack in a piezoelectric infinite medium and (b) penny-shaped crack subjected to uniform shear traction $t_1^+ = -t_1^- = \tau_o$

Mesh-1   Mesh-2   Mesh-3
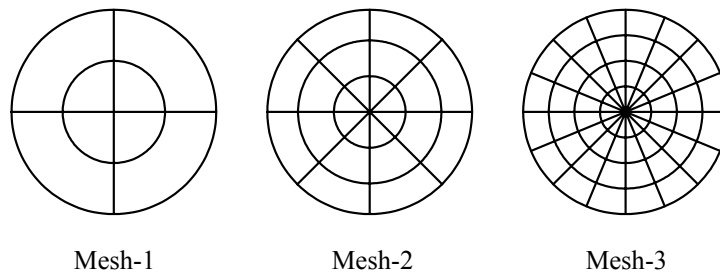
Fig. 4.4. Three meshes adopted in analysis

Numerical results obtained from the three meshes under four different electrical boundary conditions (i.e. permeable, impermeable, semi-permeable and Landis–type boundary conditions) along with the analytical solution of an impermeable crack given by Chen and Shioya (2000) are reported in Fig. 4.5 and 4.6.

Clearly, the computed intensity factors $\{K_{II}, K_{III}\}$ obtained from the three meshes for four types of cracks exhibit only weak dependence on the level of mesh refinement and this set of results is in good agreement with the analytical solution. Results obtained from the coarsest mesh (i.e. mesh-1), which contains only four elements along the crack front, are slightly different form the exact solution, whereas results obtained form the mesh-2 and mesh-3 are nearly indistinguishable from the analytical solution.

Once the convergence behavior of numerical solutions is confirmed, the behavior of the penny-shaped crack subjected to shear loading under four types of electrical boundary conditions is investigated via the numerical results obtained from the finest mesh (i.e. mesh-3). As be evident in Fig. 4.7, the mode-II and mode-III stress intensity factors for a penny-shaped crack under shear loading are identical for all four types of crack assumptions. This finding is in agreement with the work of Chen and Shioya (2000), who pointed out that K_{II} and K_{III} for impermeable and permeable cracks are identical, and this is also consistent with the discussion of Chen and Lim (2005). This conclusion suggests that the electrical boundary conditions have no effect on the stress intensify factors K_{II} and K_{III} for a penny-shaped crack under surface shear loading as long as it introduces no crack opening.
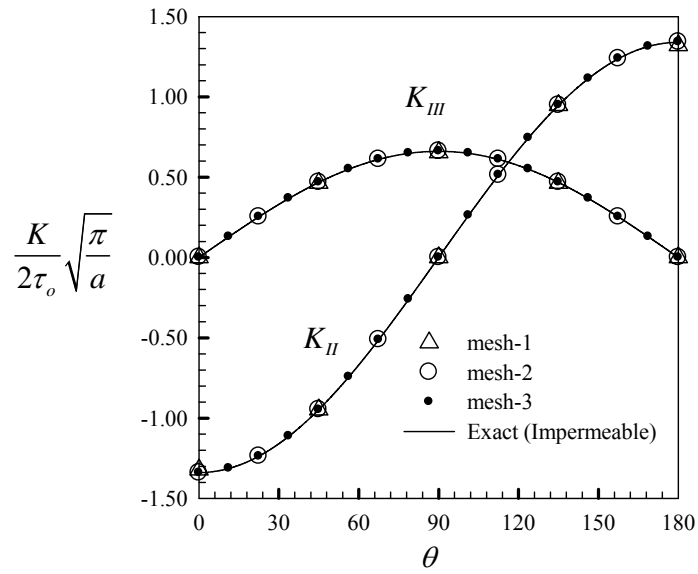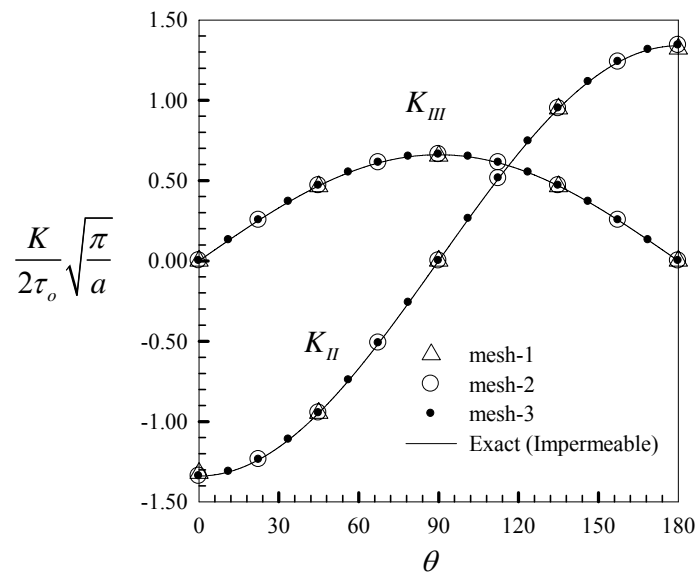
Fig. 4.5. Normalized stress intensity factors $\{K_{II}, K_{III}\}$ for a penny-shaped crack in a piezoelectric infinite medium subjected to uniform shear traction for (a) impermeable crack and (b) permeable crack. Note that the exact solution is obtained from Chen and Shioya (2000) for impermeable crack.
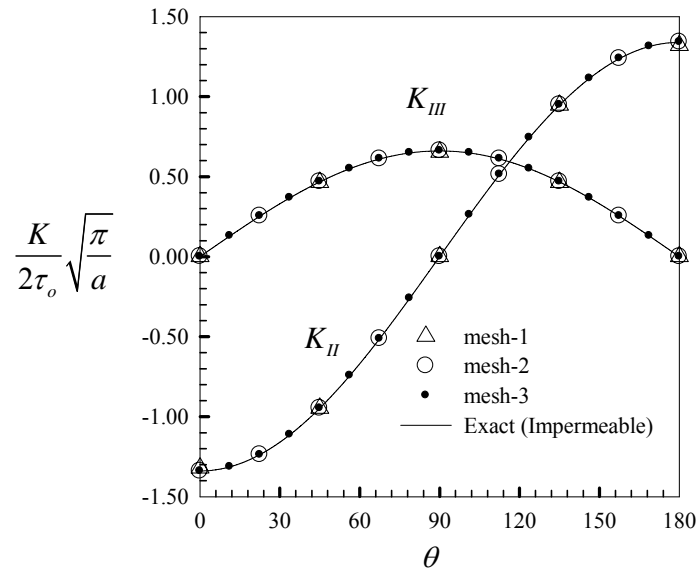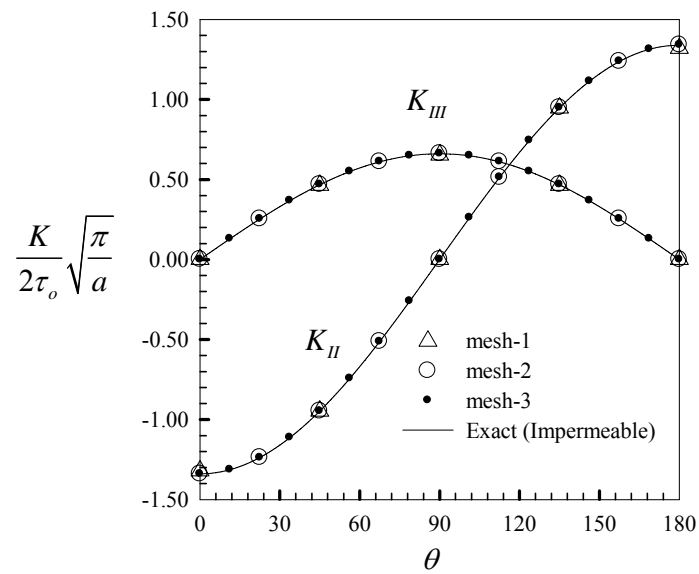
Fig. 4.6. Normalized stress intensity factors $\{K_{II}, K_{III}\}$ for a penny-shaped crack in a piezoelectric infinite medium subjected to uniform shear traction for (a) semi-permeable crack and (b) Landis-type crack. Note that the exact solution is obtained from Chen and Shioya (2000) for impermeable crack.
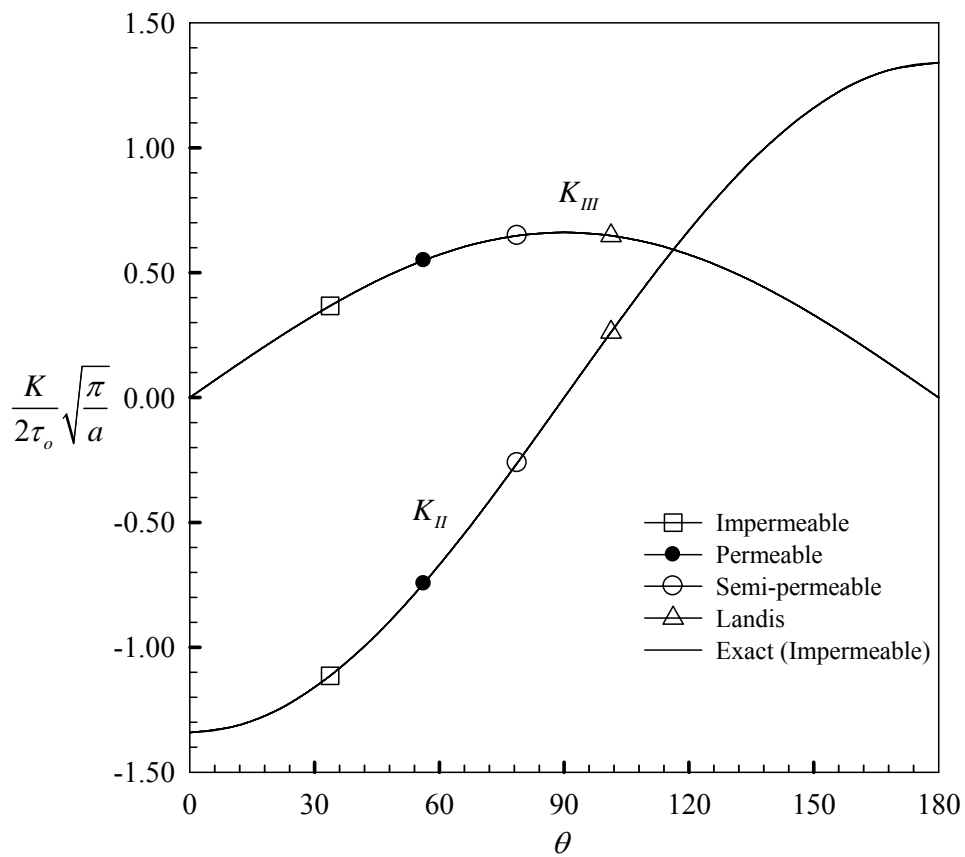
Fig. 4.7. Normalized stress intensity factors $\{K_{II}, K_{III}\}$, which is obtained from the mesh-3, for a penny-shaped crack in a piezoelectric infinite medium subjected to uniform shear traction for four types of crack assumptions. Note that the exact solution is obtained from Chen and Shioya (2000) for impermeable crack.

4.1.3 Penny-shaped crack in cube under tensile loading

For two previous numerical experiments, problems of a penny-shaped crack in a piezoelectric infinite medium subjected to both tension and shear loading under four types of crack assumptions were validated. Here, in this example, a problem of a penny-shaped crack in a finite body is examined. While the exact solution of a crack in a piezoelectric finite medium has not been available in the literature, this situation can be simulated by truncating the problem of an isolated crack in an infinite domain whose exact stress and electric induction fields are known.

Consider a penny-shaped crack of radius a embedded in a transversely isotropic piezoelectric infinite medium as shown schematically in Fig. 4.8(a). The crack surface is oriented such that it is perpendicular to the axis of material symmetry. The mixed loading condition between the uniform normal traction σ_o and uniform surface electric charge d_o with the ratio $(\sigma_o/E_{3333})/(d_o/E_{3343}) = 0.20$ is investigated. The analytical solutions for the generalized stress within the domain for impermeable and semi-permeable cracks, denoted by σ_{iJ}^{ex}, were reported by Chen et al. (2000) and Li and Lee (2004), respectively. To construct an equivalent finite domain problem, a cube of material of dimensions $2w$ x $2w$ x $2w$ with $a/w = 0.5$ is chosen such that it contains the crack at its center as shown in Fig. 4.9. On the outer boundary of this cube, the generalized traction obtained from the exact generalized stress, i.e. $t_J^{ex} = \sigma_{iJ}^{ex}n_i$ where n_i denotes an outward unit normal to the boundary, is applied throughout. The material properties of PZT-5H are chosen in the analysis and three meshes are adopted as shown in Fig. 4.10; the first mesh (mesh-1) which is very coarse consists of only eight elements for the crack surface and 16 elements for each side of the cube whereas the intermediate and fine meshes (mesh-2 and mesh-3) consists of 16 and 36 elements for the crack surface and 36 and 64 elements for each side of the cube, respectively.

Fig. 4.8. (a) Schematic of a penny-shaped crack in a piezoelectric infinite medium and (b) penny-shaped crack subjected to uniform normal traction $t_3^+ = -t_3^- = \sigma_o$ and uniform surface electric charge $t_4^+ = -t_4^- = d_o$

Fig. 4.9. Cube containing a penny-shaped crack subjected to prescribed traction data obtained from the exact generalized stress of a problem of a penny shaped crack in an unbounded domain

Side of cube   Crack

Fig. 4.10. Three meshes adopted in the analysis. Note that the discretization of a typical side of the cube is shown along with that for the crack.

For this particular loading condition, only the mode-I stress intensity factor (K_I) and the electric intensity factor (K_{IV}) exist and they are constant along the crack front. Normalized K_I and K_{IV} computed from the three meshes, under impermeable and semi-permeable boundary conditions, are reported in Table 4.4. As be evident from this set of results, numerical solutions are very accurate and exhibit only slight dependence on the discretization. In particular, the error is less than 0.7% for results obtained from the mesh-1 and 0.1% for those obtained from the mesh-2 and mesh-3. It is worth noting that the achievement of such highly accurate intensity factors while using only relatively coarse meshes for the crack surface is due to the use of special crack-tip elements in the discretization along with the direct means to extract the intensity factors in terms of the crack-front nodal data. Note in addition that the need to employ several elements on each side of the cube is primarily dictated by the need to accurately capture the complex distribution of the exact generalized surface traction.

Table 4.4 Normalized intensity factors $\{K_I, K_{IV}\}$ for finite domain-based simulation of a penny-shaped crack in an unbounded domain subjected to uniform normal traction σ_o and uniform surface electric charge d_o for impermeable and semi-permeable cracks.

Mesh	Impermeable crack		Semi-permeable crack	
	K_I / K_I^{ex}	K_{IV} / K_{IV}^{ex}	K_I / K_I^{ex}	K_{IV} / K_{IV}^{ex}
1	0.9933	0.9934	0.9933	0.9933
2	0.9995	0.9994	0.9995	0.9995
3	1.0002	1.0002	1.0002	1.0002

4.1.4 Penny-shaped crack in cube under uniform shear traction

Consider a penny-shaped crack of radius a embedded in a transversely isotropic piezoelectric infinite medium as shown schematically in Fig. 4.11(a). The axis of material symmetry is assumed to direct along the x_3-axis and is perpendicular to the crack surface. The crack is subjected to uniform shear traction τ_o as shown in Fig. 4.11(b) and the corresponding exact generalized stress field σ_{iJ}^{ex} was proposed by Chen and Shioya (2000) for impermeable cracks. To construct an equivalent finite domain problem, a cube of dimensions $2w$ x $2w$ x $2w$ containing the crack at its center with $a/w = 0.5$ as shown in Fig. 4.12 is taken in the analysis. The exact generalized traction t_J^{ex} acting to the boundary of the cube is computed by using the relation $t_J^{ex} = \sigma_{iJ}^{ex} n_i$ where n_i is outward unit normal vector to the boundary. The material properties of PZT-5H are employed in the analysis and three meshes are adopted as shown in Fig. 4.13.
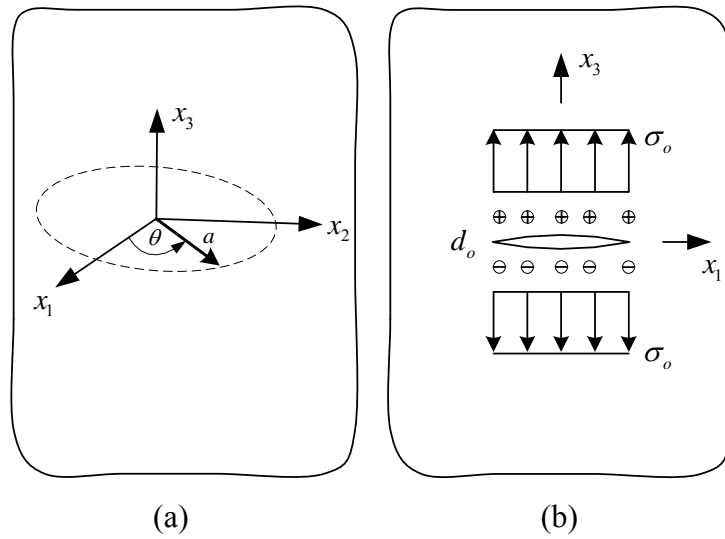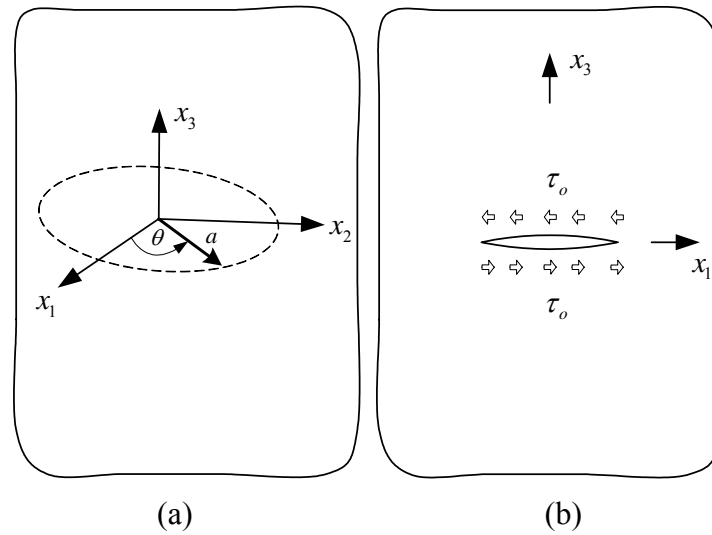
Fig. 4.11. (a) Schematic of a penny-shaped crack in a piezoelectric infinite medium and (b) penny-shaped crack subjected to uniform shear traction $t_1^+ = -t_1^- = \tau_o$
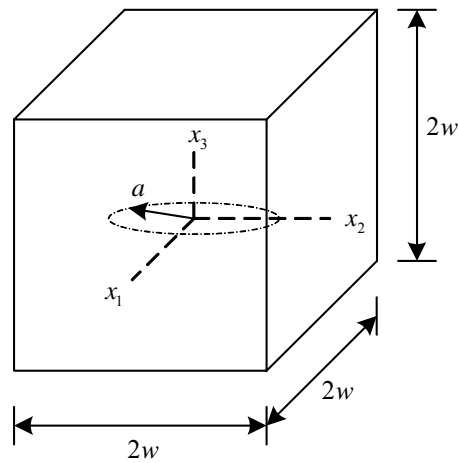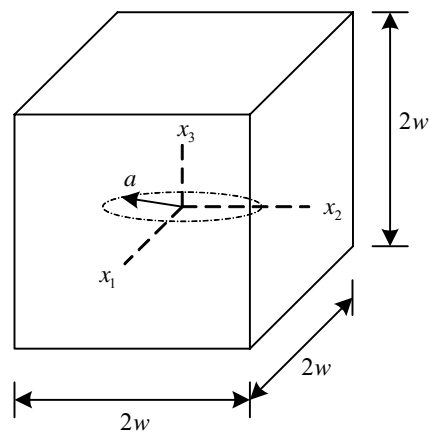

Fig. 4.12. Cube containing penny-shaped crack subjected to prescribed traction data obtained from the exact generalized stress of a problem of a penny-shaped crack in an unbounded domain
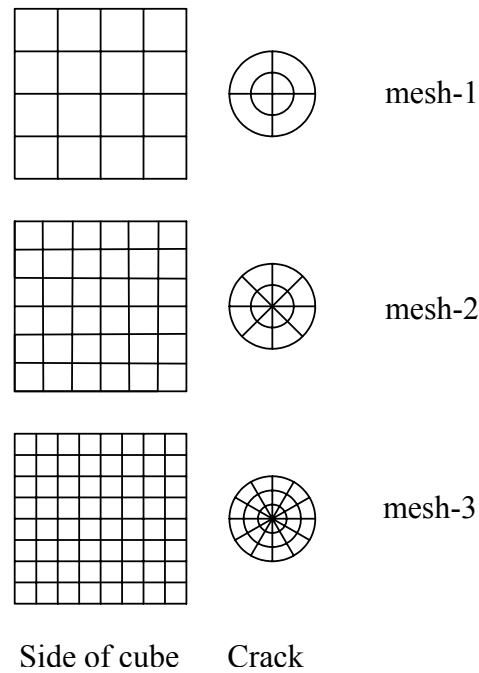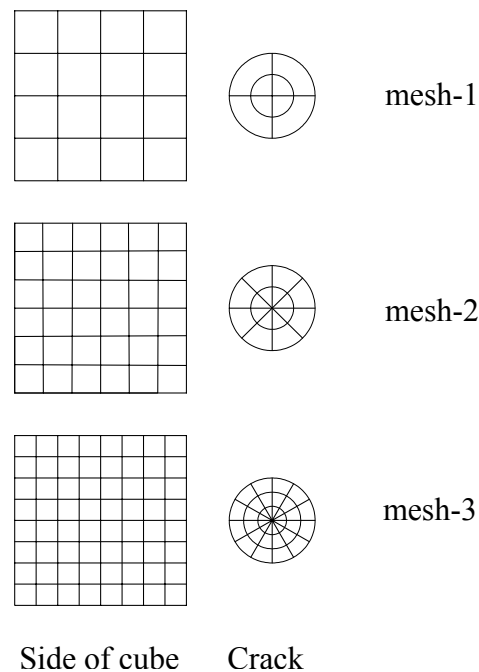
Fig. 4.13. Three meshes adopted in the analysis. Note that the discretization of a typical side of the cube is shown along with that for the crack.

For this particular loading condition, it is different from the previous example presented in subsection 4.1.3, the uniform shear traction acting on the crack surface leads to non-zero mode-II and mode-III stress intensity factors $\{K_{II}, K_{III}\}$ and, in addition, they are functions of position along the crack front (see Chen and Shioya, 2000). The normalized mode-II and mode-III stress intensity factors obtained from the three meshes for impermeable and semi-permeable cracks are reported in Fig. 4.14(a) and 4.14(b) along with the exact solution of the impermeable crack. Once again, this set of numerical results is in good agreement with the exact solution and exhibits only mild dependence on the mesh refinement. Results obtained from the mesh-1 differ slightly from the exact solution while those obtained from the mesh-2 and mesh-3 are nearly identical to the exact solution.
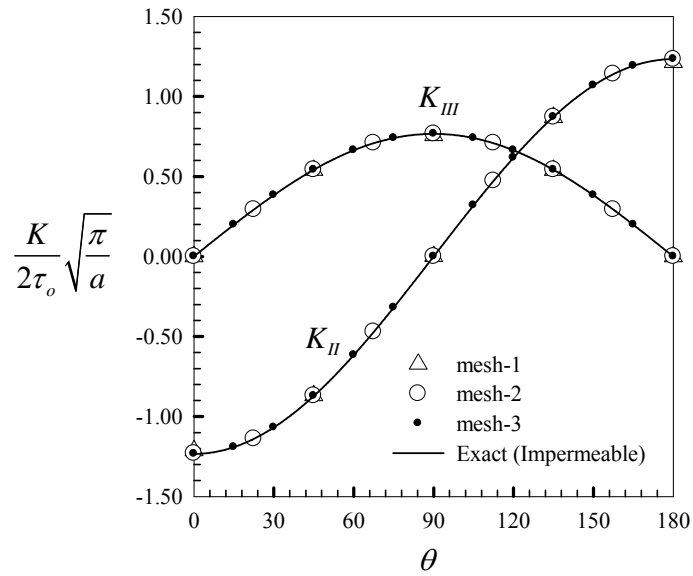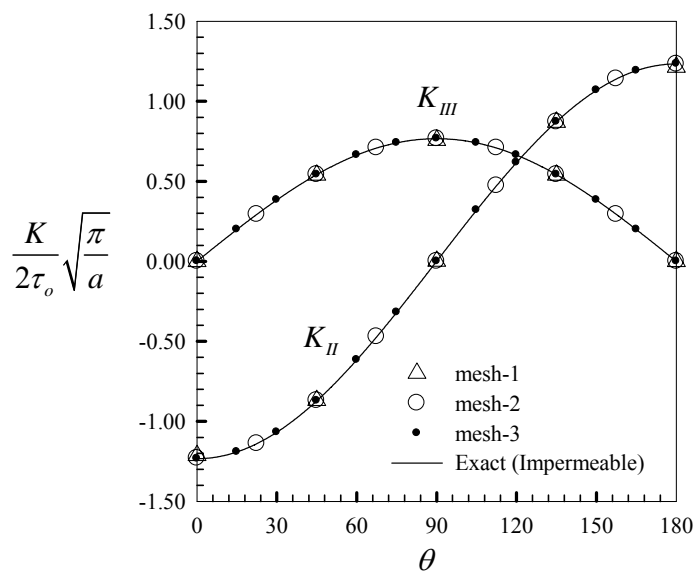
Fig. 4.14. Normalized stress intensity factors $\{K_{II}, K_{III}\}$ for the finite domain-based simulation of a penny-shaped crack in an unbounded domain subjected to uniform shear traction for (a) impermeable crack and (b) semi-permeable crack. Note that the exact solution is obtained from an isolated penny-shaped crack subjected to uniform shear traction under an impermeable assumption.

4.1.5 Cube containing penny-shaped crack under normal traction and surface electric charge

As be evident in previous numerical experiments, the problem concerning an isolated crack in an unbounded domain with existing analytical solutions for four types of crack assumptions (i.e. permeable, impermeable, semi-permeable and Landis-type cracks) were examined, while the problem associated with the finite domain containing a crack under impermeable and semi-permeable boundary conditions were validated by mimicking exactly the isolated crack problem whose exact generalized stress field are available (Chen et al., 2000; Chen and Shioya, 2000; Li and Lee, 2004). A question arises as how to validate the finite domain problem containing crack under other types of crack assumptions (e.g. Landis-type cracks) when there is no analytical or benchmark solution for comparison. Here, the validated impermeable scheme is proposed to generate the benchmark solutions to verify results of other types of crack models (e.g. permeable, semi-permeable and Landis-type cracks) and this strategy is clearly explained below.

4.1.5.1 Permeable cracks solved by impermeable scheme

For permeable cracks, the generalized traction ($\mathbf{T}_B$) and the generalized displacement ($\mathbf{U}_B$) on the boundary of the body, along with the surface electric charge $\mathbf{T}_4$ and the jump of the mechanical displacement $\begin{bmatrix} \Delta\mathbf{U}_1 & \Delta\mathbf{U}_2 & \Delta\mathbf{U}_3 \end{bmatrix}^T$ on the crack surface are obtained by solving the system of linear equations (3.1). Such vector $\begin{bmatrix} \Delta\mathbf{U}_1 & \Delta\mathbf{U}_2 & \Delta\mathbf{U}_3 \end{bmatrix}^T$ along with the jump of the electric potential $\Delta\mathbf{U}_4$, which is known a priori and equal to zero, are used to calculate the intensity factors of the permeable crack. While the solved vector $\mathbf{T}_4$ along with the known mechanical traction $\begin{bmatrix} \mathbf{T}_1 & \mathbf{T}_2 & \mathbf{T}_3 \end{bmatrix}^T$ are then used as the input data in the impermeable scheme to generate the benchmark solutions.

For the impermeable scheme, when the generalized traction $\mathbf{T}$ is known (along with the prescribed data on the outer boundary), the jump of the generalized displacement ($\Delta\mathbf{U}$) can be obtained by solving the system of linear equations (3.1)

and the vector $\Delta\mathbf{U}$ is used to calculate the intensity factors of the permeable crack. Finally, the relative error of the stress and electric intensity factors comparing between those obtained using the permeable condition and those obtained by the impermeable scheme, defined by $\left| K^{\text{Permea}} / K_{ref}^{\text{Permea (Imper)}} - 1 \right| \times 100$ and $\left| K_{IV}^{\text{Permea}} / K_{4,ref}^{\text{Permea (Imper)}} - 1 \right| \times 100$ can be evaluated.

4.1.5.2 Semi-permeable cracks solved by impermeable scheme

For semi-permeable cracks, the unknown vectors $\begin{bmatrix} \mathbf{T}_B & \mathbf{U}_B & \Delta\mathbf{U}_1 & \Delta\mathbf{U}_2 & \Delta\mathbf{U}_3 & \mathbf{T}_4 \end{bmatrix}$ are obtained by solving the system of linear equations (3.1) along with the additional equation (3.4) by using the Newton-Raphson method. The vector $\begin{bmatrix} \Delta\mathbf{U}_1 & \Delta\mathbf{U}_2 & \Delta\mathbf{U}_3 \end{bmatrix}^T$ along with the jump of the electric potential $\Delta\mathbf{U}_4$, which is originally unknown and it can be obtained after solving the equations (3.1) along with (3.4), are used to calculate the intensity factors of the semi-permeable crack. Next, the solved vector $\mathbf{T}_4$ along with the known mechanical traction $\begin{bmatrix} \mathbf{T}_1 & \mathbf{T}_2 & \mathbf{T}_3 \end{bmatrix}^T$ is used as the input data for the impermeable scheme.

Once the generalized traction $\mathbf{T}$ is prescribed (along with the prescribed data on the outer boundary, the jump of the generalized displacement ($\Delta\mathbf{U}$) can be computed by the impermeable scheme and the intensity factors can finally be obtained. The relative error between the semi-permeable solutions and those obtained by the impermeable scheme for the stress and electric intensity factors, defined by $\left| K^{\text{Semi}} / K_{ref}^{\text{Semi (Imper)}} - 1 \right| \times 100$ and $\left| K_{IV}^{\text{Semi}} / K_{4,ref}^{\text{Semi (Imper)}} - 1 \right| \times 100$ can subsequently be computed.

4.1.5.3 Landis-type cracks solved by impermeable scheme

For Landis-type cracks, the unknown vectors $\begin{bmatrix} \mathbf{T}_B & \mathbf{U}_B & \Delta\mathbf{U}_1 & \Delta\mathbf{U}_2 & \Delta\mathbf{U}_3 & \mathbf{T}_4 \end{bmatrix}$ are obtained by solving the system of linear equations (3.1) along with the two additional equations (3.4) and (3.6) using the Newton-Raphson method. The vector $\begin{bmatrix} \Delta\mathbf{U}_1 & \Delta\mathbf{U}_2 & \Delta\mathbf{U}_3 \end{bmatrix}^T$ along with the jump of the

electric potential $\Delta \mathbf{U}_4$ (obtained after solving equations (3.1) along with (3.4) and (3.6)) are used to calculate the intensity factors of Landis-type cracks. While the vector $\mathbf{T}_4$ along with the mechanical traction $\begin{bmatrix} \mathbf{T}_1 & \mathbf{T}_2 & \mathbf{T}_3 \end{bmatrix}^T$ (obtained after solving the equation (3.1) along with (3.4) and (3.6)) is used as the input data for the impermeable scheme.

Once, the jump of generalized traction ($\mathbf{T}$) is prescribed (along with the prescribed data on the outer boundary), the jump of the generalized displacement $\Delta \mathbf{U}$ can be obtained by the impermeable scheme and the vector $\Delta \mathbf{U}$ are then used to compute the intensity factors. Finally, the relative error between the Landis-type solutions and those obtained by the impermeable scheme for the stress and electric intensity factors, defined by $\left| K^{\text{Landis}} / K_{ref}^{\text{Landis (Imper)}} - 1 \right| \times 100$ and $\left| K_{IV}^{\text{Landis}} / K_{4,ref}^{\text{Landis (Imper)}} - 1 \right| \times 100$, is computed.

To confirm that the weakly singular SGBEM can be employed to solve cracks in a piezoelectric finite body under several types of crack assumptions although there is no analytical or reference solution for comparison, solutions of any finite domain problem containing crack can be verified by the impermeable scheme as described above.

Consider a cube containing a penny-shaped crack at its center and subjected to the uniform loadings at the top and bottom surfaces, while the remaining boundary including the crack is free of traction and surface electric charge as shown schematically in Fig. 4.15. The cube is made of a transversely isotropic, piezoelectric material named PZT-5H and the dimension of the cube is defined by $2w$ x $2w$ x $2w$ with $a/w = 0.5$ where a is the radius of the crack. Three loading cases, (i) the purely uniform normal traction ($\sigma_o = 1.0$), (ii) the purely uniform surface electric charge ($d_o = 1.0$) and (iii) the coupled uniform normal traction ($\sigma_o = 1.0$) and uniform surface electric charge ($d_o = 1.0$) with the loading ratio $(\sigma_o / E_{3333})/(d_o / E_{3343}) = 0.20$, are investigated, and three meshes adopted in the analysis are shown in Fig. 4.16.

The relative error, in percentage, defined by $\left| K / K_{ref}^{\text{(Imper)}} - 1 \right| \times 100$ for three types of crack assumptions (i.e. permeable, semi-permeable and Landis-type cracks)

are reported in Tables 4.5 to 4.7 where $K_{ref}^{(Imper)}$ is the computed intensity factor using the impermeable scheme and the finest mesh (i.e. mesh-3). It is found that the intensity factors obtained from the three meshes are in good agreement and they exhibit only mild dependence on the mesh refinement. More specially, the relative error for the coarsest mesh (i.e. mesh-1), which contains only one element for each side of the cube and eight elements for the entire crack surface, is less than 1.95% whereas the relative error obtained from the mesh-2 is less than 0.25%. This additional verification is crucial and confirms the correctness of the implementation in the context of finite cracked bodies under various types of electrical boundary conditions. Finally, it should be mentioned that, in these numerical experiments, the intensity factors K_I and K_{IV} for the purely uniform surface electric charge ($\sigma_o = 0.0$, $d_o = 1.0$) under permeable and semi-permeable conditions vanish.
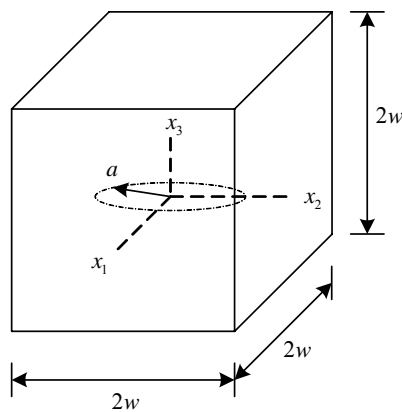

Fig. 4.15. Schematic of cube containing penny-shaped crack and subjected to uniform mechanical and electrical loadings at the top and bottom surfaces
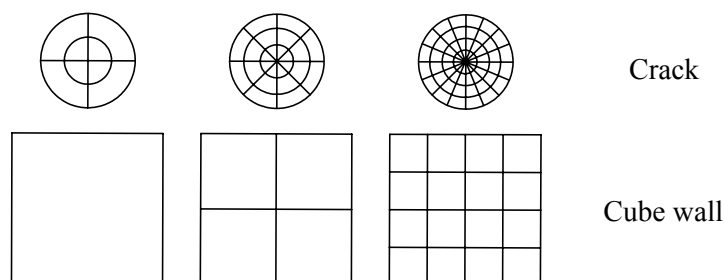

Fig. 4.16. Three meshes adopted in the analysis

Table 4.5 The relative error, in percentage, for a cube containing penny-shaped permeable crack and subjected to two loading cases.

Mesh	$\sigma_o = 1.0,\ d_o = 0.0$		$\sigma_o = 1.0,\ d_o = 1.0$	
	$\left\|\dfrac{K_I^{\text{Permea}}}{K_{1,ref}^{\text{Permea (Imper)}}} - 1\right\| \times 100$	$\left\|\dfrac{K_{IV}^{\text{Permea}}}{K_{4,ref}^{\text{Permea (Imper)}}} - 1\right\| \times 100$	$\left\|\dfrac{K_I^{\text{Permea}}}{K_{1,ref}^{\text{Permea (Imper)}}} - 1\right\| \times 100$	$\left\|\dfrac{K_{IV}^{\text{Permea}}}{K_{4,ref}^{\text{Permea (Imper)}}} - 1\right\| \times 100$
1	1.9265	1.9265	1.9277	1.9277
2	0.2020	0.2020	0.2018	0.2018
3	0.0000	0.0000	0.0000	0.0000

Table 4.6 The relative error, in percentage, for a cube containing penny-shaped semi-permeable crack and subjected to two loading cases.

Mesh	$\sigma_o = 1.0,\ d_o = 0.0$		$\sigma_o = 1.0,\ d_o = 1.0$	
	$\left\|\dfrac{K_I^{\text{Semi}}}{K_{1,ref}^{\text{Semi (Imper)}}} - 1\right\| \times 100$	$\left\|\dfrac{K_{IV}^{\text{Semi}}}{K_{4,ref}^{\text{Semi (Imper)}}} - 1\right\| \times 100$	$\left\|\dfrac{K_I^{\text{Semi}}}{K_{1,ref}^{\text{Semi (Imper)}}} - 1\right\| \times 100$	$\left\|\dfrac{K_{IV}^{\text{Semi}}}{K_{4,ref}^{\text{Semi (Imper)}}} - 1\right\| \times 100$
1	1.9256	1.9214	1.9300	1.9236
2	0.2020	0.2022	0.2018	0.2012
3	0.0000	0.0000	0.0000	0.0000

Table 4.7 The relative error, in percentage, for a cube containing penny-shaped Landis-type crack and subjected to three loading cases.

Mesh	$\sigma_o = 1.0,\ d_o = 0.0$		$\sigma_o = 0.0,\ d_o = 1.0$		$\sigma_o = 1.0,\ d_o = 1.0$	
	$\left\|\dfrac{K_I^{\text{Landis}}}{K_{1,ref}^{\text{Landis (Imper)}}} - 1\right\| \times 100$	$\left\|\dfrac{K_{IV}^{\text{Landis}}}{K_{4,ref}^{\text{Landis (Imper)}}} - 1\right\| \times 100$	$\left\|\dfrac{K_I^{\text{Landis}}}{K_{1,ref}^{\text{Landis (Imper)}}} - 1\right\| \times 100$	$\left\|\dfrac{K_{IV}^{\text{Landis}}}{K_{4,ref}^{\text{Landis (Imper)}}} - 1\right\| \times 100$	$\left\|\dfrac{K_I^{\text{Landis}}}{K_{1,ref}^{\text{Landis (Imper)}}} - 1\right\| \times 100$	$\left\|\dfrac{K_{IV}^{\text{Landis}}}{K_{4,ref}^{\text{Landis (Imper)}}} - 1\right\| \times 100$
1	1.9250	1.9209	1.9316	1.9336	1.9341	1.9277
2	0.2020	0.2023	0.2081	0.2087	0.2022	0.2016
3	0.0000	0.0000	0.0000	0.0000	0.0000	0.0000

4.2 More Complex Boundary value Problems

Once the weakly singular SGBEM is validated through various numerical experiments to ensure that this technique is capable of modeling both infinite and finite piezoelectric cracked bodies under various types of electrical boundary conditions, more complex boundary value problems are chosen to demonstrate the versatility of the current technique to model cracks and bodies of various geometries and under different loading conditions.

4.2.1 Spherical cap crack in infinite medium under tensile loading

Consider a spherical cap crack embedded in a transversely isotropic piezoelectric infinite medium, which is made of PZT-4, as shown in Fig. 4.17. The geometry of the crack surface is defined by

$$x_1 = a\sin\gamma\cos\beta, \ x_2 = a\sin\gamma\sin\beta, \ x_3 = a\cos\gamma \qquad (4.1)$$

where a is the radius of the spherical crack, $\beta \in [0, 2\pi]$ and $\gamma \in [0, \theta]$ with θ denoting half subtended angle of the surface. The axis of material symmetry and the poling direction are along the x_3 axis. Three meshes of a spherical cap crack as shown in Fig. 4.18 are employed in this investigation. The coarsest mesh consists of 16 elements whereas the intermediate and finest meshes consist of 48 elements and 120 elements, respectively. The piezoelectric medium is subjected to remote uniaxial tension $\sigma_o = 5$ MPa and uniform electric field $E_o = 0.5$ MV/m in the x_3 direction and the half subtended angle of the crack surface is chosen to be $\theta = 45^o$.
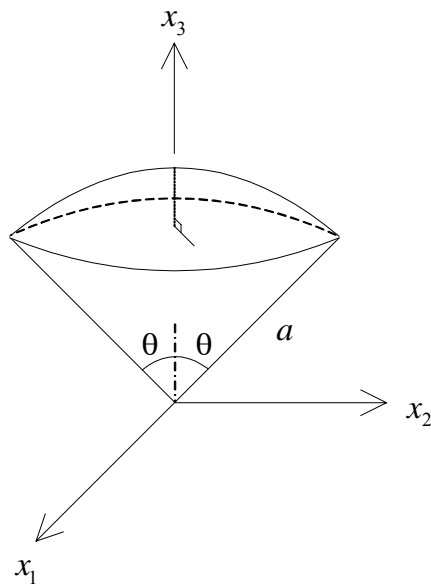
Fig. 4.17. Schematic of a spherical cap crack in a piezoelectric infinite medium

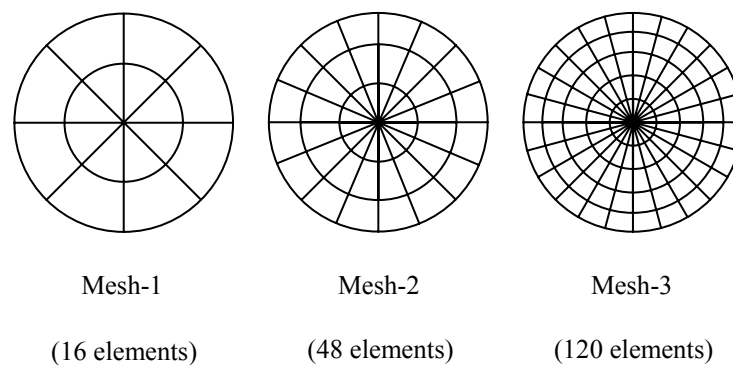| Mesh-1 | Mesh-2 | Mesh-3 |
| (16 elements) | (48 elements) | (120 elements) |

Fig. 4.18. Three meshes of a spherical cap crack adopted in the analysis

Numerical results for nonzero intensity factors, normalized by the result obtained from the mesh-3, are reported in Tables 4.8 and 4.9. It is found that the numerical results obtained from the three meshes are in good agreement; especially, the discrepancy of results obtained from the coarsest and intermediate meshes and those from the mesh-3 is less than 1.05% and 0.28%, respectively. It should be noted that the coarsest mesh consists of only eight elements for a region near the crack front and eight elements for the rest of the crack surface.

Table 4.8 Normalized intensity factors $\{K_I, K_{II}, K_{IV}\}$ for a spherical cap crack subjected to remote uniform tensile stress $\sigma_o = 5$ MPa and uniform electric field $E_o = 0.5$ MV/m for impermeable and permeable cracks

Mesh	Impermeable crack			Permeable crack		
	K_I / K_1^{ref}	K_{II} / K_2^{ref}	K_{IV} / K_4^{ref}	K_I / K_1^{ref}	K_{II} / K_2^{ref}	K_{IV} / K_4^{ref}
1	1.0103	0.9974	0.9989	1.0025	0.9973	0.9991
2	1.0026	0.9996	0.9998	1.0007	0.9996	0.9999
3	1.0000	1.0000	1.0000	1.0000	1.0000	1.0000

Table 4.9 Normalized intensity factors $\{K_I, K_{II}, K_{IV}\}$ for a spherical cap crack subjected to remote uniform tensile stress $\sigma_o = 5$ MPa and uniform electric field $E_o = 0.5$ MV/m for semi-permeable and Landis-type cracks

Mesh	Semi-permeable crack			Landis-type crack		
	$\kappa_c = 8.85x10^{-12}$ $C/(Vm)$			$\kappa_c = 8.85x10^{-12}$ $C/(Vm)$		
	K_I / K_1^{ref}	K_{II} / K_2^{ref}	K_{IV} / K_4^{ref}	K_I / K_1^{ref}	K_{II} / K_2^{ref}	K_{IV} / K_4^{ref}
1	1.0026	0.9975	0.9976	1.0026	0.9984	0.9959
2	1.0007	0.9996	0.9991	1.0005	0.9998	0.9984
3	1.0000	1.0000	1.0000	1.0000	1.0000	1.0000

4.2.2 Inclined elliptical crack in infinite medium under tensile loading

Consider an elliptical crack embedded in a transversely isotropic piezoelectric infinite medium as shown in Fig. 4.19. The axis of material symmetry and the poling direction of the piezoelectric medium are along the x_3-axis. The crack plane is oriented such that the angle β between the major axis and the x_1-axis is equal to 45°. The major and minor axes of the crack are denoted by $2a$ and $2b$, respectively. The aspect ratio of the inclined elliptical crack is chosen to be $a/b = 2$ and the medium is subjected to the uniform tensile stress $\sigma_o = 5\,\text{MPa}$ and the constant electric field $E_o = 0.5\,\text{MV/m}$ at infinity along the poling direction. The material properties of PZT-4 are chosen in the analysis and three meshes of the crack surface are adopted as depicted in Fig. 4.20.

Computed stress intensity factors $\{K_I, K_{II}, K_{III}\}$ and electric intensity factor $\{K_{IV}\}$ for impermeable, permeable, semi-permeable and Landis-type cracks are reported in Fig. 4.21 to 4.24, respectively. It is found that, for all four types of electrical boundary conditions, numerical results obtained from the mesh-1 is slightly different from those obtained from the mesh-3 whereas results obtained from the mesh-2 is nearly indistinguishable from the mesh-3.

Once convergence of the numerical results is investigated, the influence of the electrical boundary conditions upon the stress intensity factors $\{K_I, K_{II}, K_{III}\}$ and the electric intensity factor $\{K_{IV}\}$ are explored using results from mesh-3 as shown in Fig. 4.25 and 4.26. It can be inferred from Fig. 4.25 that K_I of impermeable, permeable and semi-permeable cracks are nearly identical and are greater than those of the Landis-type crack. In addition, the mode-II stress intensity factor (K_{II}) of the impermeable and permeable cracks provides the bounds for both semi-permeable and Landis-type case and results of the semi-permeable and Landis-type cracks are nearly identical.

For mode-III stress intensity factor, K_{III} of the permeable and impermeable cracks are, respectively, the upper and lower bounds of that of the semi-permeable

and Landis-type cracks, and results of the semi-permeable and Landis-type cracks are nearly identical. For the electric intensity factor, Fig. 4.26 indicates that K_{IV} of the impermeable and permeable cracks are the upper and lower bounds of that of the semi-permeable and Landis-type cracks, while results of the semi-permeable crack is greater than those of the Landis-type crack.
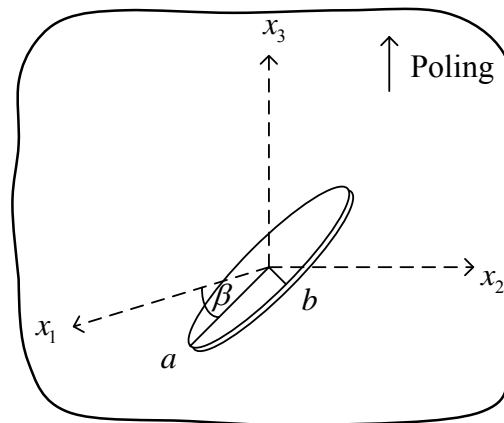

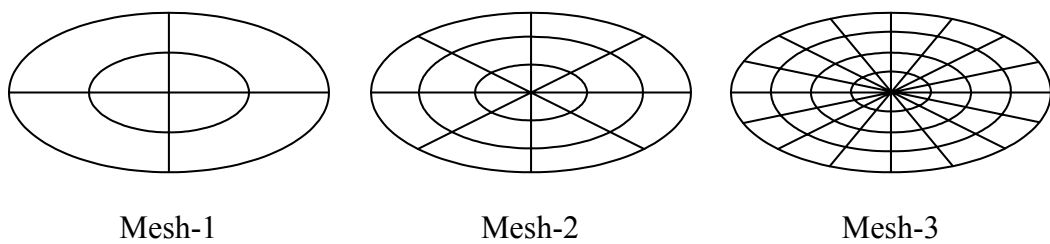Fig 4.19. Schematic of inclined elliptical crack in piezoelectric infinite medium

Mesh-1   Mesh-2   Mesh-3

Fig. 4.20. Three meshes adopted in the analysis of elliptical crack in piezoelectric infinite medium
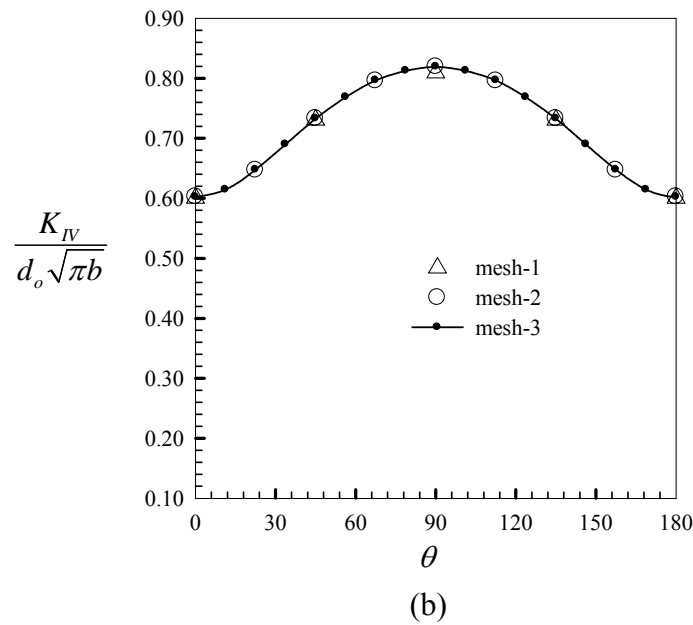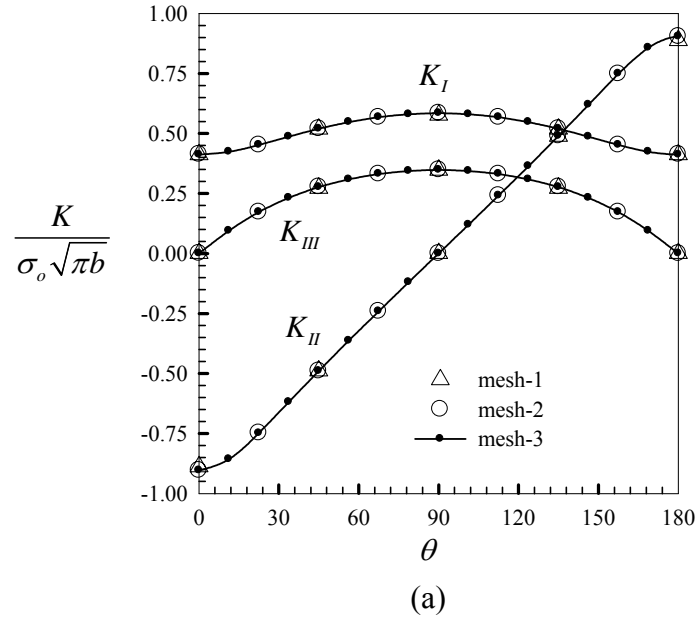
Fig. 4.21. Normalized intensity factors for an inclined elliptical crack in an unbounded domain subjected to uniform tensile stress $\sigma_o = 5\,\text{MPa}$ and constant electric field $E_0 = 0.5\,\text{MV/m}$ for impermeable crack: (a) stress intensity factors $\{K_I,\ K_{II},\ K_{III}\}$ and (b) electric intensity factor $\{K_{IV}\}$.
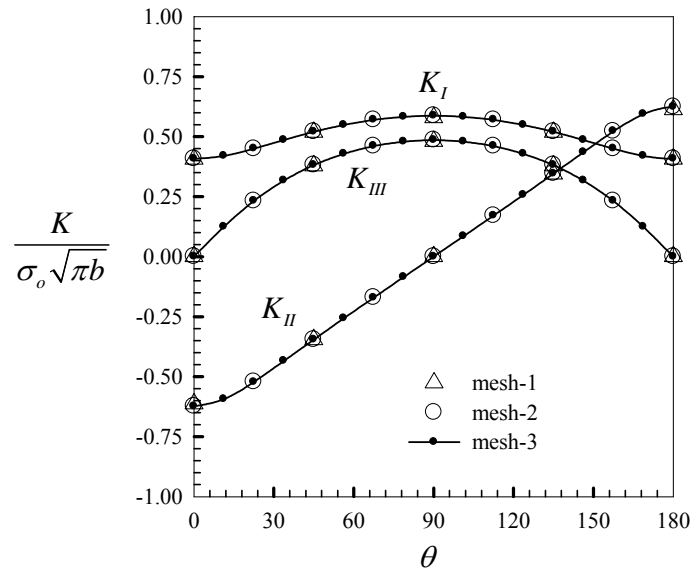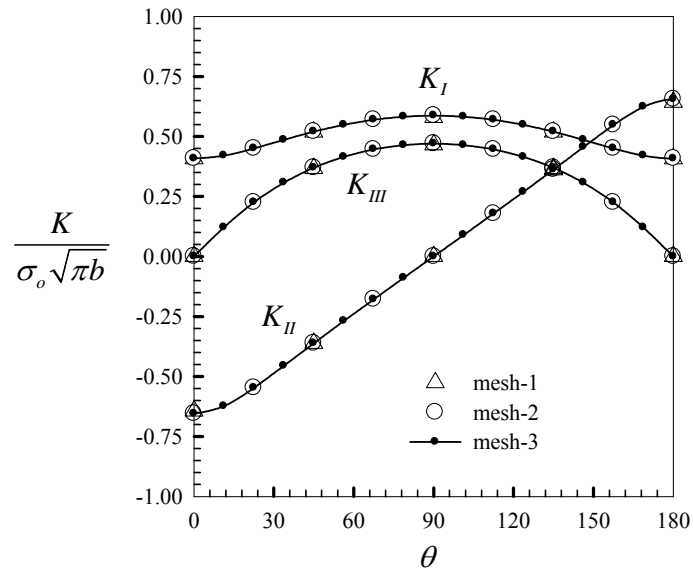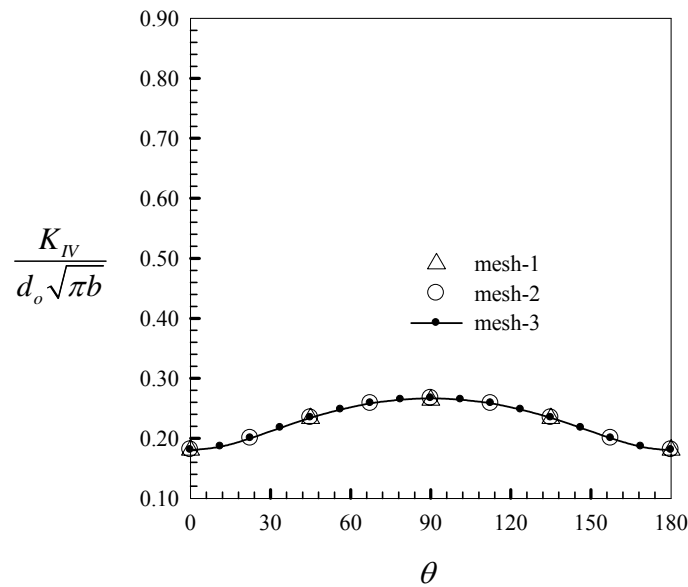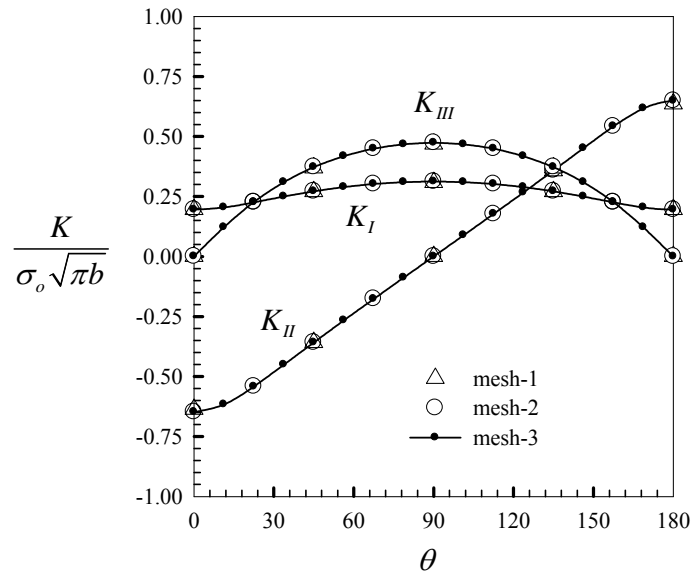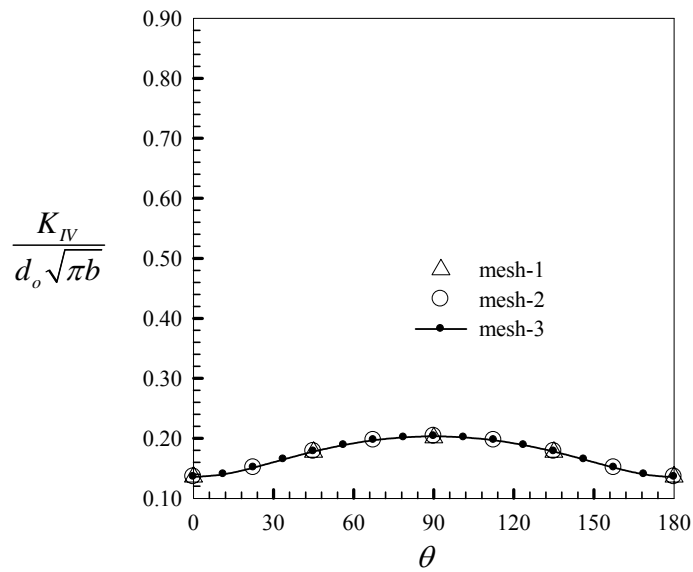
(a)
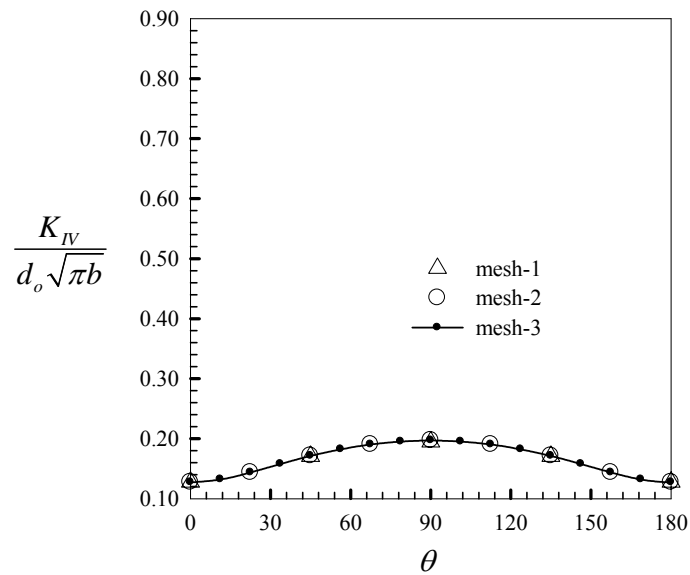
(b)

Fig. 4.22. Normalized intensity factors for an inclined elliptical crack in an unbounded domain subjected to uniform tensile stress $\sigma_o = 5\,\text{MPa}$ and constant electric field $E_0 = 0.5\,\text{MV/m}$ for permeable crack: (a) stress intensity factors $\{K_I,\ K_{II},\ K_{III}\}$ and (b) electric intensity factor $\{K_{IV}\}$.

(a)

(b)

Fig. 4.23. Normalized intensity factors for an inclined elliptical crack in an unbounded domain subjected to uniform tensile stress $\sigma_o = 5\,\mathrm{MPa}$ and constant electric field $E_0 = 0.5\,\mathrm{MV/m}$ for semi-permeable crack: (a) stress intensity factors $\{K_I,\ K_{II},\ K_{III}\}$ and (b) electric intensity factor $\{K_{IV}\}$.

(a)

(b)

Fig. 4.24. Normalized intensity factors for an inclined elliptical crack in an unbounded domain subjected to uniform tensile stress $\sigma_o = 5\,\text{MPa}$ and constant electric field $E_0 = 0.5\,\text{MV/m}$ for Landis-type crack: (a) stress intensity factors $\{K_I,\ K_{II},\ K_{III}\}$ and (b) electric intensity factor $\{K_{IV}\}$.
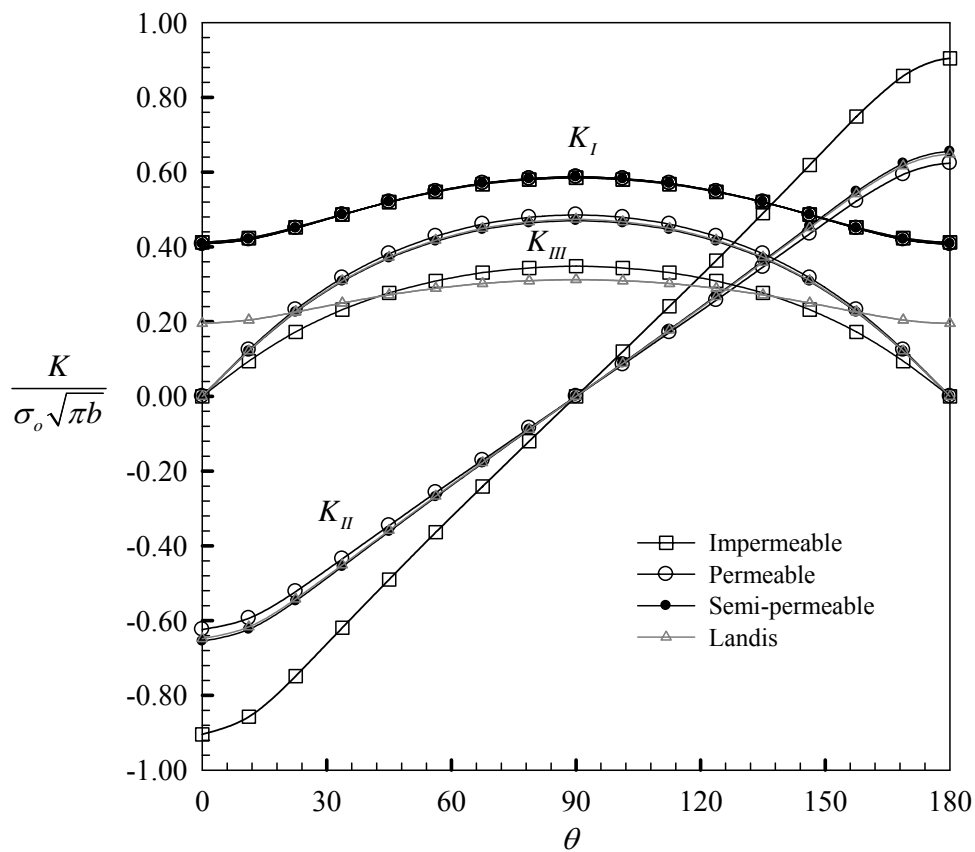
Fig. 4.25. Normalized stress intensity factors $\{K_I, K_{II}, K_{III}\}$ obtained from the mesh-3 for an inclined elliptical crack in an unbounded domain subjected to uniform tensile stress $\sigma_o = 5\,\text{MPa}$ and constant electric field $E_0 = 0.5\ \text{MV/m}$ for four types of cracks.
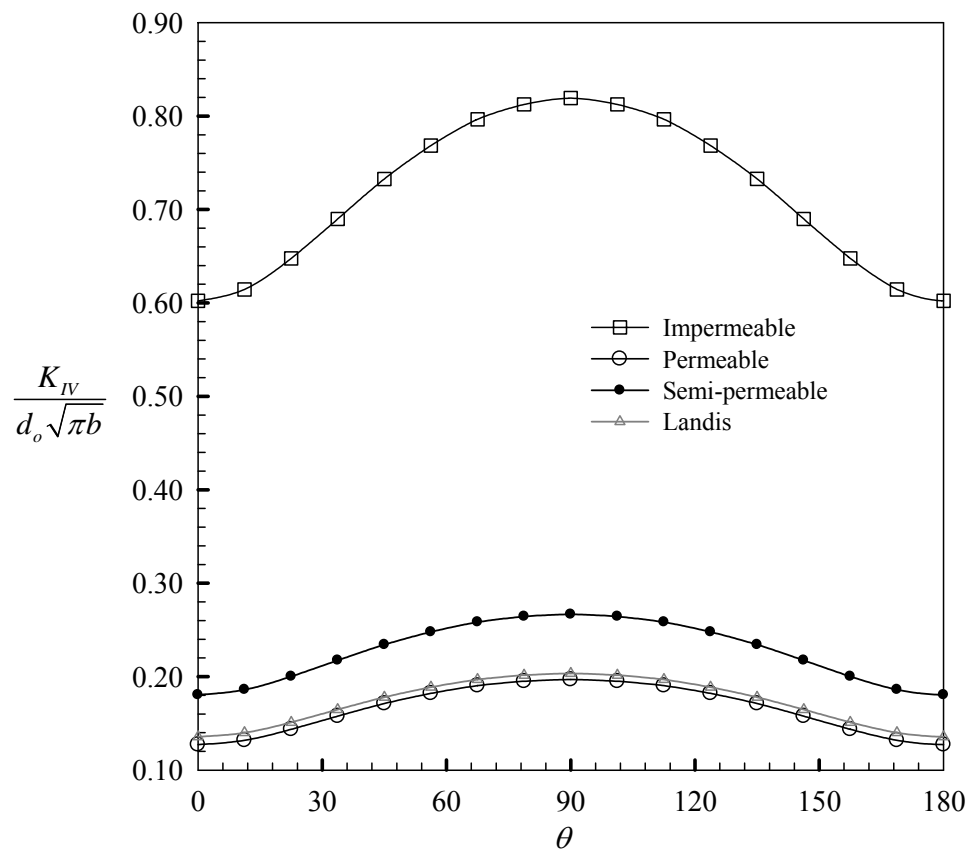
Fig. 4.26. Normalized electric intensity factor K_{IV} obtained from the mesh-3 for an inclined elliptical crack in an unbounded domain subjected to uniform tensile stress $\sigma_o = 5\,\text{MPa}$ and constant electric field $E_0 = 0.5\,\text{MV/m}$ for four types of cracks.

4.2.3 Penny-shaped crack in solid cylinder

Consider a solid cylinder of radius R and length $2L$ containing a penny-shaped crack of radius a as shown in Fig. 4.27(a). The cylinder is made of PZT-5H with the axis of material symmetry directing along the axis of the cylinder (x_3-axis). The uniform normal traction σ_o and uniform surface electric charge d_o are applied to its top and bottom surfaces with the loading ratio $(\sigma_o / E_{3333})/(d_o / E_{3343}) = 0.20$ whereas the remaining boundary including the crack surface is free of traction and surface electric charge. The problem geometry is defined as $a/R = 0.5$ and $L/R = 4$, and three meshes adopted in the analysis shown in Fig. 4.27(b).
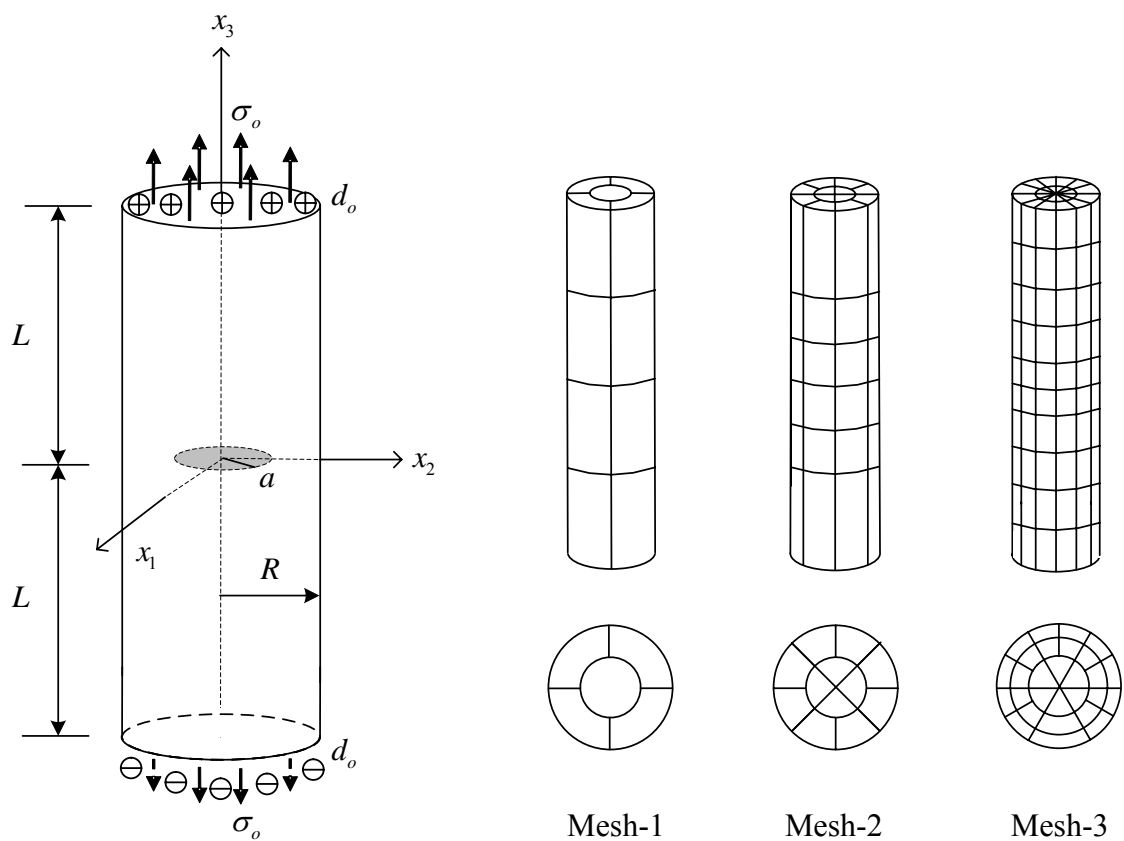

Fig. 4.27. (a) A penny-shaped crack embedded in a solid cylinder subjected to uniform normal traction σ_o and uniform surface electric charge d_o and (b) three meshes adopted in the analysis

Since the analytical solution or the reference numerical solution for this particular problem is not available in the literature, the mode-I stress intensity factors (K_I^{ref}) and the electric intensity factors (K_{IV}^{ref}) obtained from the mesh-3 for four different types of crack assumptions (given in Table 4.10) are used as the benchmark solutions. The normalized intensity factors obtained from all three meshes are then reported in Table 4.11 and 4.12 in order to investigate the convergence behavior of the numerical solutions. It is found that results obtained from the mesh-1 and the mesh-2, when compared to the reference solution obtained from the mesh-3, lead to the relative discrepancy less than 0.80% and 0.25%, respectively.

Table 4.10 The reference stress intensity factors (K_I^{ref}) and electric intensity factor (K_{IV}^{ref}) obtained from the mesh-3 for four different types of cracks.

Type of cracks	$K_I^{ref} / \sqrt{\pi a}\sigma_o$	$K_{IV}^{ref} / \sqrt{\pi a}d_o$
Impermeable crack	0.6860	0.6740
Permeable crack	0.6861	0.1915
Semi-permeable crack	0.6861	0.2148
Landis-type crack	0.6674	0.2092

Table 4.11 Normalized intensity factors for solid cylinder containing penny-shaped crack subjected to uniform normal traction σ_o and uniform surface electric charge d_o for impermeable and permeable cracks

Mesh	Impermeable crack		Permeable crack	
	K_I / K_I^{ref}	K_{IV} / K_{IV}^{ref}	K_I / K_I^{ref}	K_{IV} / K_{IV}^{ref}
1	0.9921	0.9926	0.9921	0.9921
2	0.9979	0.9979	0.9979	0.9979
3	1.0000	1.0000	1.0000	1.0000

Table 4.12 Normalized intensity factors for solid cylinder containing penny-shaped crack subjected to uniform normal traction σ_o and uniform surface electric charge d_o for semi-permeable and Landis-type cracks

Mesh	Semi-permeable crack		Landis-type crack	
	$\kappa_c = 8.85 x 10^{-12} \ C/(Vm)$		$\kappa_c = 8.85 x 10^{-12} \ C/(Vm)$	
	K_I / K_I^{ref}	K_{IV} / K_{IV}^{ref}	K_I / K_I^{ref}	K_{IV} / K_{IV}^{ref}
1	0.9921	0.9921	0.9921	0.9921
2	0.9979	0.9979	0.9979	0.9979
3	1.0000	1.0000	1.0000	1.0000

4.2.4 Circumferential crack in solid cylinder

Consider next a solid cylinder of radius R and length L that contains a circumferential crack of depth d at its half-length as shown schematically in Fig. 4.28. The cylinder is made of a transversely isotropic, piezoelectric material named PZT-5H with the axis of material symmetry directing along the axis of the cylinder (x_3-axis). The cylinder is subjected to uniform normal traction σ_o and uniform surface electric charge d_o at its top and bottom surfaces whereas the remaining boundary including the crack surface is free of traction and surface electric charge, and only the impermeable boundary condition at the crack surface is treated.

As be evident from the symmetry of geometry and boundary conditions, only the mode-I stress intensity factor and the electric intensity factor are non-zero and they are constant along the crack front. In the analysis, three meshes shown in Fig. 4.29 are adopted for $L/R = 4$ and $R/d = 2$, and the computed intensity factors are reported in Table 4.13 for the loading ratio $(\sigma_o / E_{3333})/(d_o / E_{3343})$ = 0.20. Results obtained from all three meshes are normalized by the (converged) reference solution obtained from the mesh-3. As be apparent from presented results, the intensity factors computed from the three meshes are in very good agreement and the maximum discrepancy between results from the coarse mesh and fine mesh is less than 1%. It is crucial to emphasize that while the mesh-1 is extremely coarse with only four crack-

tip elements being employed along the crack front, it yields results that are almost indistinguishable from the converged solution.
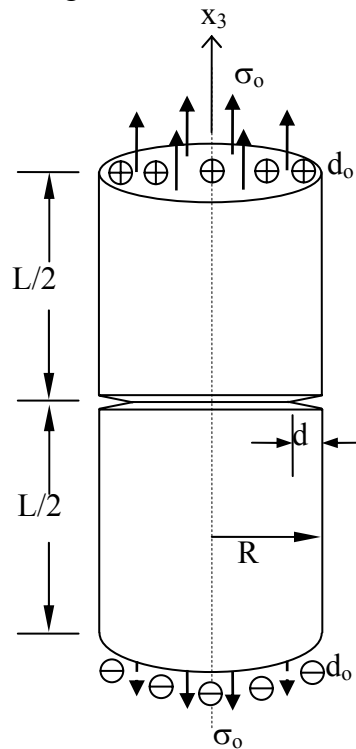

Fig. 4.28. Schematic of solid cylinder containing circumferential crack under uniform normal traction and uniform surface electric charge
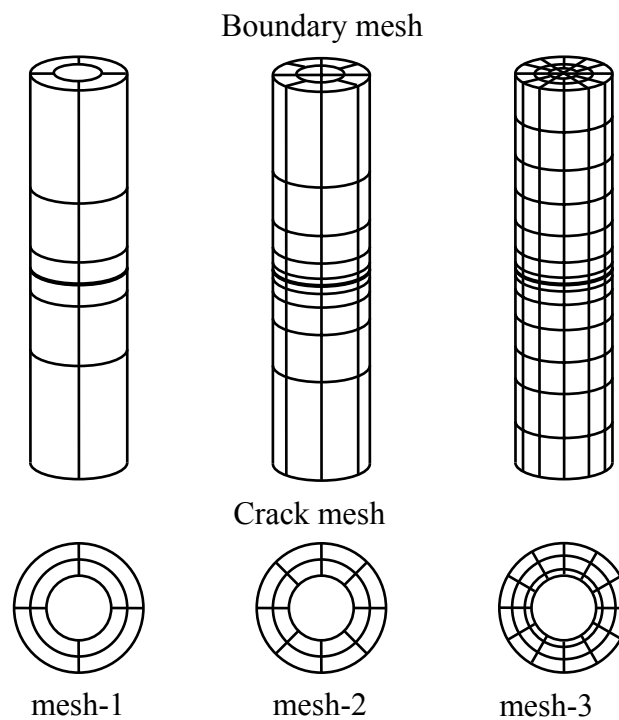

Fig. 4.29. Three meshes adopted in the analysis

Table 4.13 Normalized intensity factors for solid cylinder containing circumferential crack under impermeable boundary condition. The computed intensity factors are normalized by solutions from mesh-3 where $K_I^{ref} = 1.9430\sqrt{\pi d}\sigma_o$ and $K_{IV}^{ref} = 1.9197\sqrt{\pi d}d_o$.

Mesh	K_I/K_I^{ref}	K_{IV}/K_{IV}^{ref}
1	0.9914	0.9909
2	0.9966	0.9961
3	1.0000	1.0000

4.2.5 Edge cracked bar

Consider next a rectangular bar, which is made of PZT-5H, containing a through-the-thickness edge crack as shown in Fig. 4.30; the chosen body and crack configuration in this example are the same as that considered by Rungamornrat and Mear (2008b). The bar is subjected to the uniform normal traction σ_o and uniform surface electric charge d_o at its top and bottom surfaces whereas the rest of the boundary including the crack surface is free of the generalized traction. In the analysis, we take $w/t = 0.75$, $h/t = 0.875$, $a/t = 0.5$ and the loading ratio $(\sigma_o/E_{3333})/(d_o/E_{3343}) = 0.20$ and the crack surface is electrically impermeable. Three meshes similar to those used by Rungamornrat and Mear (2008b) are adopted as shown in Fig. 4.31.

The computed mode-I stress intensity factor (K_I) and electric intensity factor (K_{IV}) are reported, as a function of arc length s (measured from the center of the crack front), in Figs. 4.32 and 4.33, respectively. It is evident that numerical results obtained from the three meshes are in good agreement except in the local region near the surface-breaking points where results exhibit slight dependence on the level of refinement. In particular, the coarsest mesh (i.e. mesh-1) utilizes only three elements along the crack front but it can still capture the intensity factors in the central region of the crack front of comparable quality to that obtained from the finest mesh (i.e. mesh-3). The weak dependence on mesh refinement has been observed in all

experiments performed. This attractive feature results primarily from the use of special crack-tip elements along the crack front.
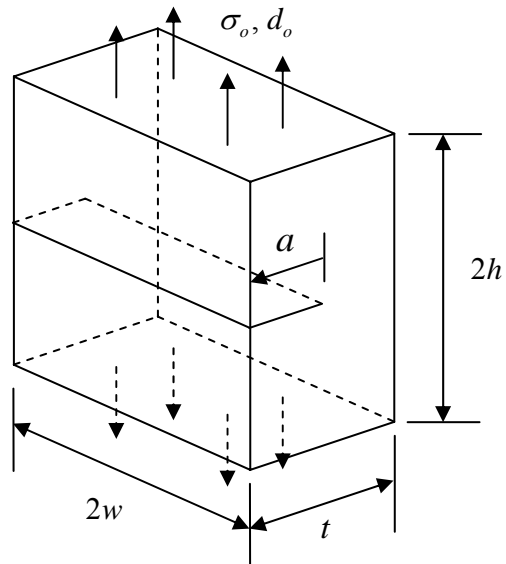

Fig. 4.30. Edge cracked rectangular bar subjected to uniform normal traction σ_o and uniform surface electric charge d_o at its top and bottom surfaces
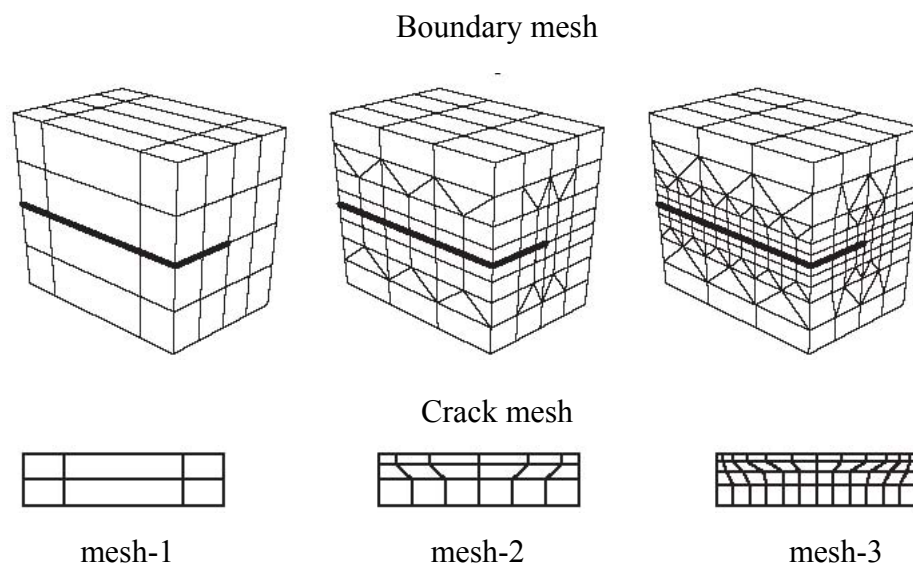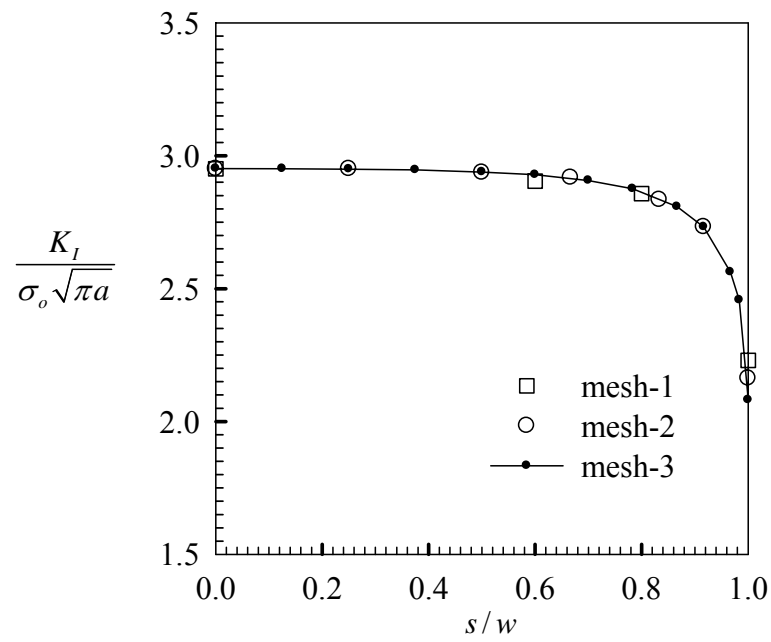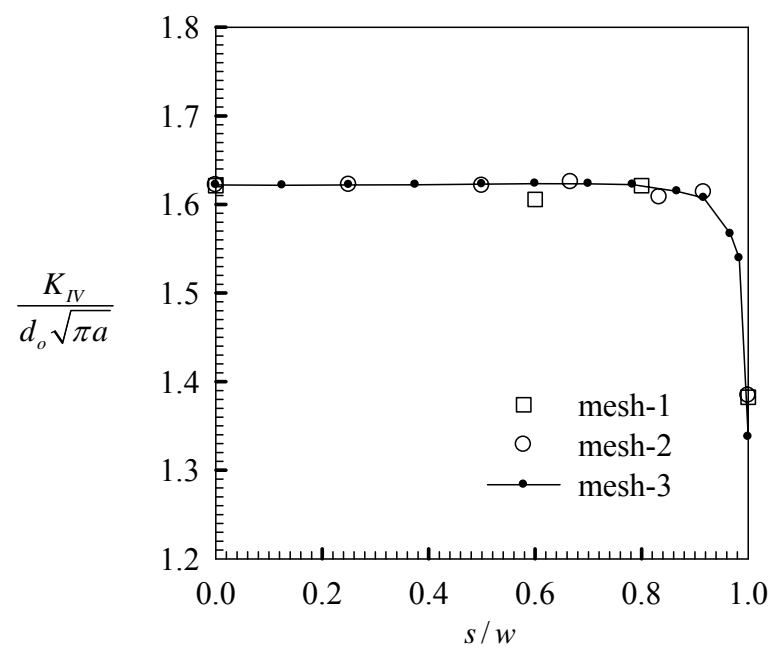

Fig. 4.31. Three meshes adopted for analysis of edge cracked rectangular bar where crack mesh is shown below the boundary mesh

$$\frac{K_I}{\sigma_o\sqrt{\pi a}}$$

□ mesh-1
○ mesh-2
—●— mesh-3

s/w

(a)

$$\frac{K_{IV}}{d_o\sqrt{\pi a}}$$

□ mesh-1
○ mesh-2
—●— mesh-3

s/w

(b)

Fig. 4.32. Normalized intensity factors for edge cracked rectangular bar subjected to uniform normal traction and uniform surface electric charge (a) mode-I stress intensity factor and (b) mode-IV electric intensity factor.

4.3 Influence of electrical boundary conditions on intensity factors

As be known, there are several types of electrical boundary conditions adopted at the crack surfaces, i.e., permeable, impermeable, semi-permeable and Landis-type cracks. A question arises as which one is physically reasonable and more realistic. Because of this, it motivates the present study to explore the influence of electrical boundary conditions on the intensity factors of the cracked piezoelectric medium. Numerical experiments of isolated planar and nonplanar cracks in an unbounded domain and the piezoelectric finite cracked bodies are investigated.

4.3.1 Penny-shaped crack in unbounded domain

Consider a penny-shaped crack of radius a embedded in a piezoelectric infinite medium that is made of PZT-4 similar to the previous problem in subsection 4.1.1. The medium is subjected to the remote uniform tensile stress σ_o, which is varied from 0 to 100 MPa, and the fixed electric field E_o equal to 0.5 MV/m. The finest mesh (i.e. mesh-3) shown in Fig.4.2 is used in the analysis. Numerical results for the mode-I stress intensity factor and the electric intensity factor are properly normalized and reported in Fig. 4.33 and Fig. 4.34 along with the analytical solution (Chen et al. 2000; Li and Lee 2004; Li et al. 2011).

It is evident again that numerical results are nearly identical to the analytical solutions for all four types of crack assumptions. Moreover, it can be concluded from Fig. 4.33 that the mode-I stress intensity factors (K_I) for permeable, impermeable and semi-permeable cases are identical for the entire range of σ_o and such results are in agreement with the work of Li and Lee (2004) and Chiang and Weng (2007) that conclude that the mode-I stress intensity factors of those three types of cracks depend only on the mechanical loading but are independent of the electric loading. In addition, it can be inferred from Fig. 4.33 that results obtained for the Landis-type crack is less than those obtained from the other three crack models when the mechanical stress is small. However, when the mechanical stress increases, the mode-I stress intensity factor obtained from the Landis-type assumption and all other three crack models are nearly identical.

In contrast with K_I, the electric intensity factor (K_{IV}) exhibits strong dependence on the electrical boundary conditions. Fig. 4.34 indicates that the electric intensity factor for both impermeable and permeable cases serve, respectively, as the upper and lower bounds of results for semi-permeable and Landis-type cases except for very small σ_o where K_{IV} for the Landis-type crack is slightly lower than that for the permeable case. Moreover, K_{IV} for semi-permeable and Landis-type cracks are nearly indistinguishable for almost the entire range of σ_o; slight difference is observed for small value of σ_o.
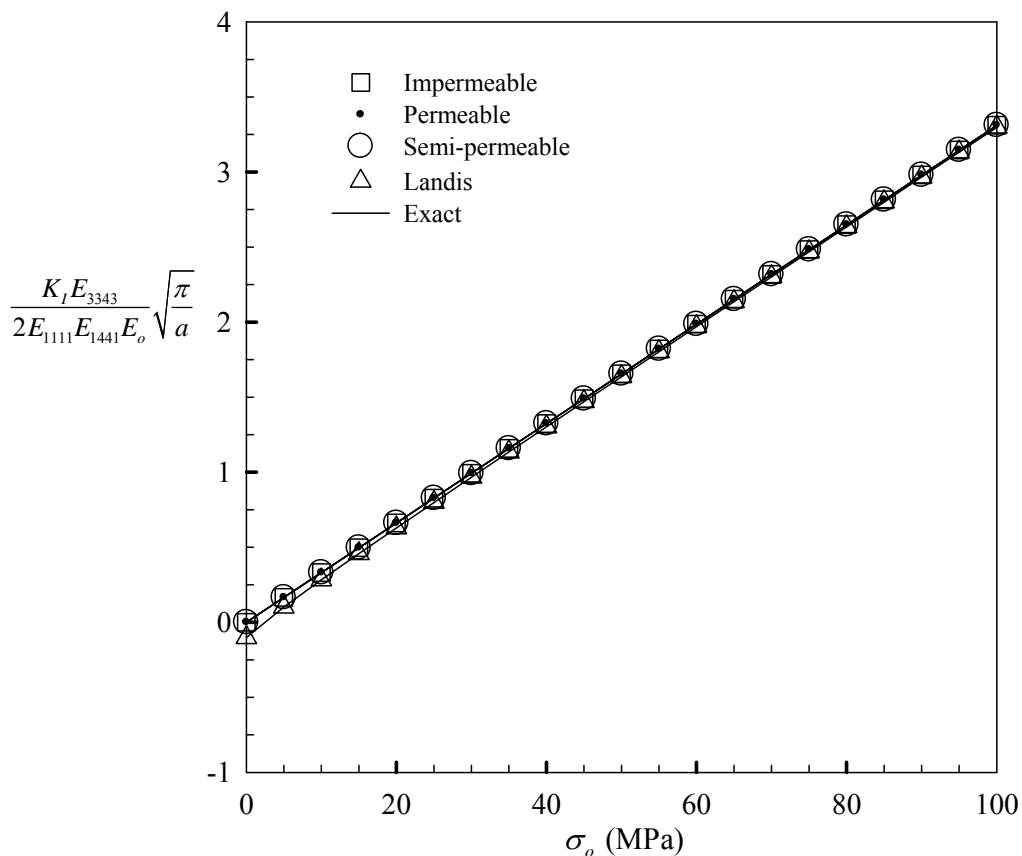
Fig. 4.33. Normalized K_I for a penny-shaped crack in a piezoelectric infinite medium subjected to remote uniform tensile stress σ_o and constant electric field E_o under four types of crack assumptions
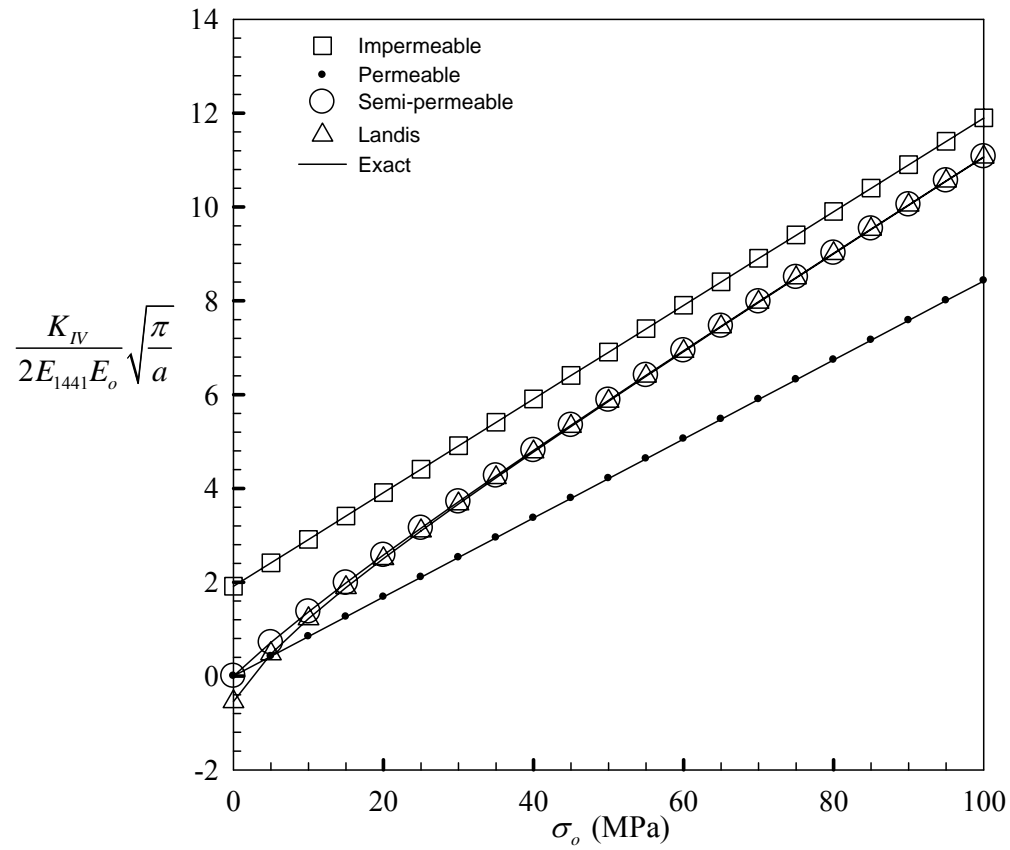
Fig. 4.34. Normalized K_{IV} for a penny-shaped crack in a piezoelectric infinite medium subjected to remote uniform tensile stress σ_o and constant electric field E_o under four types of crack assumptions

4.3.2 Elliptical crack in an unbound domain

Consider an elliptical crack embedded in a transversely isotropic piezoelectric infinite medium as shown schematically in Fig. 4.35 where a and b represent the major and minor semi-axes of the ellipse, respectively. The medium is assumed to be PZT-4 and the crack surface is assumed to lie within the $x_1 - x_2$ plane and perpendicular to the axis of material symmetry and poling direction. A convergence study of numerical solutions is performed first by using a series of meshes for the crack surface as shown in Fig. 4.36; in particular, the number of elements for mesh-1, mesh-2 and mesh-3 are 8, 24 and 64 elements, respectively. The aspect ratio of the elliptical crack is chosen to be $a/b = 2$ and the unbounded piezoelectric medium is loaded by the uniform remote tensile stress $\sigma_o = 5$ MPa and uniform remote electric field $E_o = 0.5$ MV/m along the polar direction. Normalized intensity factors K_I and K_{IV} for four types of crack assumptions computed from the three meshes are reported, as a function of position along the crack front, in Figs. 4.37-4.40. It is found that numerical results obtained from all three meshes are in good agreement. More specifically, numerical results obtained from the mesh-1 and the mesh-3 are slightly different while results obtained from the intermediate and finest mesh are almost indistinguishable for all four types of crack assumptions. Moreover, it can be inferred from Fig. 4.41(a) that the mode-I stress intensity factor of impermeable, permeable and semi-permeable cracks are nearly identical and greater than that of the Landis-type crack for the entire crack front.

In contrast with the mode-I stress intensity factor, the electric intensity factors under four types of electrical boundary conditions are completely different. Fig. 4.41(b) indicates that the electric intensity factors of impermeable and permeable cracks are, respectively, the upper and lower bounds of results of semi-permeable and Landis-type cracks. In addition, the electric intensity factor of the semi-permeable crack is greater than that of the Landis-type crack.
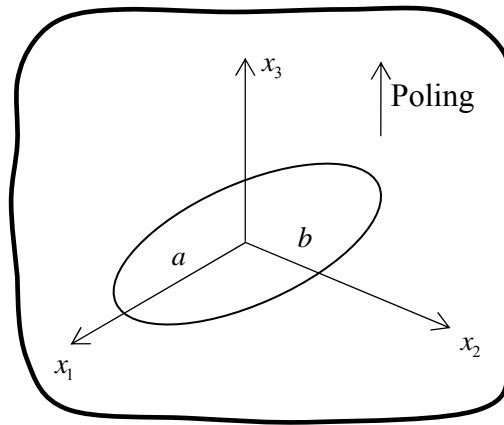
Fig. 4.35. Schematic of an elliptical crack in a piezoelectric infinite medium
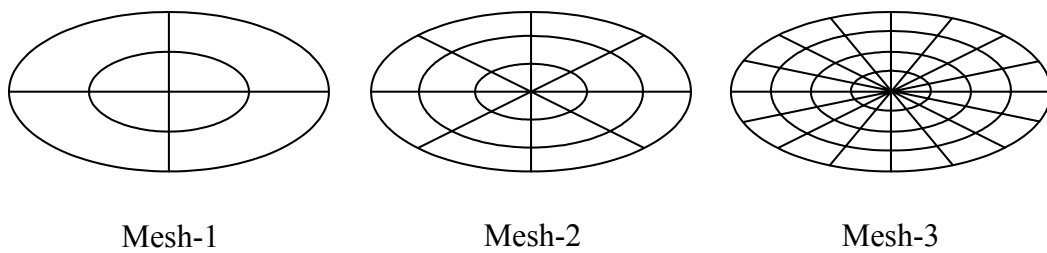

| Mesh-1 | Mesh-2 | Mesh-3 |

Fig. 4.36. A series of mesh adopted in the analysis of an elliptical crack in a piezoelectric infinite medium

$$\frac{K_I}{2\sigma_o}\sqrt{\frac{\pi}{b}}$$

△ mesh-1
○ mesh-2
• mesh-3
—— exact

θ

(a)

$$\frac{K_{IV}E_{1111}}{2E_{3343}\sigma_o}\sqrt{\frac{\pi}{b}}$$

△ mesh-1
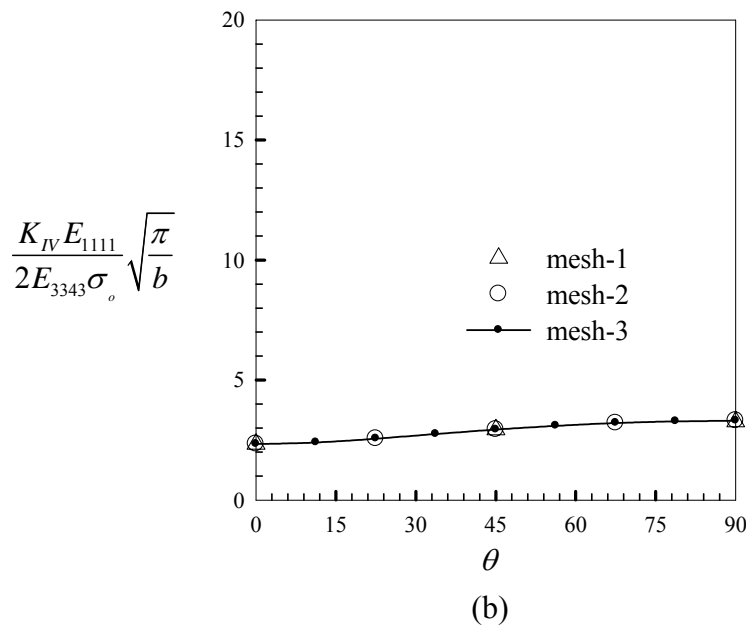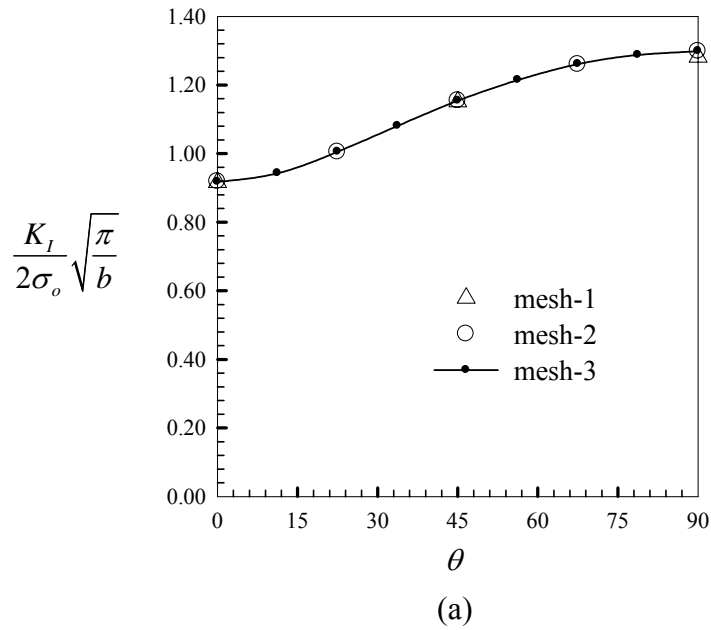○ mesh-2
• mesh-3
—— exact

θ

(b)
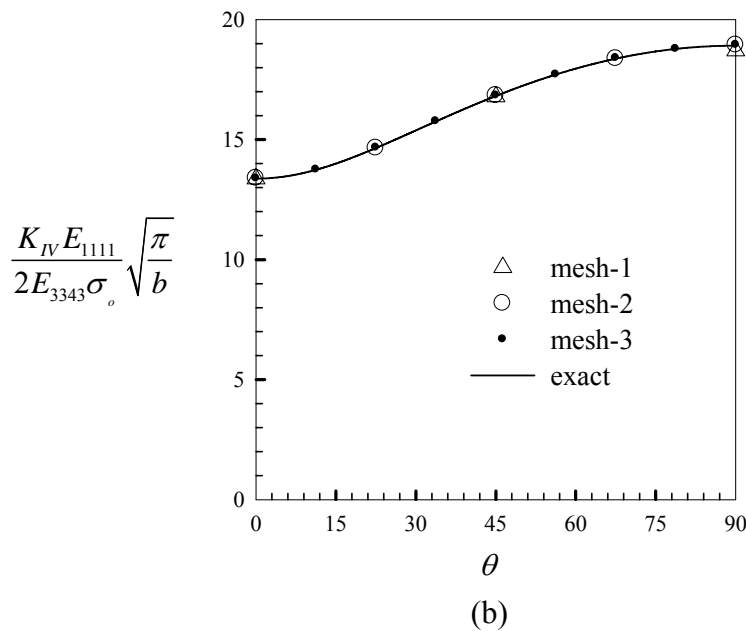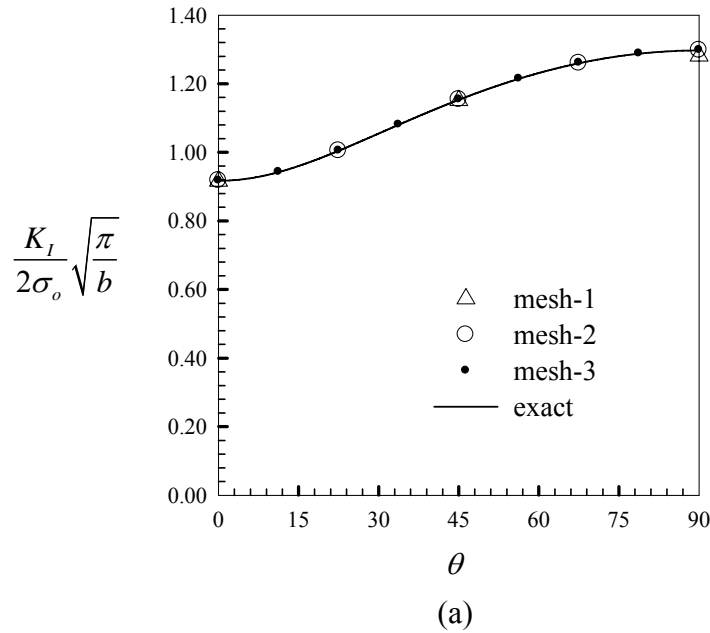
Fig. 4.37. (a) Normalized mode-I stress intensity factor and (b) electric intensity factor for elliptical crack with aspect ratio $a/b = 2$ in a piezoelectric infinite medium subjected to uniform remote tensile stress $\sigma_o = 5\,\text{MPa}$ and constant electric field $E_o = 0.5\,\text{MV/m}$ for impermeable crack.
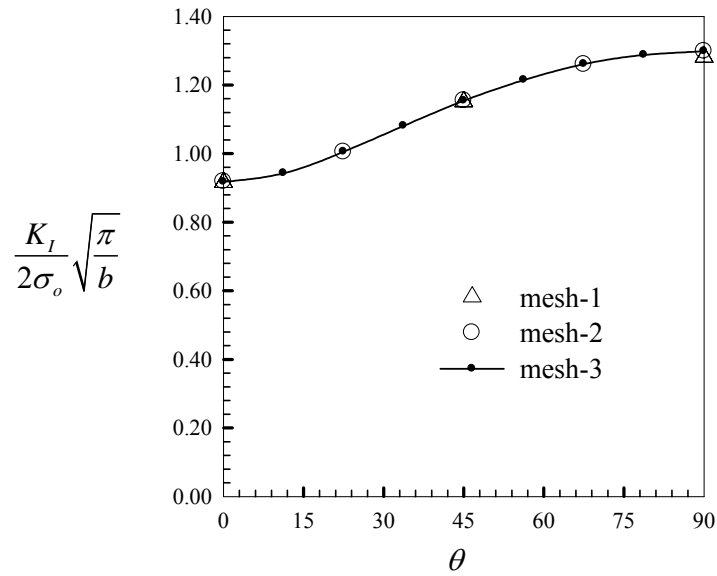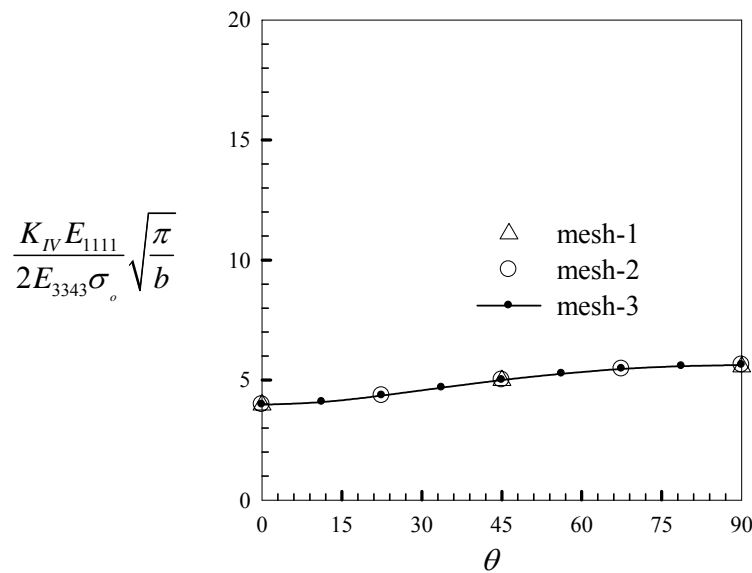
(a)

(b)

Fig. 4.38. (a) Normalized mode-I stress intensity factor and (b) electric intensity factor for elliptical crack with aspect ratio $a/b = 2$ in a piezoelectric infinite medium subjected to uniform remote tensile stress $\sigma_o = 5\,\text{MPa}$ and constant electric field $E_o = 0.5\,\text{MV/m}$ for permeable crack.

$$\frac{K_I}{2\sigma_o}\sqrt{\frac{\pi}{b}}$$

mesh-1
mesh-2
mesh-3

θ

(a)

$$\frac{K_{IV}E_{1111}}{2E_{3343}\sigma_o}\sqrt{\frac{\pi}{b}}$$

mesh-1
mesh-2
mesh-3

θ

(b)

Fig. 4.39. (a) Normalized mode-I stress intensity factor and (b) electric intensity factor for elliptical crack with aspect ratio $a/b = 2$ in a piezoelectric infinite medium subjected to uniform remote tensile stress $\sigma_o = 5\,\mathrm{MPa}$ and constant electric field $E_o = 0.5$ MV/m for semi-permeable crack.

$$\frac{K_I}{2\sigma_o}\sqrt{\frac{\pi}{b}}$$

△ mesh-1

○ mesh-2

• mesh-3

(a)

$$\frac{K_{IV}E_{1111}}{2E_{3343}\sigma_o}\sqrt{\frac{\pi}{b}}$$
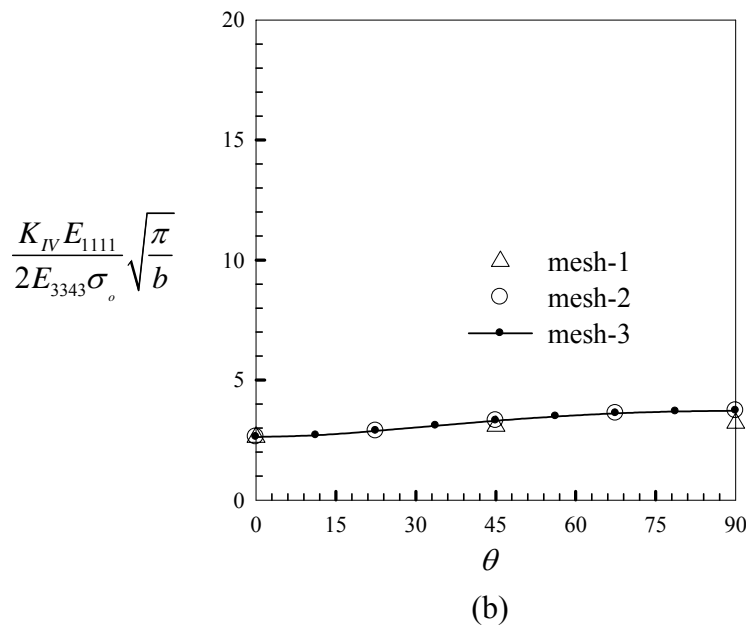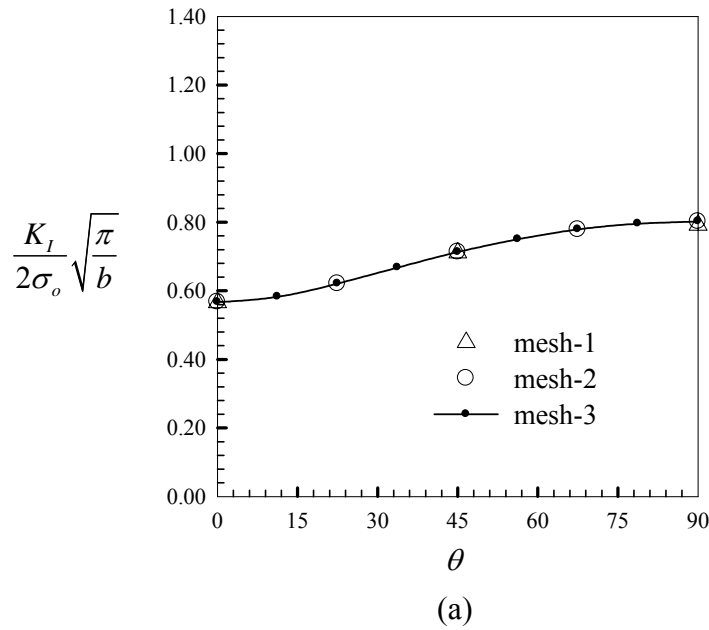
△ mesh-1

○ mesh-2

• mesh-3

(b)

Fig. 4.40. (a) Normalized mode-I stress intensity factor and (b) electric intensity factor for elliptical crack with aspect ratio $a/b = 2$ in a piezoelectric infinite medium subjected to uniform remote tensile stress $\sigma_o = 5\,\text{MPa}$ and constant electric field $E_o = 0.5\,\text{MV/m}$ for Landis-type crack.

$$\frac{K_I}{2\sigma_o}\sqrt{\frac{\pi}{b}}$$

- Impermeable
- Permeable
- Semi-permeable
- Landis

(a)

$$\frac{K_{IV}E_{1111}}{2E_{3343}\sigma_o}\sqrt{\frac{\pi}{b}}$$

- Impermeable
- Permeable
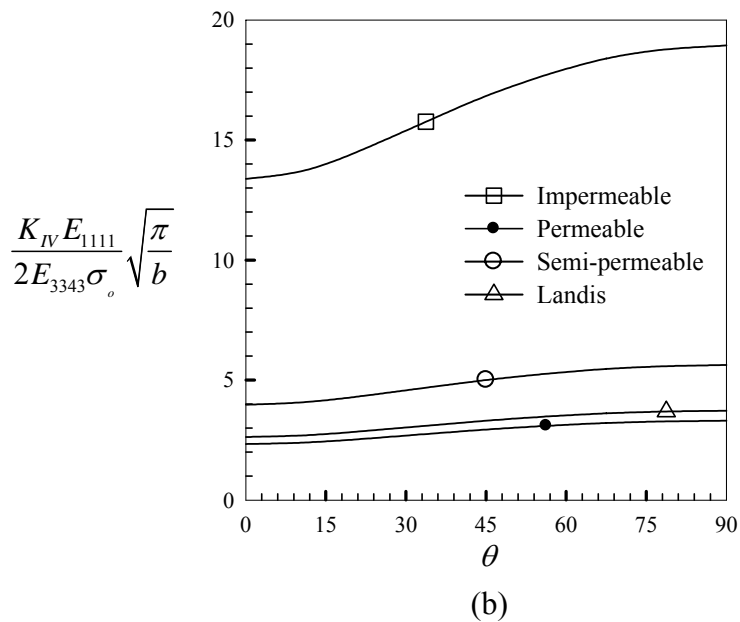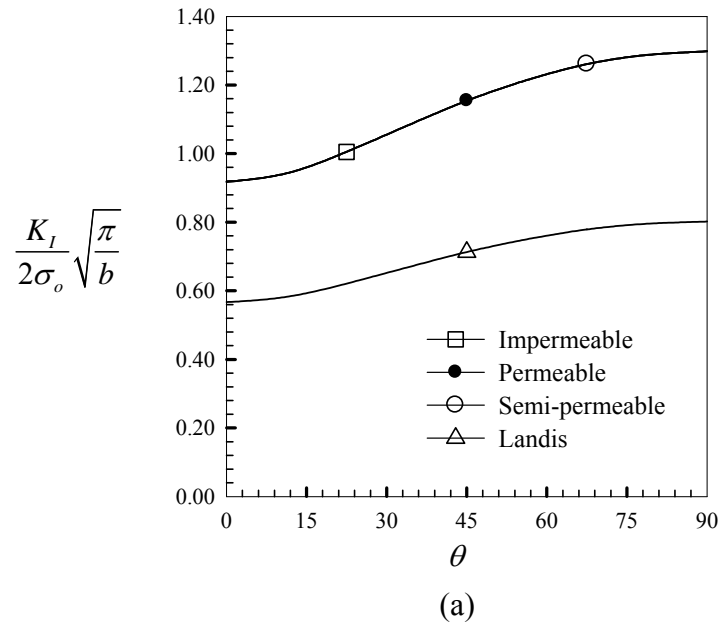- Semi-permeable
- Landis

(b)

Fig. 4.41. (a) Normalized mode-I stress intensity factor and (b) electric intensity factor for elliptical crack with aspect ratio $a/b = 2$ in a piezoelectric infinite medium subjected to uniform remote tensile stress $\sigma_o = 5\,\text{MPa}$ and constant electric field $E_o = 0.5\,\text{MV/m}$ for four types of cracks.

Furthermore, in order to study the influence of the aspect ratio a/b upon the stress and electric intensity factors under four different types of crack assumptions, three values of a/b, i.e. $a/b \in \{1, 2, 3\}$, are considered. Moreover, the applied uniform remote tensile stress is varied from 0 to 100 MPa whereas the electric field is fixed at 0.5 MV/m. Numerical solutions obtained from the mesh-3 are reported in Figs. 4.42-4.44. It can be inferred from Figs. 4.42(a) and 4.42(b) that increasing the aspect ratio a/b tends to reduce both the mode-I stress intensity factor and electric intensity factor at $\theta = 0^o$ for all four types of crack assumptions. However, at $\theta = 45^o$ and $\theta = 90^o$, K_I and K_{IV} increase as the a/b ratio increases as shown in Figs. 4.43 and 4.44, respectively. Moreover, it is also found that the maximum K_I and K_{IV} occur at $\theta = 90^o$ while the minimum K_I and K_{IV} occur at $\theta = 0^o$ for $a/b \in \{2, 3\}$. For the influence of electrical boundary conditions upon the intensity factors at $\theta \in \{0^o, 45^o, 90^o\}$ when the aspect ratio a/b is varied, it is found that the distribution of K_I and K_{IV} of an elliptical cracks ($a/b = 2, 3$) are similar to the distribution of K_I and K_{IV} for the penny-shaped crack ($a/b = 1$). More specifically, K_I of the permeable, impermeable and semi-permeable cracks are nearly identical for the entire range of the applied mechanical stress while K_I of the Landis-type crack is less than of the other three crack models when the applied remote mechanical stress is relatively small. However, when the applied uniform remote mechanical stress increases, K_I of the Landis-type crack and the other three crack models are nearly identical. In contrast with K_I, the electric intensity factors (K_{IV}) of the impermeable crack is the upper bound for the entire range of mechanical stress. While K_{IV} of the permeable crack is the lower bound when the applied mechanical stress is relatively height. However, K_{IV} of the Landis-type crack becomes the lower bound in stead of the permeable case when the applied mechanical stress is very small and K_{IV} of the semi-permeable and Landis-type cracks are nearly identical when the mechanical stress becomes larger.
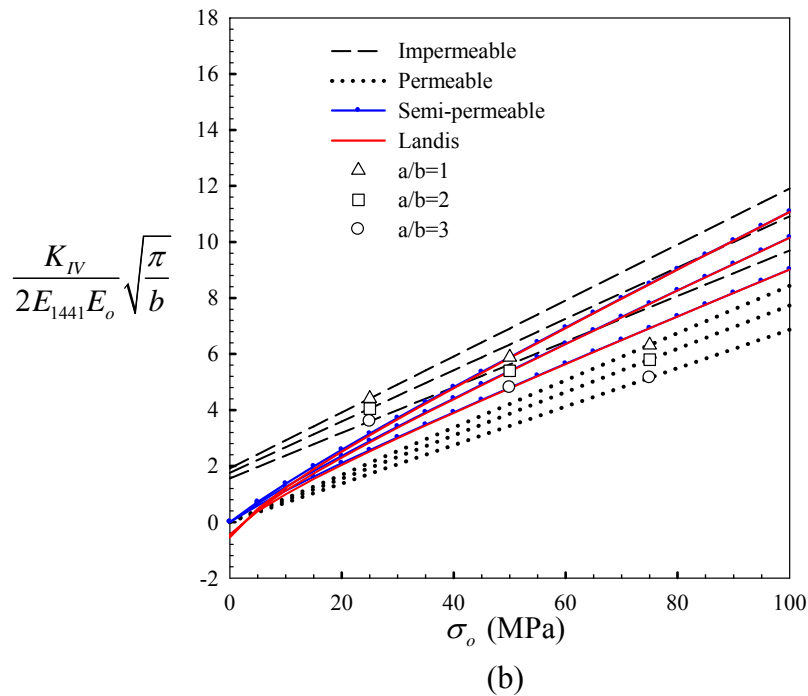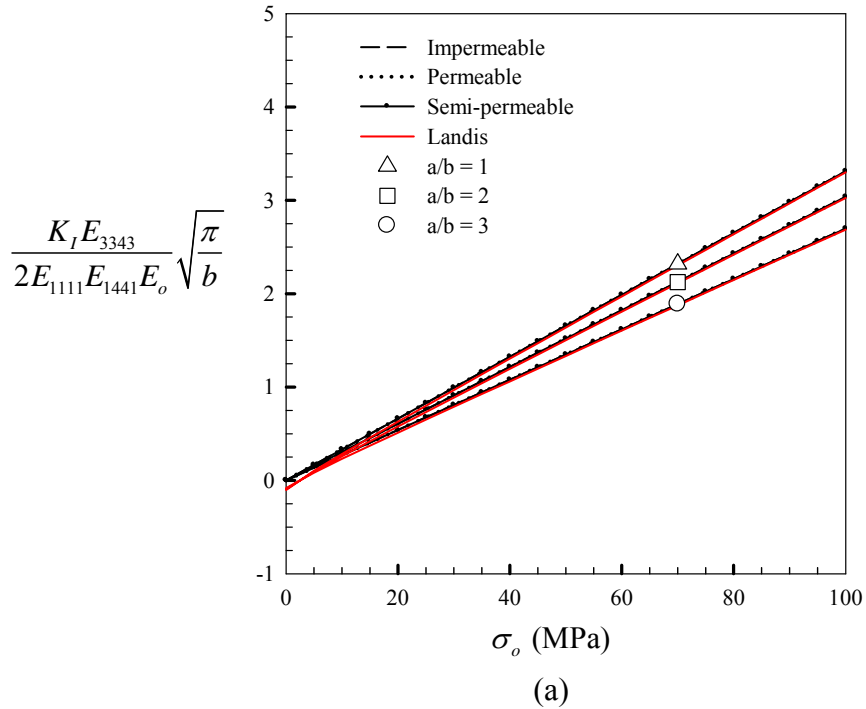
(a)

(b)

Fig. 4.42. Normalized intensity factors at $\theta = 0^o$ for an elliptical crack in an infinite medium under four types of crack assumptions (a) stress intensity factor K_I and (b) electric intensity factor K_{IV}

Fig. 4.43. Normalized intensity factors at $\theta = 45^o$ for an elliptical crack in an infinite medium under four types of crack assumptions (a) stress intensity factor K_I and (b) electric intensity factor K_{IV}
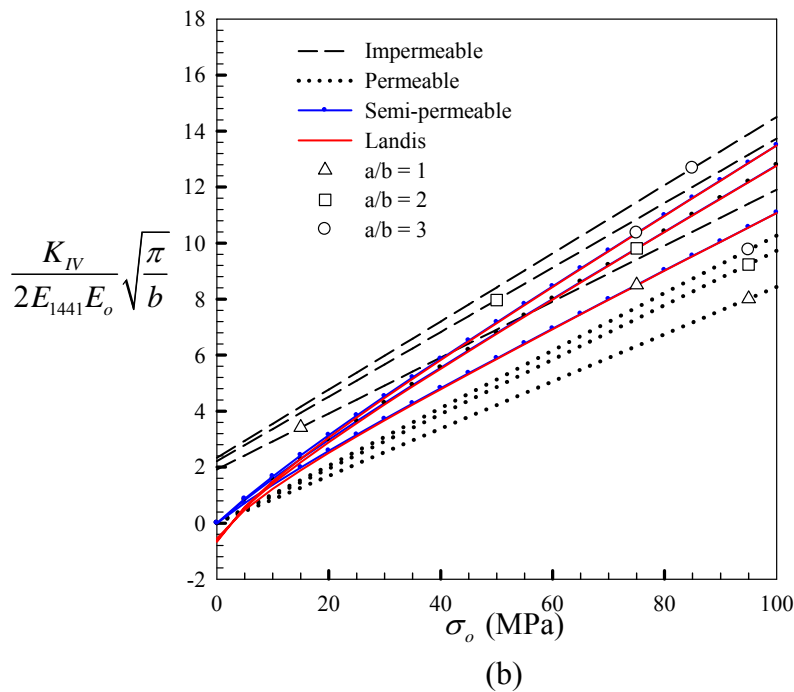
$$\frac{K_I E_{3343}}{2E_{1111}E_{1441}E_o}\sqrt{\frac{\pi}{b}}$$

σ_o (MPa)

(a)

$$\frac{K_{IV}}{2E_{1441}E_o}\sqrt{\frac{\pi}{b}}$$

σ_o (MPa)

(b)

Fig. 4.44. Normalized intensity factors at $\theta = 90^o$ for an elliptical crack in an infinite medium under four types of crack assumptions (a) stress intensity factor K_I and (b) electric intensity factor K_{IV}
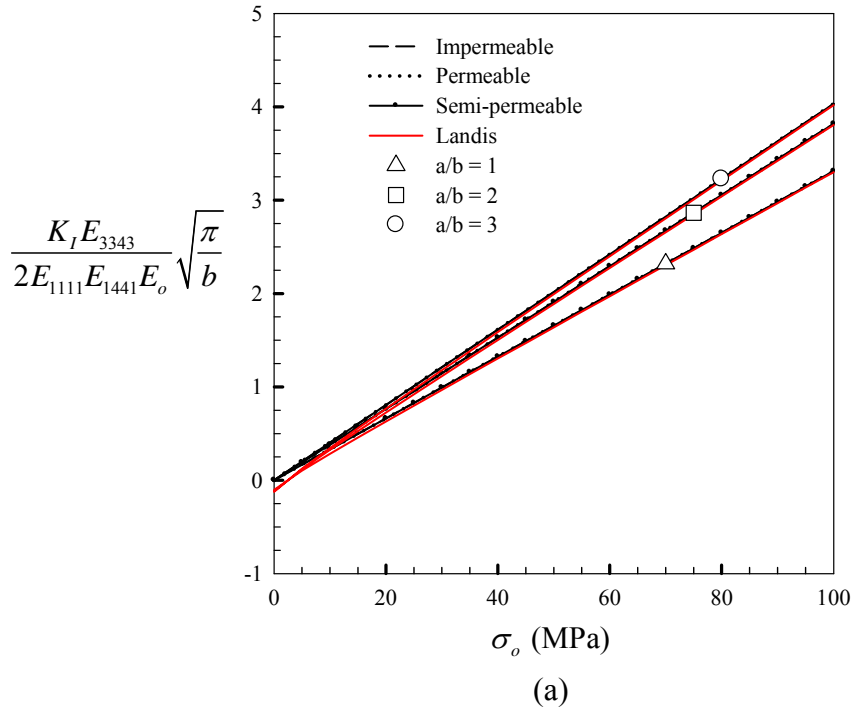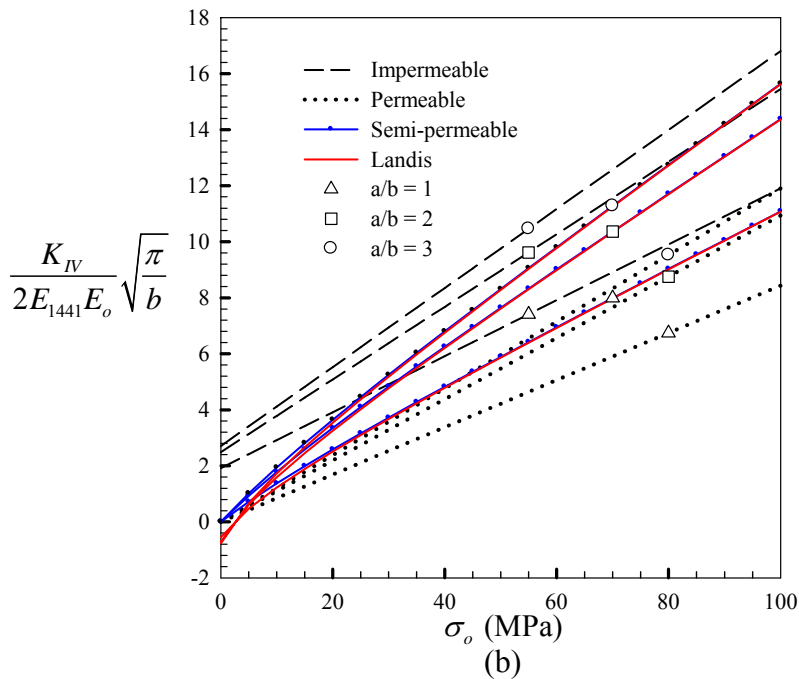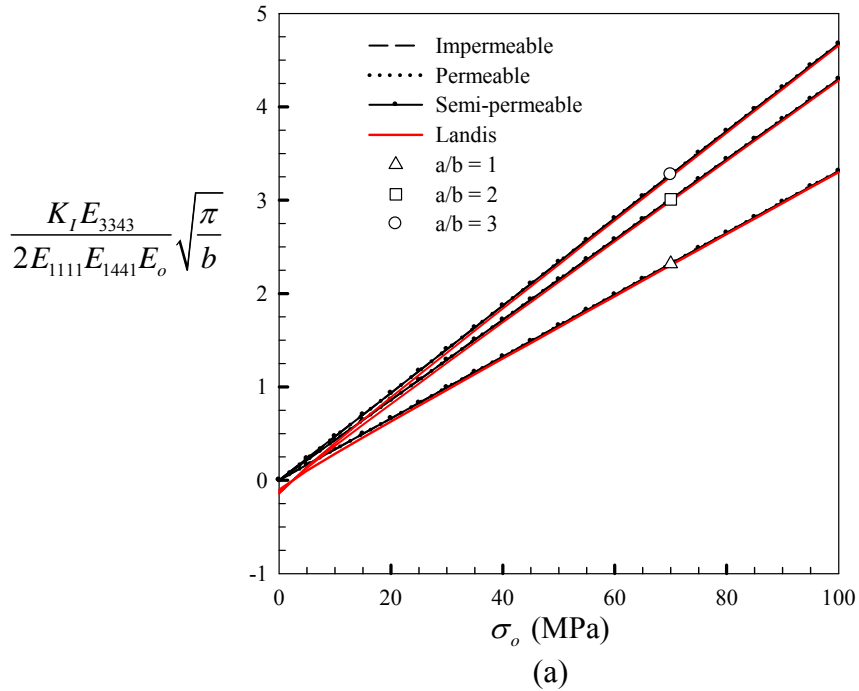
4.3.3 Spherical cap crack in unbounded domain

Consider a spherical cap crack embedded in a transversely isotropic piezoelectric infinite medium. The crack geometry and the material properties of piezoelectric medium are the same as those considered in the example 4.2.1. However, the main differences from the previous case are that (i) the half subtended angle of the surface (θ) is varied as $\theta \in \{15^o, 30^o, 45^o, 60^o\}$ and (ii) the applied uniaxial remote stress is varied from 0 to 100 MPa. The applied electric field E_0 is fixed at 0.5 MV/m which is the same as that for the previous example. Numerical results of intensity factors K_I, K_{II} and K_{IV} computed from the mesh-3 (see Fig. 4.18) are reported in Figs. 4.45-4.50, respectively. It is found that increasing the half subtended angle of the surface tends to increase the magnitude of the mode-II stress intensity factor, but tends to reduce the magnitude of the mode-I stress and electric intensity factors, for all crack models. In addition, the rate of decrease of K_I is more rapid than that of K_{IV} and this can be discussed below.

Figure 4.45(a) shows that when the half subtended angle of the surface is small $(\theta = 15^o)$, the distribution of K_I is similar to that of K_I for a penny-shaped crack; more specifically, K_I of permeable, impermeable and semi-permeable cracks are nearly identical whereas K_I of the Landis-type crack is less than those of the other three cracks.

Figure 4.45(b) shows that, when $\theta = 30^o$, K_I of permeable, impermeable and semi-permeable cracks are clearly separated. More specifically, it is found that when the applied remote mechanical stress is small, K_I of the semi-permeable and the permeable cracks are nearly identical and serve as the upper bound whereas K_I of the Landis-type crack is the lower bound, and K_I of the impermeable crack lies between the upper and lower bounds.

However, when the applied uniform tensile stress increases, the stress intensity factor K_I of permeable and Landis-type cracks are, respectively, the upper and lower bounds of both the semi-permeable and the impermeable cracks, whereas the stress

intensity factor K_I of the semi-permeable crack is always higher than that of the impermeable crack. It is interesting to note that, while the stress intensity factors K_I of impermeable, permeable and semi-permeable cracks for the penny-shaped cracks considered in this study are identical and are independent of the electric loading, results for a spherical crack are not identical. This means that the curvature of crack surface has significant influence on the mode-I stress intensity factor for those three crack models. Moreover, it can be inferred from Figure 4.45(b) that, at zero mechanical stress, K_I of the impermeable crack does not vanish, but it becomes negative.

Figure 4.46(a) shows that, when $\theta = 45^o$, K_I of the permeable crack is the upper bound, whereas K_I of the impermeable and Landis-type cracks are nearly identical and results for both crack models serve as the lower bound. Moreover, it is found that the mode-I stress intensity factor of the semi-permeable crack varies from the upper bound (permeable solution) to the lower bound (impermeable and Landis-type solutions) as the applied remote stress increases. However, it should be noted that, when the applied mechanical stress is small, the stress intensity factor K_I of the Landis-type crack is less than that of the impermeable crack, whereas K_I of the permeable and semi-permeable cracks are nearly identical. As already discussed above, as the half subtended angle (θ) increases, the impermeable solution shifts down and the discrepancy between the upper and lower bound solution increases. In addition, one can clearly see the transition of the semi-permeable solution from the upper to the lower bounds.

Finally, Figure 4.46(b) shows that, when $\theta = 60^o$, the impermeable solution becomes the lower bound in stead of that of the Landis-type crack, whereas the permeable solution is still the upper bound. Moreover, it is observed that the stress intensity factor K_I of the semi-permeable crack is higher than that of the Landis-type crack. One can also see that K_I of the semi-permeable and Landis-type cracks varies from the permeable solution, which is the upper bound, to the impermeable solution, which is the lower bound, as the applied mechanical stress increases.

For the effect of a non-planar crack upon the stress intensity factor K_{II} can be inferred from Figs. 4.47 to 4.48. It is found that increasing the half subtended angle of the surface tends to increase the magnitude of the mode-II stress intensity factor. Moreover, it is obviously seen that the stress intensity factor K_{II} under all four types of electrical boundary conditions are nearly identical for all angle θ. Similarly, the effect of a non-planar crack upon the intensity factor K_{IV} can be inferred from Figs. 4.49 to 4.50. It is found that when the half subtended angle of the crack surface is relatively small ($\theta = 15^o, 30^o$), K_{IV} of the impermeable and permeable cracks are, respectively, the upper and lower bounds of both the semi-permeable and Landis-type solutions except for very small mechanical stress σ_o where K_{IV} of the Landis-type crack is slightly lower than that of the permeable crack. However, when the applied mechanical stress increases, it is found that K_{IV} of the semi-permeable and Landis-type cracks are nearly identical and they approach the impermeable solution. However, when the half subtended angle becomes larger, discrepancy of the impermeable solution and the semi-permeable and Landis-types solutions increases and this implies that results of the semi-permeable and Landis-type cracks tend to approach results of the permeable crack, which is the lower bound, in stead of the impermeable solution, which is the upper bound.
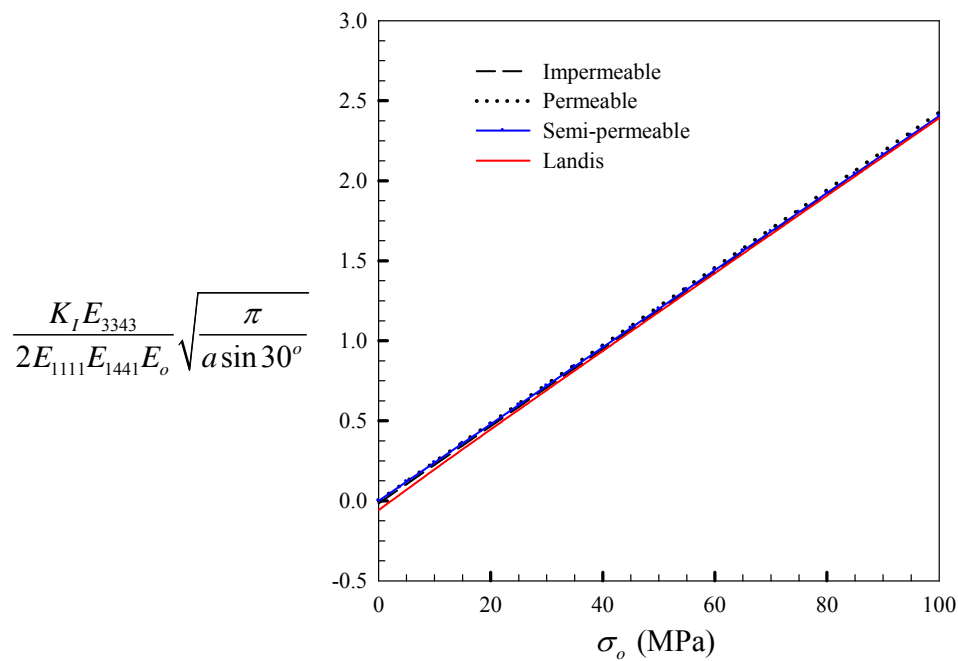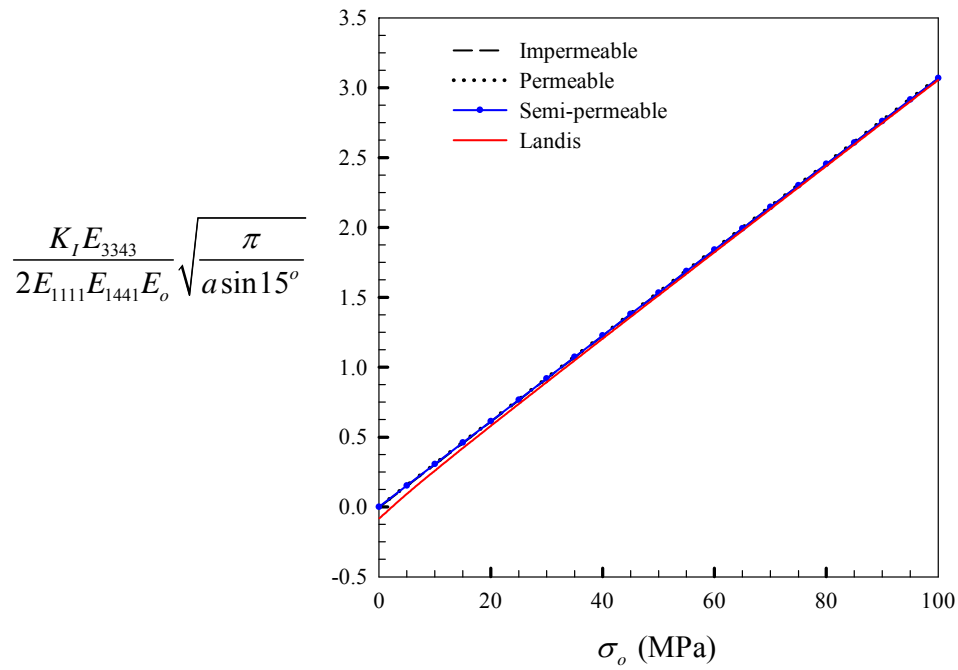
$$\frac{K_I E_{3343}}{2E_{1111}E_{1441}E_o}\sqrt{\frac{\pi}{a\sin 15^o}}$$

(a)

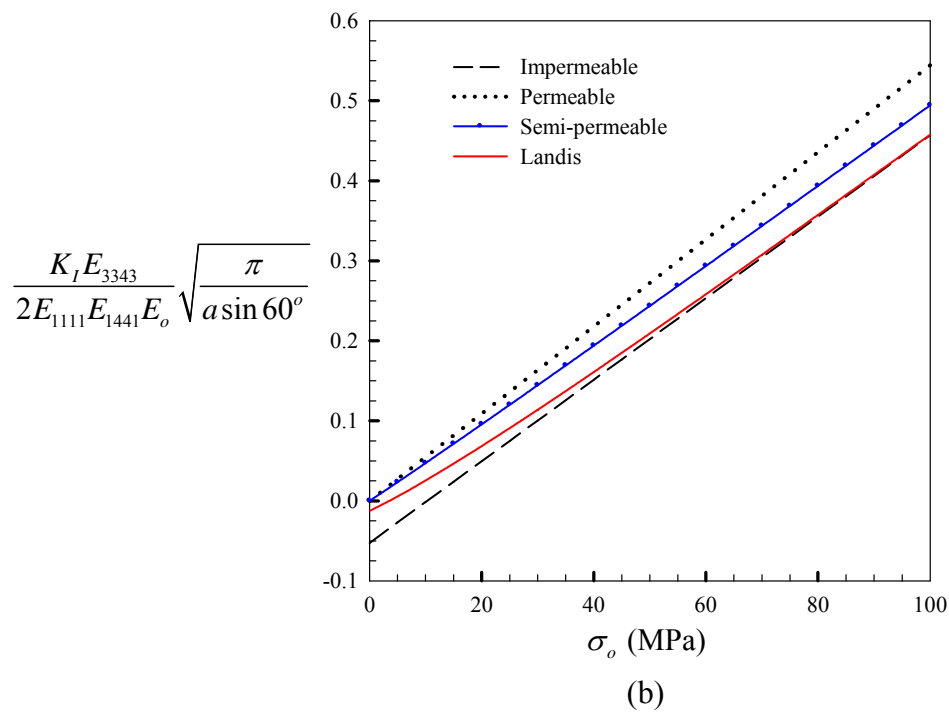$$\frac{K_I E_{3343}}{2E_{1111}E_{1441}E_o}\sqrt{\frac{\pi}{a\sin 30^o}}$$

(b)

Fig. 4.45. Normalized stress intensity factors K_I for a spherical cap crack in an infinite medium for four types of crack assumptions: (a) $\theta = 15^o$ and (b) $\theta = 30^o$

$$\frac{K_I E_{3343}}{2E_{1111}E_{1441}E_o}\sqrt{\frac{\pi}{a\sin 45^o}}$$

(a)

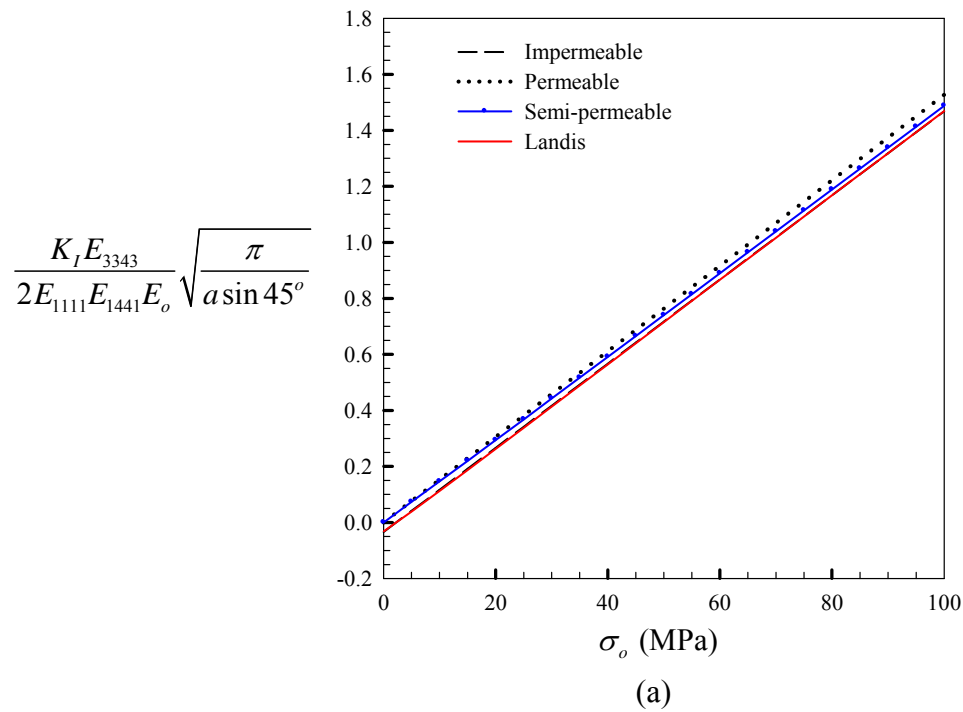$$\frac{K_I E_{3343}}{2E_{1111}E_{1441}E_o}\sqrt{\frac{\pi}{a\sin 60^o}}$$

(b)

Fig. 4.46. Normalized stress intensity factors K_I for a spherical cap crack in an infinite medium for four types of crack assumptions: (a) $\theta = 45^o$ and (b) $\theta = 60^o$

$$\frac{K_{II}E_{3343}}{2E_{1111}E_{1441}E_o}\sqrt{\frac{\pi}{a\sin 15^o}}$$

σ_o (MPa)

(a)

$$\frac{K_{II}E_{3343}}{2E_{1111}E_{1441}E_o}\sqrt{\frac{\pi}{a\sin 30^o}}$$
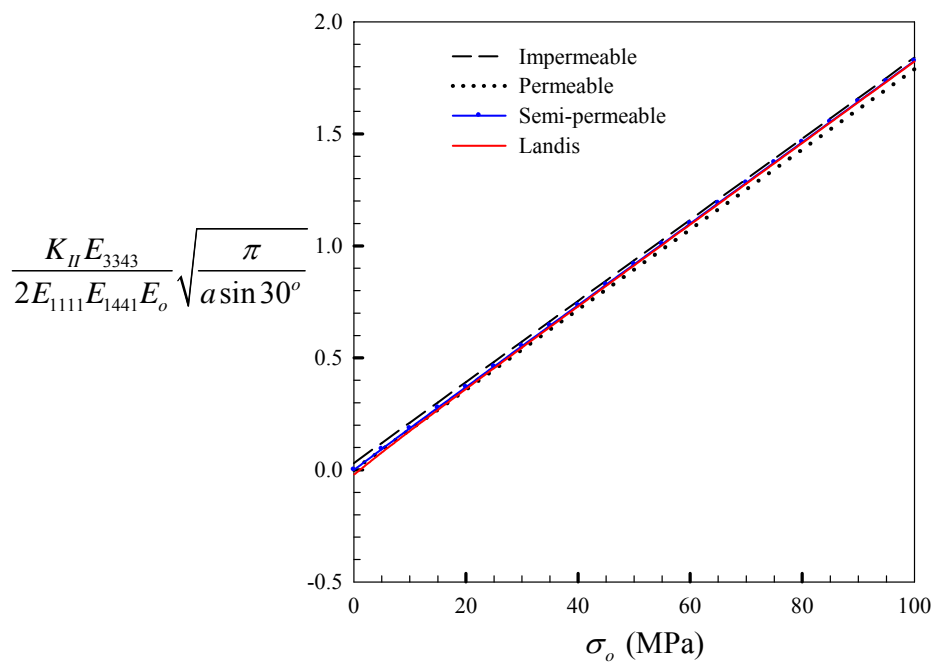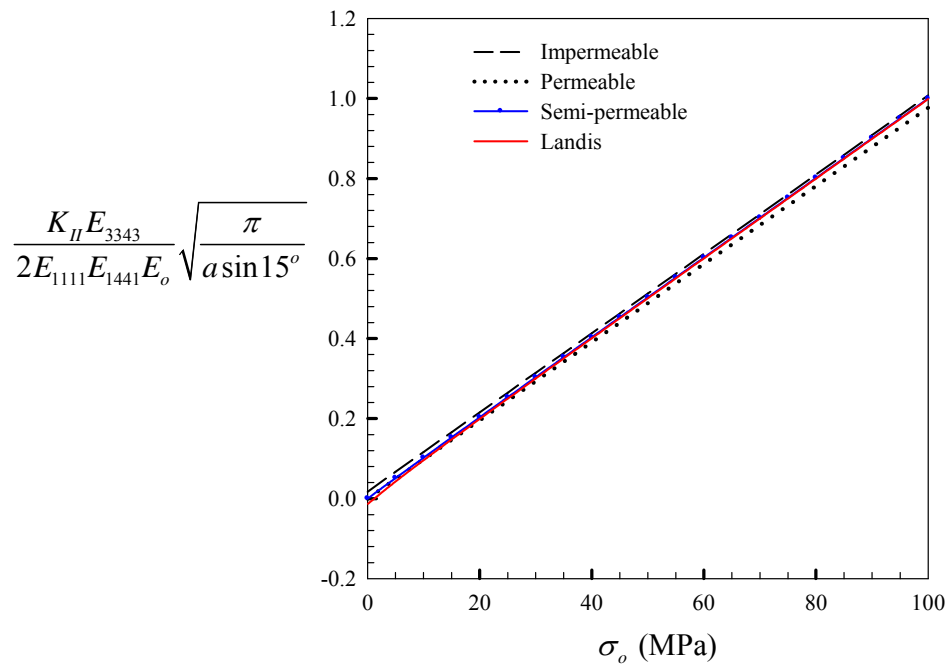
σ_o (MPa)

(b)

Fig. 4.47. Normalized stress intensity factors K_{II} for a spherical cap crack in an infinite medium for four types of crack assumptions: (a) $\theta = 15^o$ and (b) $\theta = 30^o$

$$\frac{K_{II}E_{3343}}{2E_{1111}E_{1441}E_o}\sqrt{\frac{\pi}{a\sin 45^o}}$$

σ_o (MPa)

(a)

$$\frac{K_{II}E_{3343}}{2E_{1111}E_{1441}E_o}\sqrt{\frac{\pi}{a\sin 60^o}}$$
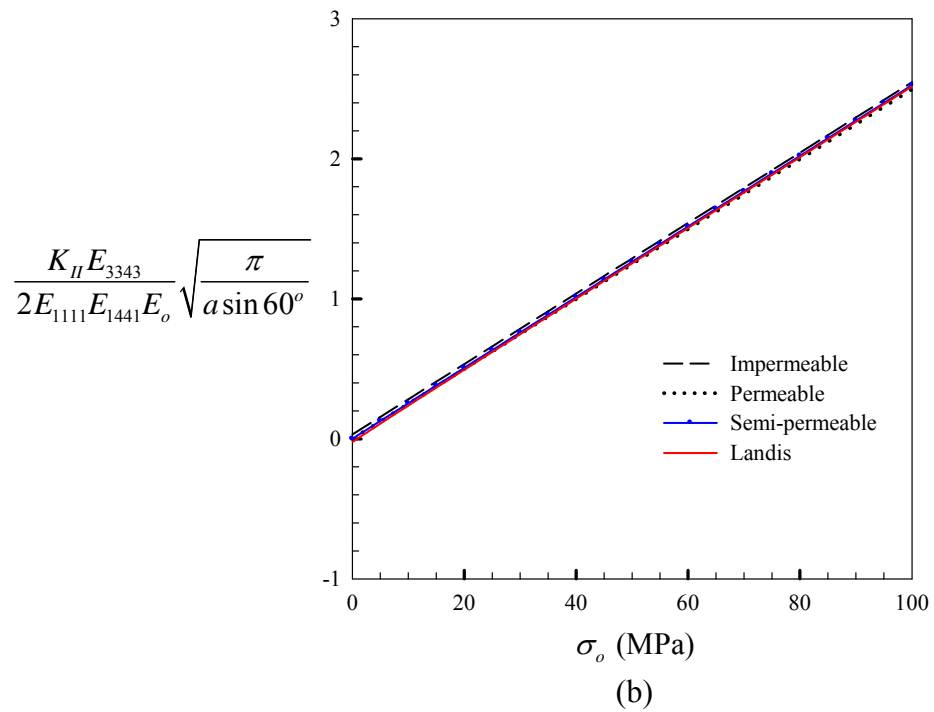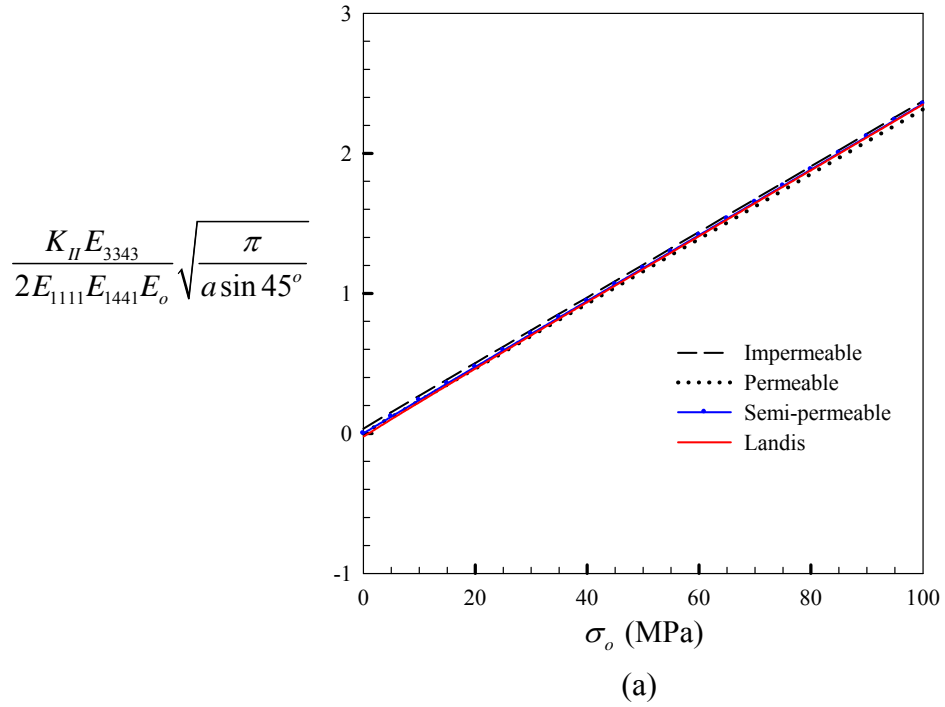
σ_o (MPa)

(b)

Fig. 4.48. Normalized stress intensity factors K_{II} for a spherical cap crack in an infinite medium for four types of crack assumptions: (a) $\theta = 45^o$ and (b) $\theta = 60^o$

Fig. 4.49. Normalized electric intensity factors K_{IV} for a spherical cap crack in an infinite medium for four types of crack assumptions: (a) $\theta = 15^o$ and (b) $\theta = 30^o$

$$\frac{K_{IV}}{2E_{1441}E_o}\sqrt{\frac{\pi}{a\sin 45^o}}$$

(c)

$$\frac{K_{IV}}{2E_{1441}E_o}\sqrt{\frac{\pi}{a\sin 60^o}}$$

(d)

Fig. 4.50. Normalized electric intensity factors K_{IV} for a spherical cap crack in an infinite medium for four types of crack assumptions: (a) $\theta = 45^o$ and (b) $\theta = 60^o$
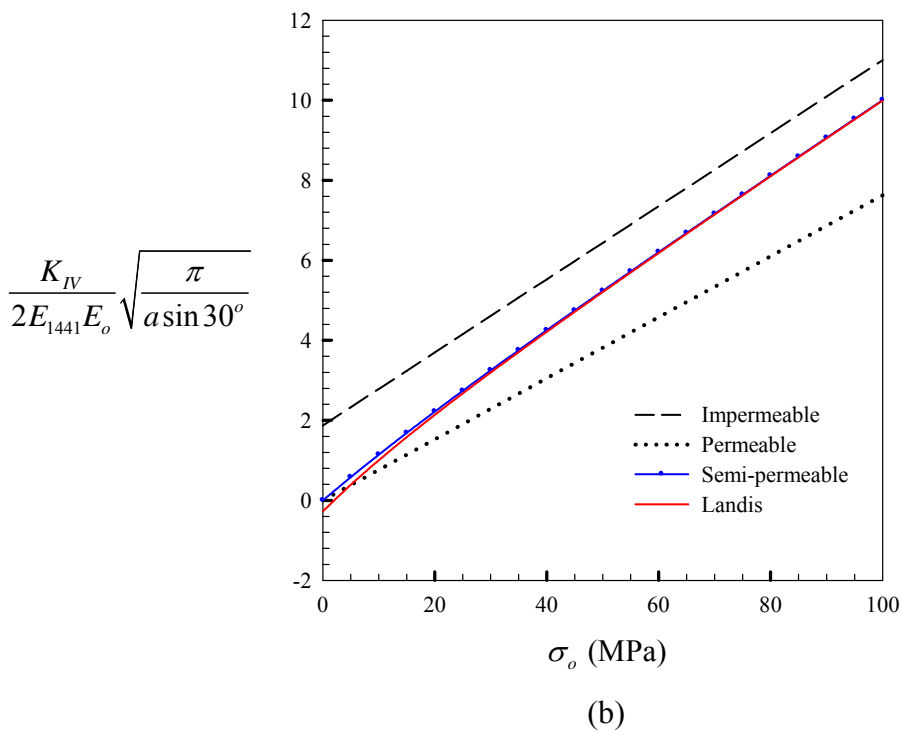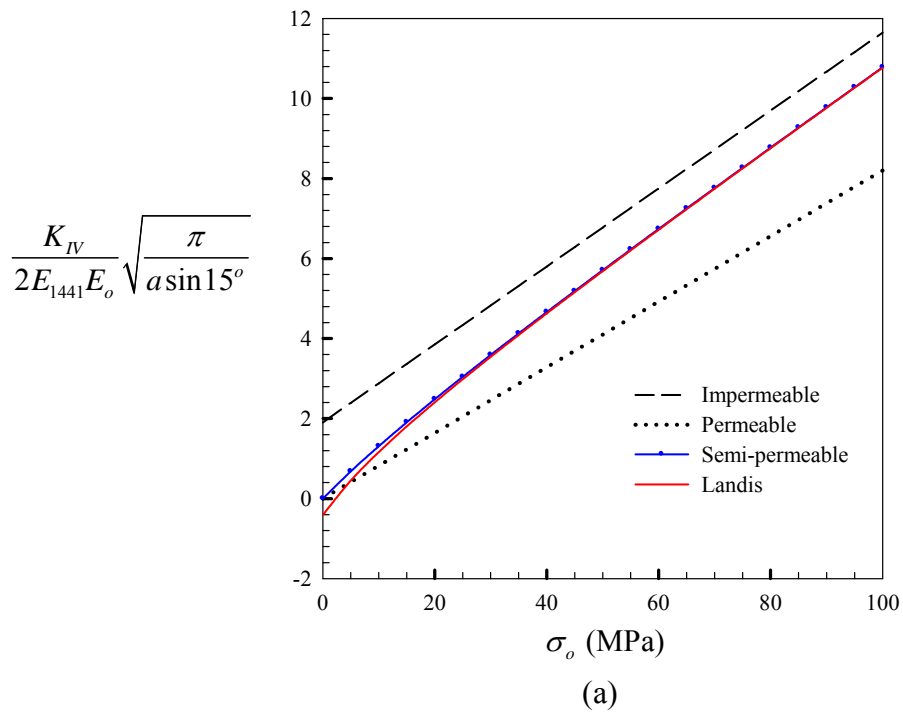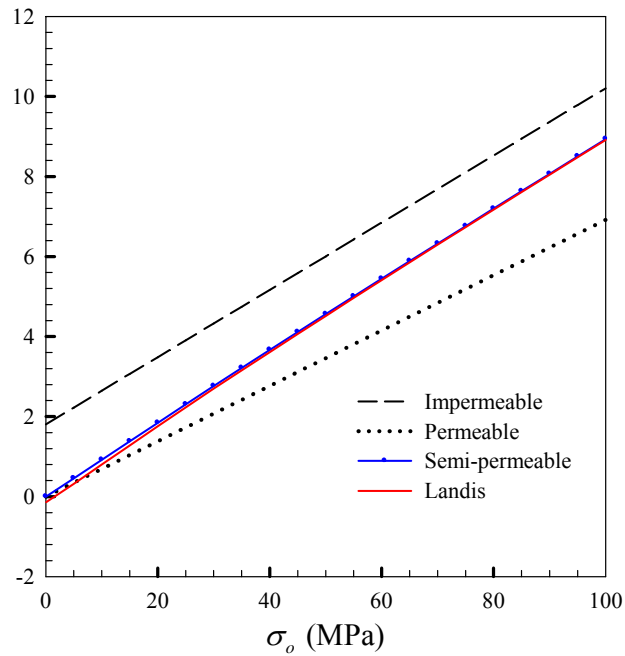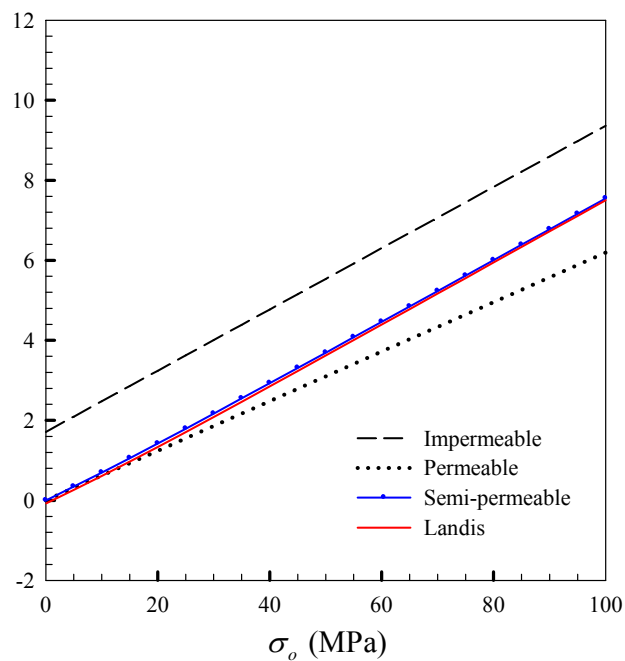
4.3.4 Elliptical crack in a cube

As a final example, consider a finite cube containing an elliptical crack and subjected to uniform normal traction σ_o and uniform surface electric charge d_o at the top and bottom surfaces as shown schematically in Fig. 4.51(a). The width of the cube is denoted by $2w$ and the major and minor semi-axes of the elliptical crack are denoted by a and b, respectively. The crack is located at the center of the cube and is oriented as shown in Fig. 4.51(b). The cube is made of a transversely isotropic piezoelectric material PZT-5H with its axis of material symmetry normal to the plane of the crack. In the analysis, $a/w = 0.5$ and $a/b = 2$ are taken and three meshes are adopted as indicated in Fig. 4.52.

The computed mode-I stress intensity factor and electric intensity factor obtained from the three meshes, under four types of crack assumptions, are reported in Figs. 4.53 to 4.56 for the loading ratio $(\sigma_o / E_{3333})/(d_o / E_{3343}) = 0.20$. It is found that the numerical results obtained from all three meshes, for each type of crack assumptions, are in good agreement. More specifically, results obtained from the mesh-2 and mesh-3 are nearly indistinguishable. Even the coarsest mesh (i.e. mesh-1), which utilizes only four elements along the crack front, accurately captures the distribution of the stress and electric intensity factors.

Moreover, it can be inferred from Fig. 4.57(a) that the mode-I stress intensity factors of the impermeable, permeable and semi-permeable cracks are nearly identical and are greater than that of the Landis-type crack. In contrast with the mode-I stress intensity factor, the electric intensity factor under four types of crack assumptions are completely different. Fig. 4.57(b) indicates that the electric intensity factors of the impermeable and permeable cracks are, respectively, the upper and lower bund solutions of both the semi-permeable and Landis-type solutions, and results of the Landis-type crack is less than that of semi-permeable crack.
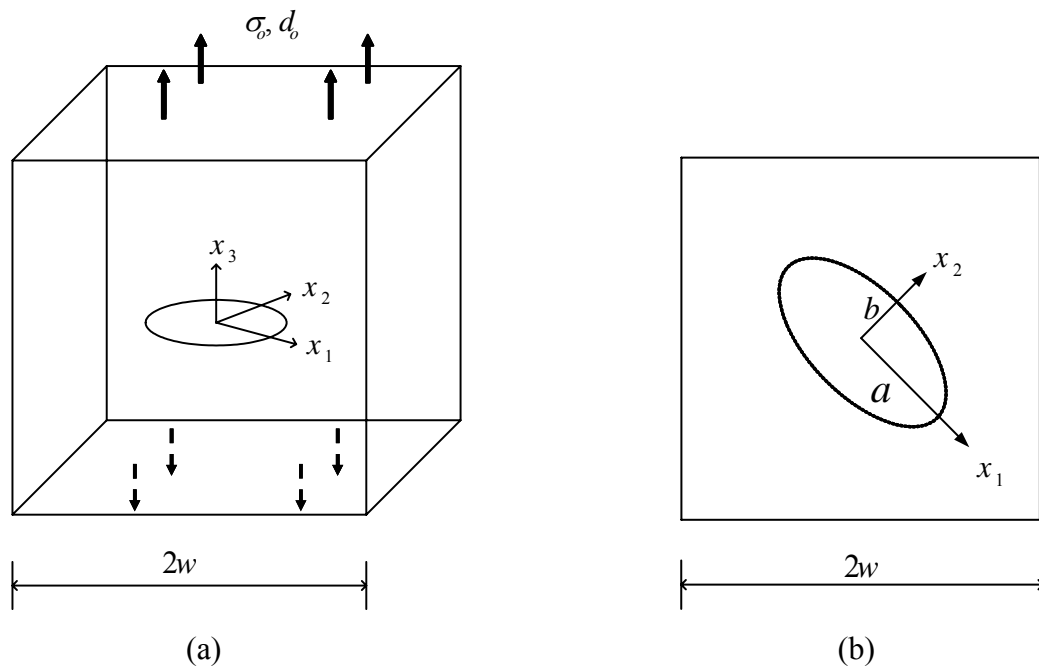
Fig. 4.51. (a) Schematic of cube containing elliptical crack and subjected to uniform normal traction and surface electric charge at the top and bottom surfaces and (b) top view indicating orientation of elliptical crack

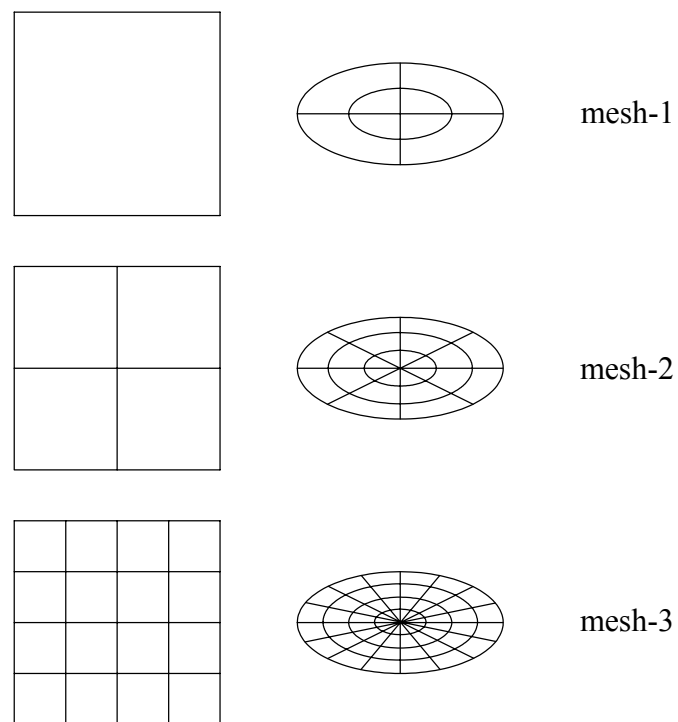Fig. 4.52. Three meshes adopted in the analysis
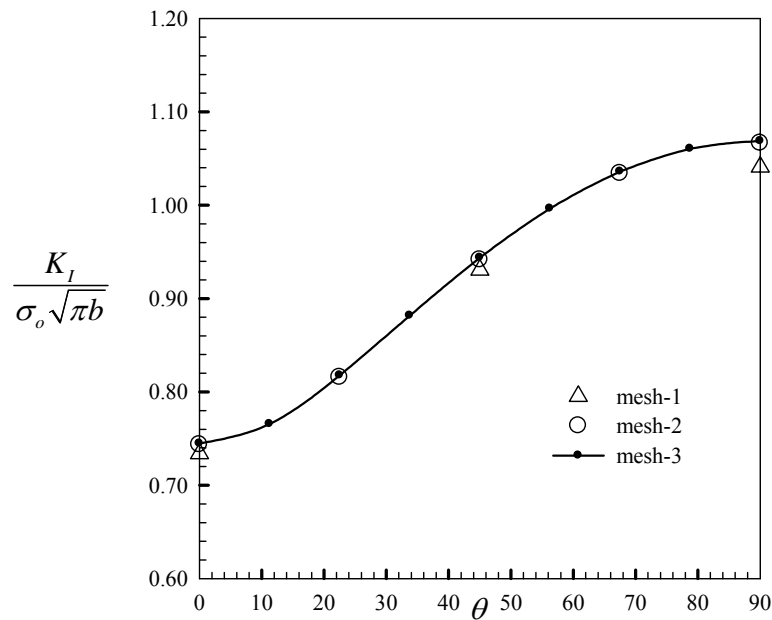
(a)
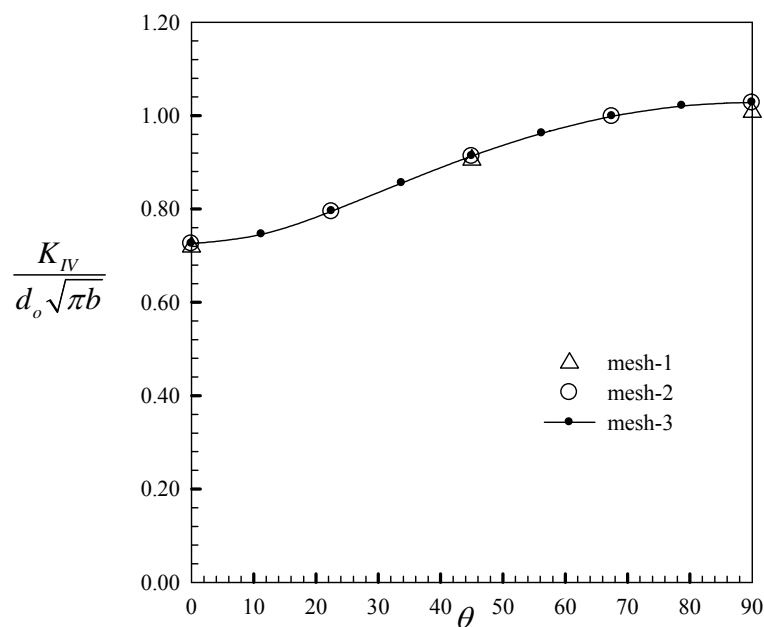
(b)

Fig. 4.53. Normalized intensity factor for elliptical crack in cube subjected to uniform normal traction and uniform surface electric charge for impermeable crack where θ is an angle used to parameterize the crack front: $x_1 = a\cos\theta$ and $x_2 = b\sin\theta$; (a) stress intensity factor K_I and (b) electric intensity factor K_{IV}.

(a)

(b)

Fig. 4.54. Normalized intensity factor for elliptical crack in cube subjected to uniform normal traction and uniform surface electric charge for permeable crack where θ is an angle used to parameterize the crack front: $x_1 = a\cos\theta$ and $x_2 = b\sin\theta$; (a) stress intensity factor K_I and (b) electric intensity factor K_{IV}.
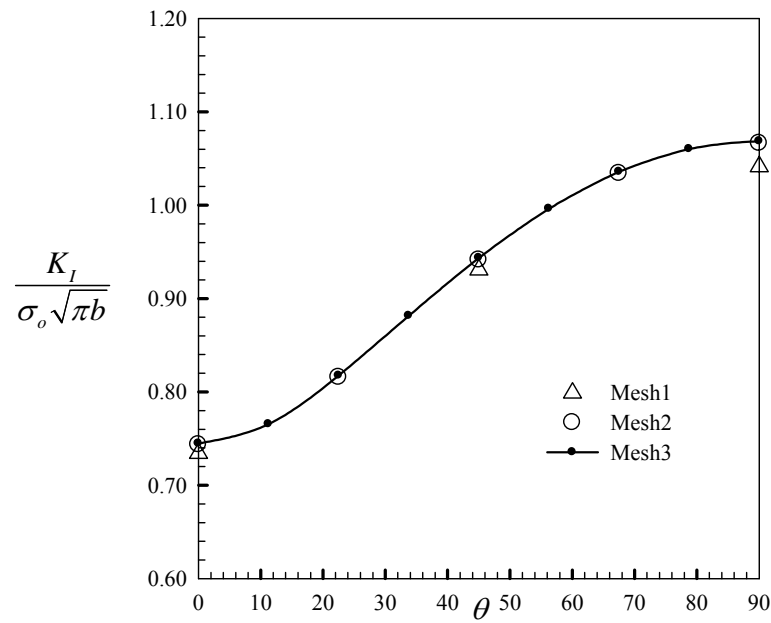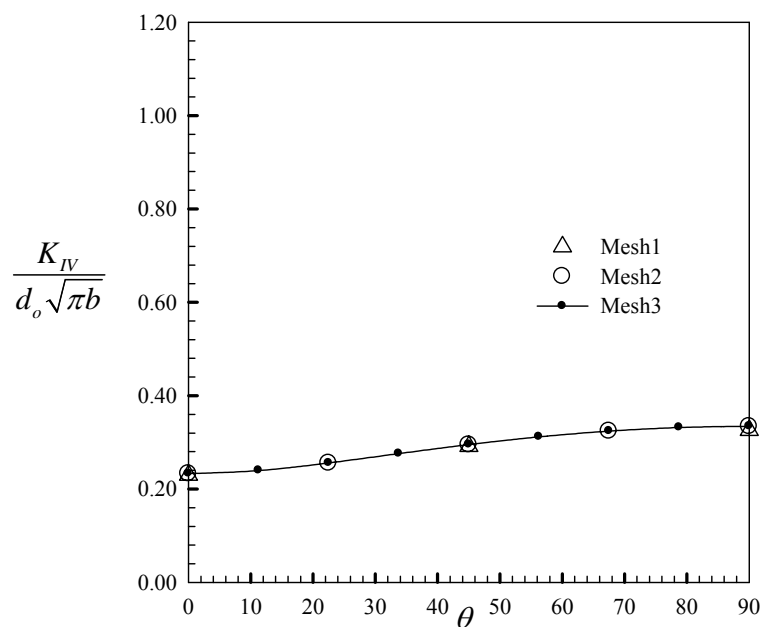
Fig. 4.55. Normalized intensity factor for elliptical crack in cube subjected to uniform normal traction and uniform surface electric charge for semi-permeable crack where θ is an angle used to parameterize the crack front: $x_1 = a\cos\theta$ and $x_2 = b\sin\theta$; (a) stress intensity factor K_I and (b) electric intensity factor K_{IV}.
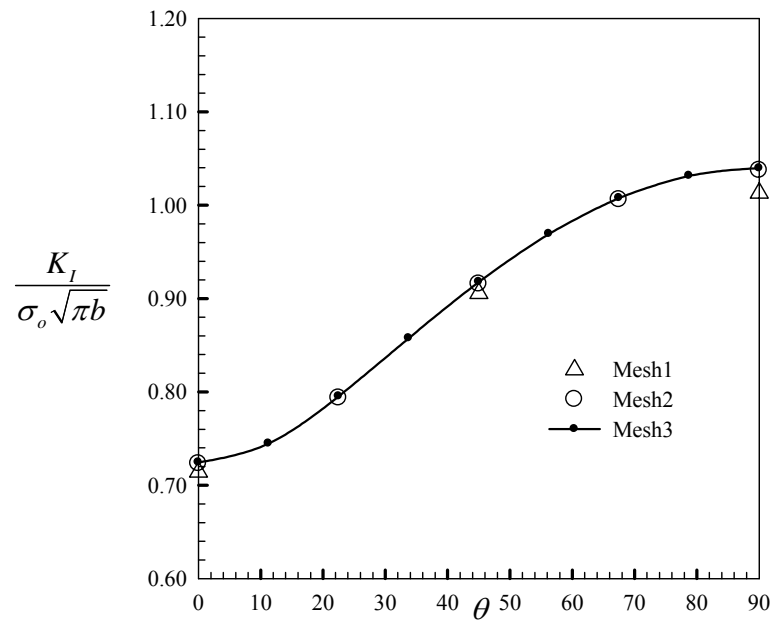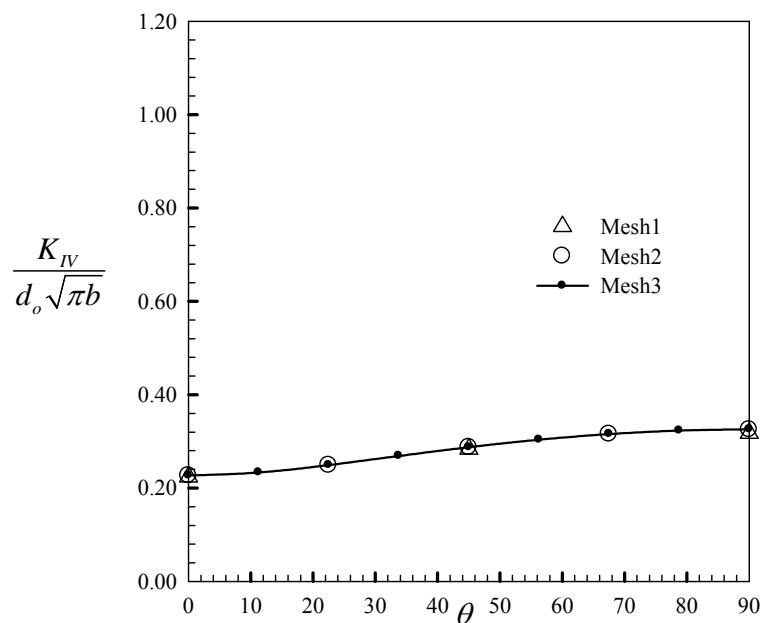
Fig. 4.56. Normalized intensity factor for elliptical crack in cube subjected to uniform normal traction and uniform surface electric charge for Landis-type crack where θ is an angle used to parameterize the crack front: $x_1 = a\cos\theta$ and $x_2 = b\sin\theta$; (a) stress intensity factor K_I and (b) electric intensity factor K_{IV}.
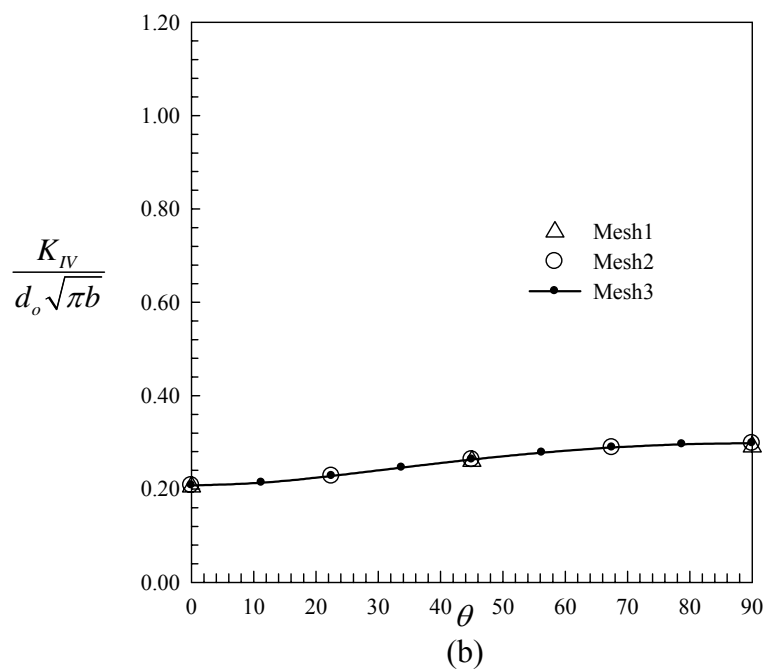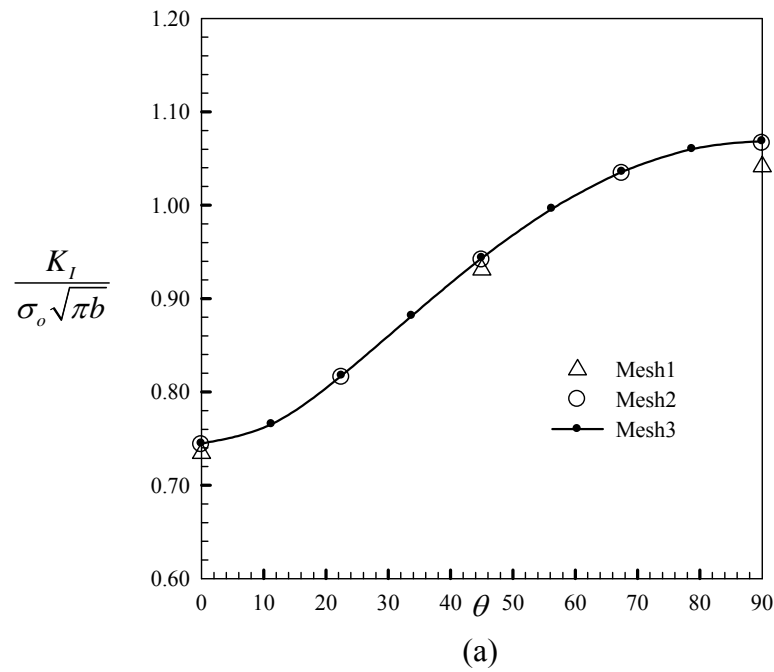
(a)

(b)

Fig. 4.57. Normalized intensity factor for elliptical crack in cube subjected to uniform normal traction and uniform surface electric charge for four types of crack assumptions where θ is an angle used to parameterize the crack front: $x_1 = a\cos\theta$ and $x_2 = b\sin\theta$; (a) stress intensity factor K_I and (b) electric intensity factor K_{IV}.
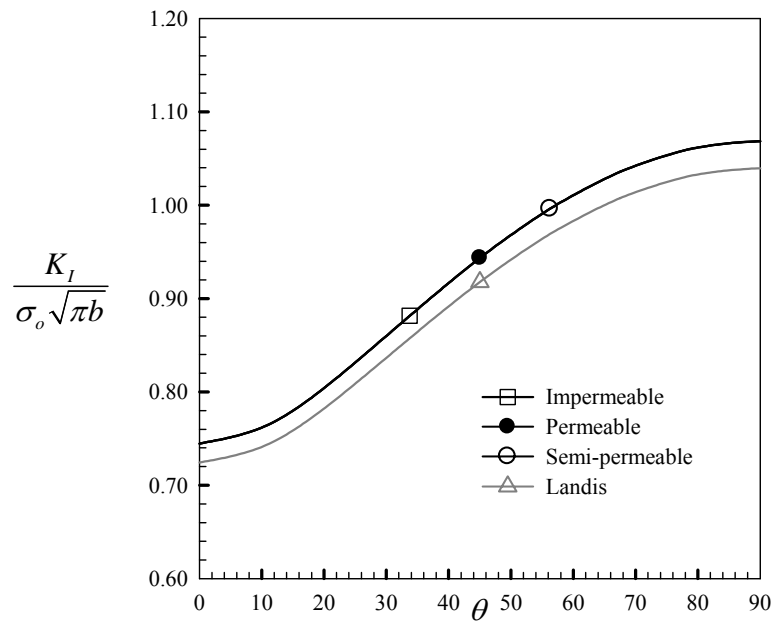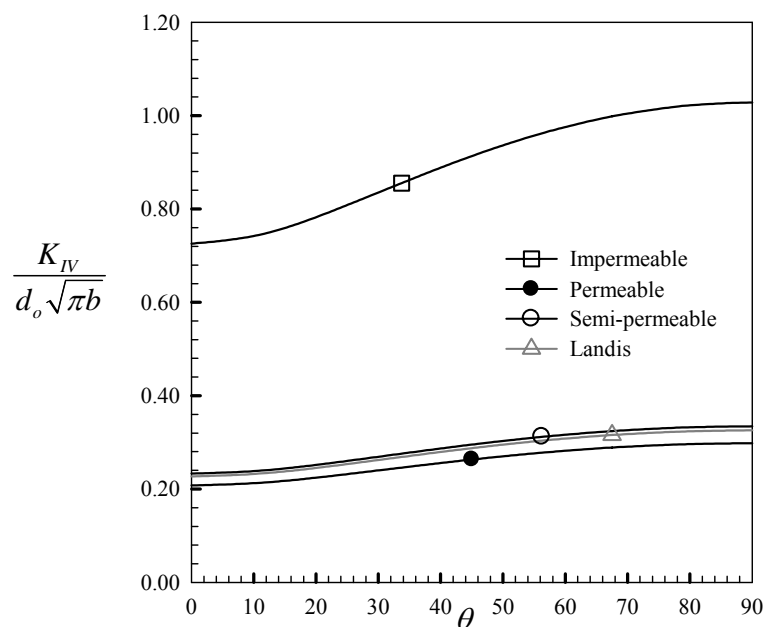
CHAPTER V

CONCLUSIONS

A weakly singular SGBEM is developed for analysis of cracks in three-dimensional, generally anisotropic, linear piezoelectric infinite and finite media under four types of crack assumptions (i.e. permeable, impermeable, semi-permeable and Landis-type cracks). The governing equation, which is in a symmetric form well-suited to deal with the arbitrary crack geometries under various types of crack assumptions, is based upon a pair of weak-form integral equations for the generalized displacement and the generalized surface traction. Since both integral equations contain only the weakly singular kernels of $\mathcal{O}(1/r)$, the C^o-interpolations can be employed to approximate the solution and test functions on the entire boundary and crack surface. For the region near the crack front, special crack-tip elements, which were proposed by Rungamornrat and Mear (2008c), is used to approximate the jump of the generalized displacement. These special crack-tip elements have two advantage features: the first one is the corresponding shape functions can capture the first three terms of asymptotic fields and the other is extra degrees of freedom introduced along the crack front to directly capture to the strength of singularity. The former feature enables relatively large crack-tip elements be used along the crack front whereas the later provides a direct means to determine the mixed-mode stress intensity factors and the electric intensity factor without carrying extrapolations.

Boundary value problems with existing analytical solution are examined first in order to verify the current method. The first one is a penny-shaped crack embedded in a piezoelectric infinite domain and the other is a piezoelectric finite body containing a penny-shaped crack that mimics exactly the problem of an isolated crack in an unbounded domain where the exact generalized stress field is available. Results indicate that the computed stress and electric intensity factors are in excellent agreement with the exact solution. Moreover, the solution verification technique using the impermeable scheme is proposed for problems of cracks in a piezoelectric finite body when the exact generalized stress field or the reference solution is not available for comparison.

Once the weakly singular SGBEM is validated through various numerical experiments for both infinite and finite crack bodies under all four types of crack assumptions, a set of more complex problems are considered to demonstrate the capabilities and versatility of the current technique to model cracks and bodies of various geometries and under different loading conditions. It was found that the technique is robust and promising. In particular, it yields highly accurate numerical solutions for the stress and electric intensity factors along the crack front with only weak dependence on the level of mesh refinement. Finally, the influence of all four types of crack assumptions upon the stress and electric intensity factors for piezoelectric infinite and finite media is thoroughly explored.

For a planar crack embedded in an unbounded domain (either a penny-shaped crack or an elliptical crack), the stress intensity factors K_I of permeable, impermeable and semi-permeable cracks are identical since they depend only on the mechanical loading but are independent of the electric loading. In contrast with those three crack models, K_I of the Landis-type crack depends on the electric loading as well as the mechanical loading. Numerical results also indicate that K_I of the Landis-type crack is less than of those of the other three crack models when the applied remote mechanical stress is relatively small. However, when the applied remote mechanical stress increases, K_I for all crack assumptions are nearly identical.

Unlike the mode-I stress intensity factor, the electric intensity factors K_{IV} of all four crack models are completely different. More specifically, the electric intensity factor K_{IV} of the impermeable crack is the upper bound (for the entire range of the applied remote mechanical stress) whereas K_{IV} of the Landis-type crack is the lower bound when the applied remote mechanical stress is nearly zero. However, when the applied mechanical stress increases, the electric intensity factor K_{IV} of the permeable crack becomes the lower bound in stead of the Landis-type solution, whereas K_{IV} of the semi-permeable and Landis-type cracks are nearly identical and approach the impermeable solution.

However, the behavior of a penny-shaped crack under the shear loading is different from that under the tension loading. The mode-II and mode-III stress

intensity factors of a penny-shaped crack under the shear loading are identical for permeable, impermeable, semi-permeable and Landis-type cracks. This implies that the electrical boundary conditions on the crack surface have no influence on the stress intensity factors K_{II} and K_{III} of a penny-shaped crack under the shear loading as long as the crack surface is still closed.

Unlike the planar cracks, the stress intensity factors $\{K_I, K_{II}\}$ and the electric intensity factor K_{IV} are non-zero for a spherical cap crack embedded in an unbounded domain under the tension loading. It is found that the mode-I stress intensity factors for the penny-shaped crack and the spherical cap crack under tension loading are different. While K_I of the impermeable, permeable and semi-permeable cracks are identical for both penny-shaped and elliptical cracks, the stress intensity factors K_I of those three crack models for the spherical cap crack are not identical and one can clearly see when the half subtended angle of the surface (θ) becomes larger. This implies that the curvature of non-planar cracks renders the dependence of the electric field on the mode-I stress intensity factor, while, as discussed in the case of planar cracks, the electric field has no effect on K_I of permeable, impermeable and semi-permeable cracks but exhibits influence on results of the Landis-type crack. Moreover, numerical results indicate that the more increase of the half subtended angle of the surface of the spherical cap crack, the more downward shift of the K_I curve of the impermeable crack and the more increase of the gap between the upper and lower bounds of the mode-I stress intensity factors. As a result, one can see the transition between the upper and lower bounds of the stress intensity factor K_I for all four types of crack models.

For the mode-II stress intensity factor of a spherical cap crack under the tension loading, it is found that the more increase of the half subtended angle of the surface, the more increase of the magnitude of the mode-II intensity factors for all four types of crack assumptions (i.e. permeable, impermeable, semi-permeable and Landis-type cracks). Moreover, it is obviously seen that K_{II} for all four types of crack models are nearly identical for all half subtended angle considered.

For the electric intensity factor of a spherical cap crack under the tension loading, it is found that its distribution is similar to those of a penny-shaped crack (or an elliptical crack) when the half subtended angle of the surface of the spherical crack is not large ($\theta = 15^o, 30^o$). More specifically, the electric intensity factor K_{IV} of the impermeable crack is always the upper bound for the entire range of the applied mechanical stress whereas the Landis-type solution is a lower bound when the applied mechanical stress is very small. However, when the applied mechanical stress increases, the permeable solution becomes the lower bound in stead of the Landis-type solution. In addition, results of the Landis-type crack are nearly identical to those of the semi-permeable crack and both solutions approach the upper bound (i.e., the impermeable solution). However, when the half subtended angle of the surface of a spherical cap crack becomes larger, the gap between the impermeable solution and the semi-permeable and Landis-type solutions increases and this implies that the electric intensity factors K_{IV} of the semi-permeable and Landis-type cracks tend to approach the results of the permeable crack in stead of the impermeable solution.

Finally, the investigation of all four types of crack models upon the stress intensity factors and the electric intensity factor for piezoelectric finite bodies containing a planar crack (i.e. an elliptical crack embedded in a finite cube) indicated that the mode-I stress intensity factors of the permeable, impermeable and semi-permeable cracks are nearly identical and are greater than K_I of the Landis-type crack. Moreover, it is found that the electric intensity factors K_{IV} of the impermeable and permeable cracks are, respectively, the upper and lower bounds of those of the semi-permeable and Landis-type cracks, and the electric intensity factor K_{IV} of the semi-permeable crack is greater than the Landis-type solution.

REFERENCES

Bacon, D.J., Barnett, D.M., and Scattergood, R.O. 1978. Anisotropic continuum theory of lattice defects. Progress in Materials Science 23: 51-262.

Bui, H.D. 1977. An integral equation method for solving the problem of a plane crack of arbitrary shape. J. Mech. Phys. Solids 25: 29-39.

Chen, M.C. 2003a. Application of finite-part integrals to the three-dimensional fracture problems for piezoelectric media, Part I: hypersingular integral equation and theoretical analysis. Int. J. Fract. 121: 133-148.

Chen, M.C. 2003b. Application of finite-part integrals to the three-dimensional fracture problems for piezoelectric media, Part II: numerical analysis. Int. J. Fract. 121: 149–161.

Chen, W.Q., and Lim, C.W. 2005. 3D point force solution for a permeable penny-shaped crack embedded in an infinite transversely isotropic piezoelectric medium. Int. J. Fract. 131: 231–246.

Chen, W.Q., and Shioya, T. 2000. Complete and exact solutions of a penny-shaped crack in a piezoelectric solid: antisymmetric shear loadings. Int. J. Solids Struct. 37: 2603–2619.

Chen, W.Q., Shioya, T., and Ding, H.J. 2000. A penny-shaped crack in piezoelectrics: resolved. Int. J. Fract. 105: 49–56.

Chiang, C.R., and Weng, G.J. 2007. Nonlinear behavior and critical state of a penny-shaped dielectric crack in a piezoelectric solid. Journal of Applied Mechanics 74: 852–860.

Davi, G., and Milazzo, A. 2001. Multidomain boundary integral formulation for piezoelectric materials fracture mechanics. Int. J. Solids Struct. 38: 7065-7078.

Deans, S.R. 1983. The Radon transform and some of its applications. Wiley, New York.

Deeg, W.F. 1980. The analysis of dislocation, crack and inclusion problems in piezoelectric solids. Doctoral dissertation, Department of Materials Science and Engineering, Standford University.

Denda, M., and Mansukh, M. 2005. Upper and lower bounds analysis of electric induction intensity factors for multiple piezoelectric cracks by the BEM. Eng. Anal. Bound. Elem. 29: 533-550.

Dunn, M.L. 1994. The effects of cracks face boundary conditions on the fracture mechanics of piezoelectric solids. Engineering fracture mechanics 48: 25-39.

Frangi, A., Novati, G., Springhetti, R., and Rovizzi, M. 2002. 3D fracture analysis by the symmetric Galerkin BEM. Comput. Mech. 28: 220-232.

Gao, C.F., and Fan, W.X. 1999. Exact solutions for the plane problem in piezoelectric materials with an elliptic or a crack. Int. J. Solids Struct. 36: 2527-2540.

Gel'fand, I.M., Graev, M.I., and Vilenkin, N.Y. 1966. In: Generalized functions: Integral geometry and representation theory, Vol. 5. Academic Press, New York.

Groh, U., and Kuna, M. 2005. Efficient boundary element analysis of cracks in 2D piezoelectric structures. Int. J. Solids Struct. 42: 2399-2416.

Gu, H., and Yew, C.H. 1988. Finite element solution of a boundary integral equation for mode I embedded three-dimensional fractures. Int. J. Numer. Methods Eng. 26: 1525-1540.

Hao, T.H., and Shen, Z.Y. 1994. A new electric boundary condition of electric fracture mechanics and its applications. Engineering Fracture Mechanics 47: 793-802.

Hayami, K. 1992. A projection transformation method for nearly singular surface boundary element integrals. In: Brebbia CA, Orszag SA, editors. Lecture notes in engineering, Berlin: Springer-Verlag. 73.

Hayami, K., and Brebbia, C.A. 1988. Quadrature methods for singular and nearly singular integrals in 3-D boundary element method. In: Brebbia CA, editor. Boundary element X, vol. 1. Berlin: Springer-Verlag. 237-264.

Hayami, K., and Matsumoto, H. 1994. A numerical quadrature for nearly singular boundary element integrals. Eng. Anal. Bound. Elem. 13: 143-154.

Helgason, S. 1999. The Radon Transform, second ed. Birkhauser, Boston.

Jiang, L.Z., and Sun, C.T. 2001. Analysis of indentation cracking in piezoceramics. Int. J. Solids Struct. 38: 1903-1918.

Kogan, L., Hui, C.Y., and Molkov, V. 1996. Stress and induction field of a spheroidal inclusion or a penny-shaped crack in a transversely isotropic piezoelectric material. Int. J. Solids Struct. 33: 2719-2737.

Landis, C.M. 2004. Energetically Consistent Boundary Conditions for Electromechanical Fracture. Int. J. Solids Struct. 41: 6291–6315.

Li, H.B., and Han, G.M. 1985. A new method for evaluating singular integrals in stress analysis of solids by the direct boundary element method. Int. J. Numer. Methods. Eng. 21: 2071-2098.

Li, Q., and Chen, Y.H. 2008. Why traction-free? Piezoelectric crack and Coulombic traction. Archive of applied mechanics 78: 559-573.

Li, Q., Ricoeur, A., and Kuna, M. 2011. Coulomb traction on a penny-shaped crack in a three dimensional piezoelectric body. Archive of applied mechanics 81: 685-700.

Li, S., and Mear, M.E. 1998. Singularity-reduced integral equations for displacement discontinuities in three-dimensional linear elastic media. Int. J. Fract. 93: 87-114.

Li, S., Mear, M.E., and Xiao, L. 1998. Symmetric weak-form integral equation method for three-dimensional fracture analysis. Comput. Methods Appl. Mech. Engrg. 151: 435-539.

Li, X.F., and Lee, K.Y. 2004. Three-dimensional electroelastic analysis of a piezoelectric material with a penny-shaped dielectric crack. Journal of Applied Mechanics 71: 866-878.

Martin, P.A., and Rizzo, F.J. 1996. Hypersingular integrals: how smooth must the density be?. Int. J. Numer. Methhods Eng. 39: 687–704.

McMeeking, R.M. 1999. Crack tip energy release rate for a piezoelectric compact tension specimen. Engineering Fracture Mechanics 64: 217-244.

McMeeking, R.M. 2001. Towards a fracture mechanics for brittle piezoelectric and dielectric materials. International Journal of Fracture 108: 25-41.

McMeeking, R.M. 2004. The energy release rate for a griffith crack in a piezoelectric material. Engineering Fracture Mechanics 71: 1149–1163.

Motala, Y., and Banks-Sills, L. 2009. M-integral for calculating intensity factors of cracked piezoelectric materials using the exact boundary conditions. Journal of Applied Mechanics. 76: 011004-1-011004-9.

Nam, B.G., and Watanabe, K. 2008. Effect of electric boundary conditions on crack energy density and its derivatives for piezoelectric material. Engineering Fracture Mechanics 75: 207-222.

Ou, Z.C., and Chen, Y.H. 2003. Discussion of the Crack Face Electric Boundary Condition in Piezoelectric Fracture Mechanics. Int. J. Fract. 123: L151–L155.

Ou, Z.C., and Chen, Y.H. 2007. Re-examination of the PKHS crack model in piezoelectric materials. European Journal of Mechanics A/Solids 26: 659-675.

Pak, Y.E. 1992. Circular inclusion problem in antiplane piezoelectricity. Int. J. Solids Struct. 29: 2403-2419.

Pan, E. 1999. A BEM analysis of fracture mechanics in 2D anisotropic piezoelectric solids. Eng. Anal. Bound. Elem. 23: 67–76.

Park, S.B., and Sun, C.T. 1995. Effect of electric field on fracture of piezoelectric ceramics. Int. J. Fract. 70: 302-316.

Parton, V.Z. 1976. Fracture mechanics of piezoelectric materials. Acta Astronaut 3: 671-683.

Qin, T.Y., and Noda, N.A. 2004. Application of hypersingular integral equation method to a three-dimensional crack in piezoelectric materials. JSME International Journal Series A 47(2): 173-180.

Qin, T.Y., Yu Y.S., and Noda, N. A. 2007. Finite-part integral and boundary element method to solve three-dimensional crack problems in piezoelectric materials. Int. J. Solids Struct. 44: 4770–4783.

Rungamornrat, J., and Mear, M.E. 2008a. Weakly-singular, weak-form integral equations for cracks in three-dimensional anisotropic media. Int. J. Solids Struct. 45: 1283-1301.

Rungamornrat, J., and Mear, M.E. 2008b. A weakly-singular SGBEM for analysis of cracks in 3D anisotropic media. Comput. Methods Appl. Mech. Engrg. 197: 4319-4332.

Rungamornrat, J., and Mear, M. E. 2008c. Analysis of fractures in 3D piezoelectric media by a weakly singular integral equation method. Int. J. Fract. 151: 1- 27.

Sanz, J.A., Ariza M.P., and Dominguez J. 2005. Three-dimensional BEM for piezoelectric fracture analysis. Eng. Anal. Bound. Elem. 29: 586–596.

Schneider, G.A., Felten, F., and McMeeking, R.M. 2003. The electrical potential difference across cracks in PZT measured by Kelvin Probe Microscopy and the implications for fracture. Acta Materialia. 51: 2235-2241.

Sladek, V., and Sladek, J. 1982. Three dimensional crack analysis for an anisotropic body. Appl. Math. Modeling. 6: 374-380.

Solis, M., Sanz, J.A., Ariza, M.P., and Dominguez, J. 2009. Analysis of cracked piezoelectric solids by a mixed three-dimensional BE approach. Eng. Anal. Bound. Elem. 33: 271-282.

Sosa, H., and Khutoryansky, N. 1996. New developments concerning piezoelectric materials with defects. Int. J. Solids Struct. 33: 3399-3414.

Suo, Z., Kuo, C.M., Barnet, D.M., and Willis, J.R. 1992. Fracture mechanics for piezoelectric ceramics. J. Mechs. Phys. Solids 40: 739-765.

Wang, B.L., and Mai, Y.W. 2003. On the electrical boundary conditions on the crack surfaces in piezoelectric ceramics. Int. J. Eng. Sci. 41: 633–652.

Wang, X.D., and Jiang, L.Y. 2002. Fracture behavior of cracks in piezoelectric media with electromechanically coupled boundary conditions. Proc. R. Soc. London, Ser. A 458: 2545–2560.

Wang, X.D., and Jiang, L.Y. 2004. The nonlinear fracture behaviour of an arbitrarily oriented dielectric crack in piezoelectric materials. Acta Mechanica 172: 195–210.

Weaver, J. 1977. Three-dimensional crack analysis. Int. J. Solids Struct. 13: 321-330.

Wippler, K., and Kuna, M. 2007. Crack analyses in three-dimensional piezoelectric structures by the BEM. Comput. Mater. Sci. 39: 261–266.

Xiao, L. 1998. Symmetric weak-form integral equation method for three-dimensional fracture analysis. Doctoral dissertation, The University of Texas at Austin.

Xu, G., and Ortiz, M. 1993. A variational boundary integral method for the analysis for 3-D cracks of arbitrary geometry modeled as continuous distributions of dislocation loops. Int. J. Numer. Methods Engrg. 36: 3675-3701.

Xu, X.L., and Rajapakse, R.K.N.D. 2001. On a Plane Crack in Piezoelectric Solids. Int. J. Solids Struct. 38: 7643–7658.

BIOGRAPHY

Weeraporn Phongtinnaboot was born in Krabi, Thailand on July 9, 1978, the son of Pittaya Phongtinnaboot and Malinee Phongtinnaboot. He received his Bachelor of Engineering degree in Civil Engineering from Prince of Songkla University in 2001. Later, He continued his Master's degree in structural civil engineering at Chulalongkorn University in June of 2003 under the supervision of Assistant Professor Dr. Chatpan Chintanapakdee and successfully fulfilled the requirements for the Master of Engineering degree in May of 2006. He was employed as a research assistant in the project of "Study, analysis and development of the design guidelines for shelter and public building in the Tsunami risk proned area" until September of 2006 and continued his Doctoral Degree in Civil Engineering, under the supervision of Assistant Professor Dr. Chatpan Chintanapakdee and Assistant Professor Dr. Jaroon Rungamornrat, in November of 2006 under the Faculty Development Scholarship of the Commission on Higher Education of Thailand with collaboration of AUN/SEED-Net. He spent for eleven months from December of 2009 to October of 2010 to research towards his Ph.D. under the supervision of Associate Professor Dr. Anil C. Wijeyewickrema, Tokyo Institute of Technology, Japan.